PhD degree in Systems Medicine (curriculum in Molecular Oncology)

European School of Molecular Medicine (SEMM),

University of Milan and University of Naples “Federico II”

Settore disciplinare: BIO/10

Biochemical insights into the protein NuMA and its binding partners between mitotic spindle and nuclear compartments

Cristina Renna

European Institute of Oncology (IEO), Milan

Tutor: Dr. Marina Mapelli

European Institute of Oncology (IEO), Milan

PhD Coordinator: Prof. Saverio Minucci

Anno accademico 2020-2021

TABLE OF CONTENTS

GLOSSARY

53BP1	p53-binding protein 1
AB	Apico-basal
ACD	Asymmetric cell division
aPKC	Atypical protein kinase C
Arp1	Actin-related protein 1
ATM	Ataxia-telangiectasia mutated
AU	Arbitrary unit
BD	Binding domain
BICD	Bicaudal D homolog
BICDR1	Bicaudal D-related protein 1
BRCA1	Breast cancer type 1 susceptibility protein
BRCT	BRCA1 C-terminal repeats
BSA	Bovine serum albumin
Cap-Gly	Cytoskeleton-associated protein glycine-rich
CC	Coiled-coil
CDK1	Cyclin-dependent kinase 1
CH	Calponin-homology
Co-IP	Co-immunoprecipitation
CSR	Class switch recombination
C-terminal	Carboxy-terminal
DDR	DNA damage response
DIC	Differential interference contrast
DLG	Discs large
DSB	Double strand break
EB1	End-binding 1
ECL	Enhanced chemiluminescence
ERM	Ezrin–radixin–moesin
FBS	Fetal bovine serum
Fl	Full length
FRAP	Fluorescence recovery after photobleaching
GAR	Gly- and Arg-rich
GAS41	Glioma-amplified-sequence 41
GEF	Guanine exchange factor
GFP	Green fluorescent protein
GSH	Glutathione Sepharose
GST	Glutathione s-transferase
HAP1	Huntingtin-associated protein 1
HC	Heavy chain
HCT116	Human colorectal carcinoma cells
HEK293T	Human embryonic kidney 293T cells
HeLa	Human cervical cancer cells
HR	Homologous recombination
HURP	Hepatoma upregulated protein
IB	Immunoblot
IC	Intermediate chain
IEC	Ion-exchange chromatography
iLID	Light-induced hetero-dimerization system
IR	Ionising radiation

IRIF	Ionizing radiation-induced foci
ITC	Isothermal titration calorimetry
K_d	Dissociation constant
KD	Knockdown
KO	Knockout
LC	Light chain
LGL	Lethal giant larvae
LGN	Leu-Gly-Asn-repeat-enriched protein
LIC	Light intermediate chain
LLPS	Liquid-liquid phase separation
MAR	Matrix attachment region
MBP	Maltose binding protein
MC38	Murine colon adenocarcinoma cells
MDC1	Mediator of DNA damage checkpoint protein 1
MEF	Mouse embryo fibroblast
mInsc	Mammalian homologue of Inscuteable
MRN	MRE11-RAD50-NBS1
MT	Microtubule
Mud	Mushroom body defect
Mw	Molecular weight
NEK	NIMA-related kinase
NHEJ	Non-homologous end-joining
NLS	Nuclear localization signal
N-terminal	Amino-terminal
NuMA	Nuclear mitotic apparatus
OD	Oligomerization domain
O-GlcNAcylation	O-linked β-N-acetylglucosamine glycosylation
Par	Partitioning defective
PARP	Poly (ADP-ribose) polymerase
PDB	Protein data bank
PIP	Phosphoinositides
PLK1	Polo-like kinase 1
PolyU	Poly-uridine
PP2A	Protein phosphatase 2A
PTIP	PAX transactivation activation domain-interacting protein
PtK2	Kidney epithelial cells
PTM	Post-translational modification
RIF1	Replication timing regulatory factor 1
RNF168	RING finger protein 168
RNF8	RING finger protein 8
Robl	Roadblock
RPE-1	Human retinal pigment epithelial-1 cells
SAD	Single-wavelength anomalous diffraction
SAF	Spindle assembly factor
SCD	Symmetric cell division
SD	Standard deviation
SDS-PAGE	Sodium dodecyl sulphate-polyacrylamide gel electrophoresis
SEC	Size-exclusion chromatography
SEM	Standard error mean
Se-Met	Seleno-methionine
shRNA	Short hairpin RNA
SLS	Static light scattering
SPDL1	Spindle apparatus coiled-coil protein 1
TIRF	Total internal reflection fluorescence

TIRR	Tudor-interacting repair regulator
TPR	Tetratricopeptide repeat
TPX2	Targeting protein for Xklp2
TRAK1	Trafficking kinesin-binding protein 1
U2OS	Human osteosarcoma cells
Ub	Ubiquitin
UDR	Ubiquitylation-dependent recruitment
USP28	Ubiquitin carboxyl-terminal hydrolase 28
WT	Wild-type

FIGURES INDEX

ABSTRACT

During my PhD program I worked on two Nuclear Mitotic Apparatus (NuMA)-related projects. The first one centred on the biochemical and structural characterization of the NuMA-dynein mitotic interaction and was published last year on *Structure* with the title *"Organizational principles of the NuMA-dynein interaction interface and implications for mitotic spindle functions"* [1]. The second project focused on the study of the largely unknown role of NuMA in the nucleus during interphase. Regarding this part, I got interesting details on the NuMA-53BP1 (p53-binding protein 1) interaction in the context of liquid-liquid phase separation (LLPS).

In multicellular organisms, the proper organization of the mitotic spindle is essential for accurate cell division, tissue development and homeostasis. In vertebrate cells, the protein NuMA is a master regulator of mitotic spindle functions, implicated in spindle assembly and orientation, working together with the high molecular weight (M_w) dynein-dynactin microtubule (MT)-motor complex. The domain structure of NuMA consists of an N-terminal globular domain, a central extended coiled-coil, and an unstructured C-terminal cargo-binding region. Whether NuMA is a dynein-dynactin activating adaptor is still not known. On these premises, the first part of my PhD project focused on the characterization of the NuMA-dynein binding interface, which I performed in collaboration with other members of the group. The crystal structure of the N-terminal head of NuMA ($NuMA^{1-153}$) revealed that it folds into a hook domain, a conserved feature of the Hook-family dynein-dynactin adaptors interacting directly with the Light Intermediate Chain (LIC) subunit of dynein. Pulldown assays performed with purified proteins indicated a direct interaction between $NuMA^{1-705}$ and LIC and identified four conserved residues in the NuMA hook domain that are crucial for LIC binding. Interestingly, sequence alignment between NuMA and known CC1-box containing dynein-dynactin adaptors revealed the existence of a *CC1-box-like motif* in the NuMA N-terminal coiled-coil domain ($NuMA^{365-376}$) that we demonstrated to be also implicated in contacting LIC. Thus, our studies identified two sites on NuMA' N-terminus required for the interaction with a conserved hydrophobic helix in LIC1 C-terminus. Spindle positioning assays in human cervical cancer (HeLa) cells showed that these newly identified dynein-binding interfaces of NuMA are essential for correct mitotic progression. Collectively, these results support the notion that NuMA acts as a mitotic dynein-dynactin adaptor, forming complexes with similar topology to what observed for other known hook and CC1-box containing adaptors.

In vertebrate cells, NuMA accumulates in the nucleus during interphase and contributes to the DNA damage response (DDR), negatively regulating the 53BP1 double strand break (DSB) repair function. The second part of my PhD project focused on the characterization of the NuMA-53BP1 binding interface. By co-immunoprecipitation (co-IP) experiments in human embryonic kidney 293T (HEK293T) nuclear extracts with α-NuMA antibodies, I confirmed that endogenous NuMA interacts with 53BP1, and that this interaction is decreased upon DNA damage induction [2]. Interestingly, analytical size-exclusion chromatography (SEC) experiments with purified fragments revealed that the C-terminus of 53BP1 (53BP1$^{1484-1972}$) interacts directly with the C-terminus of NuMA (NuMA$^{1821-2115}$). These are two intrinsically disordered domains, common to proteins that undergo LLPS, a mechanism conferring spatial and temporal regulation to biological processes. Since 53BP1 forms DNA damage foci, which are LLPS condensates promoted by its C-terminal disordered region, I tested whether also NuMA is involved in this mechanism. Interestingly, I found that NuMA$^{1821-2115}$ forms liquid droplets *in vitro* at 20 μM and physiological salt concentrations, promoted by electrostatic and polar interactions. By co-IP experiments in HEK293T nuclear extracts, I also detected an interaction of NuMA with the MT nucleator TPX2 (targeting protein for Xklp2). Since TPX2 counteracts the 53BP1 DSB repair function during replication stress and undergoes LLPS, I hypothesized that NuMA could work with TPX2 in regulating the DDR by forming dynamic LLPS condensates. Surprisingly, by co-IP experiments, an interaction between NuMA and 53BP1 was also scored during mitosis, where 53BP1 is known to be part of the centrosome surveillance pathway, another condensate-associated regulatory process.

Further studies are required to uncover the molecular basis and the functional role of the NuMA interaction with 53BP1 both in the DDR and in the centrosome surveillance pathway.

1. INTRODUCTION

During my PhD I focused on the biochemical and structural study of the protein NuMA and its binding partners: the MT-motor cytoplasmic dynein during mitosis and the DDR protein 53BP1 during interphase. In this perspective, the introduction below will give an overview of the processes in which NuMA-dynein and NuMA-53BP1 complexes are involved in vertebrate cells.

1.1 Cell division and the mitotic spindle

The ordered and highly coordinated series of events that leads to cell duplication and division is called the cell cycle. The eukaryotic cell cycle is divided into four sequential phases: G_1, S, G_2, and M. G_1, S, and G_2 together are called interphase: chromosome duplication happens in S phase (S stands for DNA synthesis), and cell growth during the gap phases G_1 and G_2. Chromosome segregation and cell division occur during M phase, which comprises two major processes: nuclear division (mitosis) during which the duplicated chromosomes are distributed into the daughter nuclei, and cytoplasmic division (cytokinesis), when the cell itself divides in two. Mitosis is further divided into five phases: prophase, prometaphase, metaphase, anaphase, and telophase [3] (figure 1.1).

At prophase, the replicated chromosomes, each consisting of two closely associated sister chromatids, condense. Outside the nucleus, the mitotic spindle starts assembling between the two centrosomes, which have duplicated and moved apart. Prometaphase initiates with the breakdown of the nuclear envelope. Chromosomes attach to spindle MTs via their kinetochores and undergo active movement. At metaphase, the chromosomes are aligned at the equator of the spindle, midway between the spindle poles, and the kinetochore MTs attach sister chromatids to opposite poles of the spindle. At anaphase, the sister chromatids separate to form two daughter chromosomes, and each is pulled toward the spindle pole it faces. During telophase, the two sets of daughter chromosomes decondense. A new nuclear envelope reassembles around each set, forming two nuclei. The division of the cytoplasm starts with the contraction of the contractile ring and completes during cytokinesis with the generation of two daughter cells [3] (figure 1.1).

The mitotic spindle is responsible for faithful chromosome segregation during cell division, and errors in spindle formation can lead to aneuploidy, an unbalanced chromosome complement, or cytokinesis failure, which are associated with tumorigenesis [4].

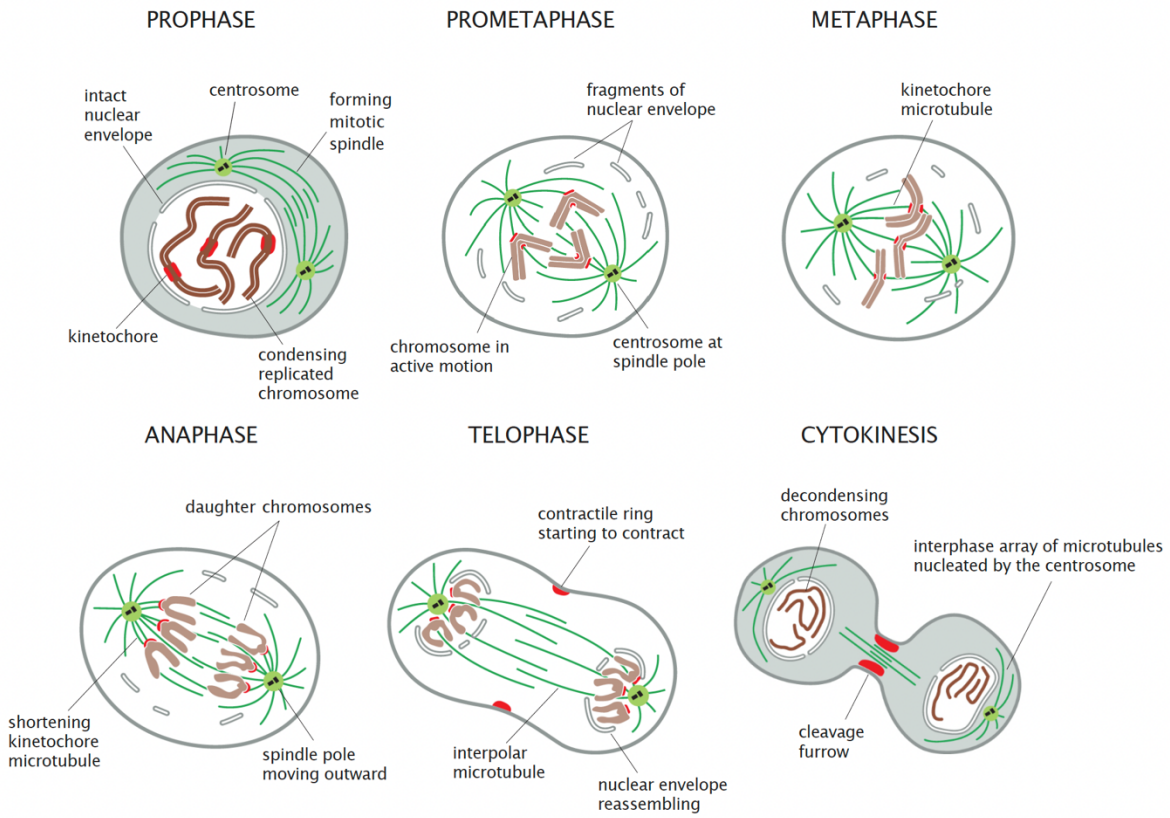

Figure 1.1 - The principal events of M phase in a eukaryotic cell

The five stages of mitosis and cytokinesis, collectively called M phase, typically occupy only a small fraction of the cell cycle. Adapted from Alberts et al., Molecular Biology of the Cell, 2015 [3].

In the next subparagraphs (1.1.1 and 1.1.2) I will introduce the processes of spindle assembly and orientation in which the protein NuMA was found to play essential functions during mitosis.

1.1.1 Principles of mitotic spindle assembly

The mitotic spindle is a large intracellular structure organized by MTs, polar α/β-tubulin filaments that emanate from the centrosomes, which not only nucleate but also organize MTs of the spindle [5]. The core of the mitotic spindle is a giant bipolar array of MTs, the minus-ends of which are focused at the two spindle poles, while the plus-ends radiate outward from the poles. Three classes of MTs make up the spindle: astral MTs, kinetochore MTs, and interpolar MTs. Astral MTs emanate from the centrosomes and reach the cell cortex, having a major role in spindle positioning; bundles of kinetochore MTs connect spindle poles to the kinetochores and are essential for equal segregation of sister chromatids; the plus-ends of interpolar MTs overlap with the plus-ends of MTs from the other pole, resulting in an antiparallel array in the spindle midzone [6] (figure 1.2a).

Multiple mechanisms cooperate to ensure the bipolarity of the spindle: the MT-mediated pathway, the centrosomal spindle assembly pathway, in which mitotic kinases like NIMA-related kinases (NEKs), cyclin-dependent kinases (CDKs), Polo-like kinases (PLKs) and Aurora kinases play an important role [7], and the chromosomal pathway, which consists in the establishment of a Ran-GTP gradient around mitotic chromosomes. In this case, the guanine exchange factor (GEF) RCC1 that is bound to chromatin stimulates the small GTPase Ran in the cytosol to bind GTP in place of GDP. The activated small G protein Ran-GTP, which is also involved in nuclear import and export, promotes spindle self-organization through the release of importin-bound spindle assembly factors (SAFs) such as the non-motile MT-associated proteins NuMA, TPX2, and HURP (hepatoma upregulated protein), and the motor protein kinesin-14, which stimulate MT nucleation and organization and regulate MT dynamics [8]. Recently Tsuchiya and colleagues found that in human colorectal carcinoma (HCT116) cells the Ran-GTP, required to activate HURP and kinesin-14 near chromosomes, is not essential to activate NuMA away from chromosomes for spindle-pole focusing and to target TPX2 to the spindle poles [9].

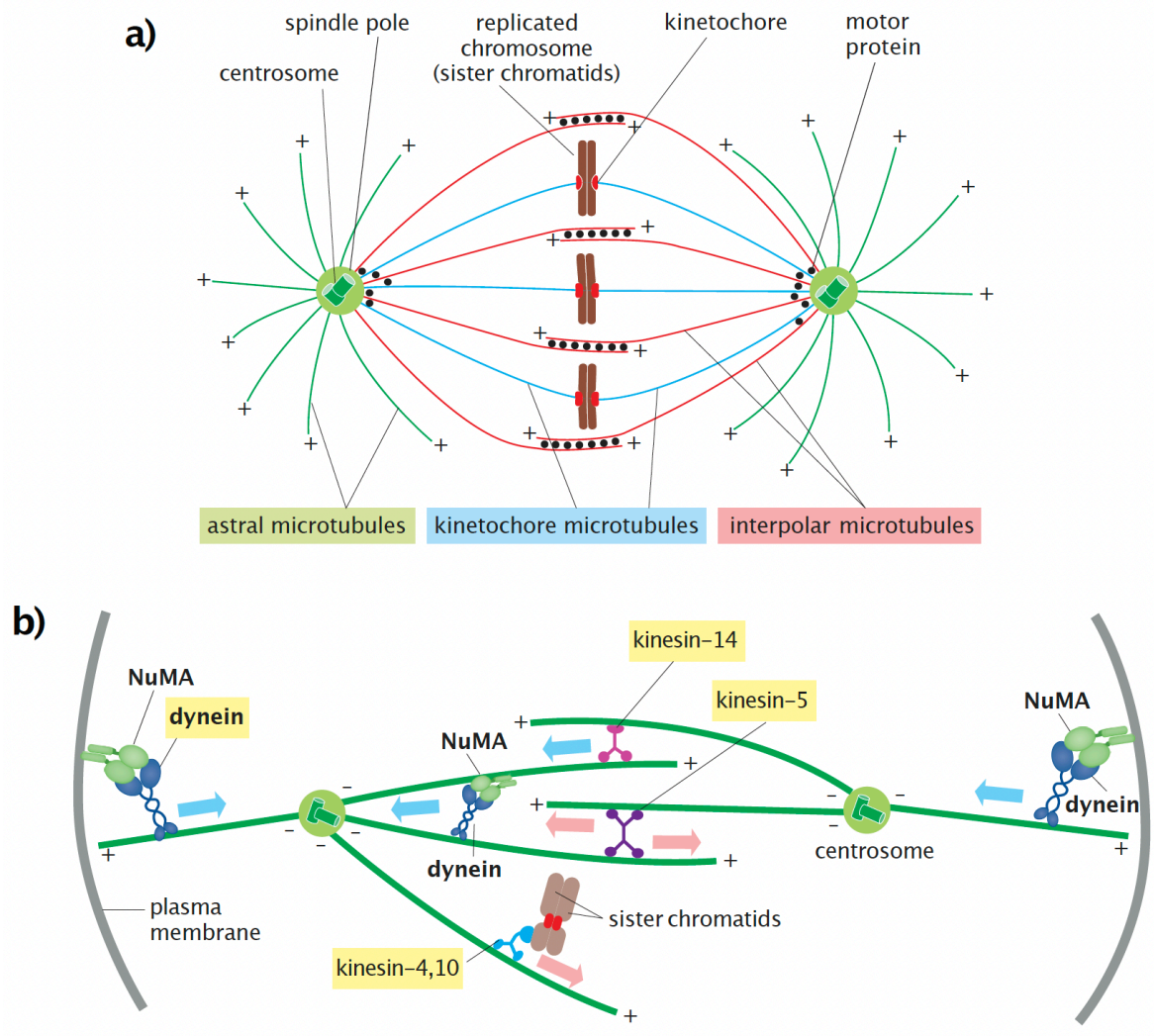

Figure 1.2 - The metaphase mitotic spindle in a eukaryotic cell

a) *The three classes of spindle MTs. Astral MTs (light green) radiate outward from the poles; kinetochore MTs (light blue) connect the spindle poles with the kinetochores of sister chromatids; interpolar MTs (light red) from the two poles interdigitate at the spindle equator.* ***b)*** *Four major classes of MT-dependent motor proteins contribute to spindle assembly and function. The coloured arrows indicate the direction of motor protein movement along a MT (cyan toward the minus-end and pink toward the plus-end). Adapted from Alberts et al., Molecular Biology of the Cell, 2015* [3].

Spindle assembly is governed by unidirectional and opposite-polarity MT-based motor proteins, the kinesin-related proteins, which usually move toward the plus-end of MTs, and dynein, which moves toward the minus-end (retrograde movement). Kinesin-5 (human Eg5) contains two motor domains that interact with the plus-ends of antiparallel MTs in the spindle midzone. Because the two motor domains move toward the plus-ends of the MTs, they slide the two antiparallel MTs past each other toward the spindle poles, pushing the poles apart [10] (figure 1.2b). When Eg5 is inhibited, spindles form as monopoles with minus-ends clustered into a single aster [11]. Kinesin-14 (KIFC1 or human HSET) is a minus-end directed motor with a single motor domain and another domain that can interact with a neighboring MT. It cross-links antiparallel interpolar MTs at the spindle midzone and pulls the poles together, stimulating bipolar spindle assembly and focusing spindle poles [12]. The chromokinesins kinesin-4 and kinesin-10 are plus-end directed motors that associate with chromosome arms and push the attached chromosome away from the pole [13] (figure 1.2b). Finally, dynein is a minus-end directed motor that links the plus-ends of astral MTs to components of the actin cytoskeleton at the cell cortex and determines the division orientation in complex with the $G\alpha_i$-LGN-NuMA module (described in paragraph 1.1.2.1). It also focuses MT-minus-ends at the spindle poles, contributing to spindle-pole focusing in cooperation with the protein NuMA [14–16] (figure 1.2b).

Defects at the spindle poles resulting in abnormal centrosome separation in prophase [17] and impaired astral MTs nucleation from the centrosomes [18] often cause spindle assembly defects and misoriented divisions.

1.1.2 Principles of mitotic spindle orientation

In addition to spindle assembly, NuMA and dynein, together with the $G\alpha_i$-LGN module, constitute the core mechanism of mitotic spindle positioning in vertebrate cells [19] (paragraph 1.1.2.1).

In this paragraph I will give emphasis to the impact of spindle orientation on epithelial tissues. In multicellular organisms, cell divisions occur with a defined orientation of the

mitotic spindle compared to the tissue architecture. Oriented divisions shape epithelial architecture contributing to tissue formation during morphogenesis and homeostasis in adult life, as they determine the position of daughter cells within the tissue and also, in the case of vertebrate stem cells, their fate [20].

Stem cells of stratified epithelia, sitting on the underlying basement membrane and in physical contact with one another, form multiple layers dividing through oriented divisions, in which the mitotic spindle aligns along a specific axis determined by intrinsic cellular polarity. Epithelial polarity is settled by antagonizing forces between the evolutionary conserved apical Par3/Par6/aPKC and baso-lateral Scribble/DLG/LGL polarity complexes [21]. The orientation of the spindle with respect to the apico-basal (AB) polarity axis determines the symmetric or asymmetric outcome of stem cell division [22] (figure 1.3). Specifically, in symmetric cell divisions (SCDs), divisions occurring within the plane of epithelia, or planar divisions, the spindle is positioned perpendicularly to the AB axis, and generates two equal-sized daughters that inherit identical cellular content and retain the same integrin-mediated contacts with the basement membrane. This type of cell division shapes the architecture of epithelial sheets, leading to tissue growth and expansion of the basal progenitor pool (figure 1.3a), and controlling tissue directional growth and elongation (figure 1.3b) [20]. Conversely, in asymmetric cell divisions (ACDs) the spindle is aligned parallel to the AB axis, ensuring unequal partitioning of cellular components, and differential cell fate specification. This type of cell division promotes tissue differentiation and epithelial stratification during epidermal murine skin development, resulting in one basal cell that remains progenitor and one apical daughter cell that undergoes differentiation [23] (figure 1.3c).

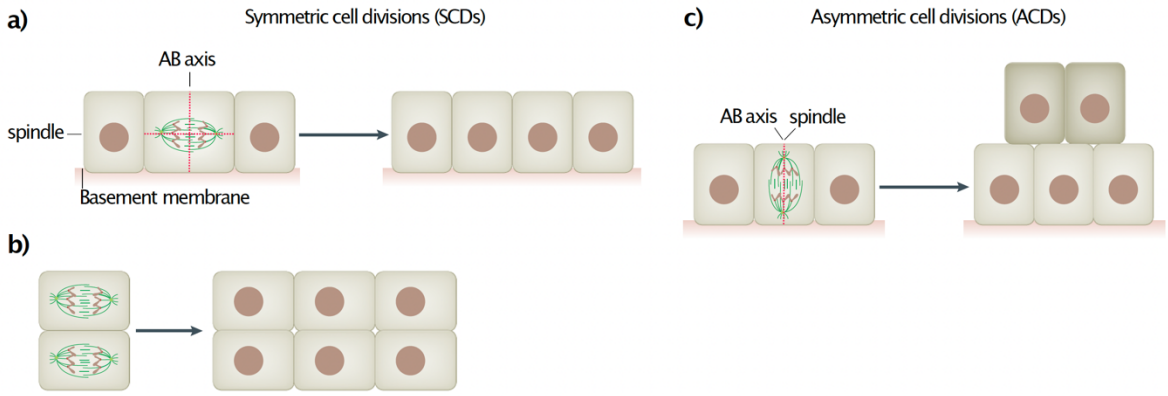

Figure 1.3 – Roles of spindle orientation in epithelial organization

a) *A simple epithelium is maintained by orientation of the mitotic spindle parallel to the basement membrane.* ***b)*** *Planar divisions occurring in one direction across the epithelium lead to tissue elongation during morphogenetic growth or homeostatic turnover.* ***c)*** *Development of stratified*

epithelia is driven by an orientation of the mitotic spindle perpendicular to the basement membrane, which generates additional layers of cells. These divisions are typically coupled to cell fate determination, by which the basal daughter cell remains a progenitor and the apical daughter cell is committed to differentiation. Adapted from Lechler and Mapelli, Nat. Rev. Mol. Cell Biol., 2021 [20].

Mispositioning of cells within the tissue would lead to an imbalance between the pools of progenitor and differentiating cells, resulting in excessive differentiation and depletion of progenitor cells, or allowing the production of additional stem cells, potentially causing abnormal proliferation and tumour formation. Work in *Drosophila* demonstrated the induction of tumour growth by altered stem-cell asymmetric division [24]. The mechanistic understanding of how spindle misorientation drives cancer in vertebrate models remains fragmentary and necessitates further studies [25].

To safeguard proper tissue organization and development and to limit malignant growth, defective spindle orientation can be ameliorated in tissues under physiological conditions by correction mechanisms. Specifically, in order to maintain epithelial integrity, in the developing murine epidermis the deleterious effects of aberrant spindle alignment are typically corrected in telophase (process known as "telophase rescue") [26]. In the *Drosophila* imaginal discs, cells that are mispositioned in the tissue after division, especially those displaced from the basement membrane, may undergo apoptosis due to loss of contact or loss of other microenvironmental survival signals [27]. Finally, another mechanism to protect *Drosophila* epithelial monolayers against the consequences of misoriented divisions is the reintegration of misplaced cells by lateral adhesion [28,29].

In conclusion, rescue mechanisms operate in the tissue to avoid the tumorigenic potential of spindle misorientation. However, loss of spindle orientation, owing for example to mutations in the spindle positioning machinery (described in the next subparagraph), might promote tumour formation.

1.1.2.1 Working principles of the force-generating $G\alpha_i$-LGN-NuMA-dynein-dynactin module

Early studies in invertebrates and epithelial cells in culture led to the identification of evolutionarily conserved core mechanisms of mitotic spindle positioning that are centred on the $G\alpha_i$-LGN-NuMA-dynein-dynactin module [19].

In HeLa cells at metaphase, GDP-loaded $G\alpha_i$ subunits of membrane-associated heterotrimeric G-proteins ($G\alpha_i$-GDP) localize in cortical crescents above the spindle poles, accumulating at caveolae, caveolin-rich membrane patches (figure 1.4) [30]. Four $G\alpha_i$-GDP

subunits, whose myristoyl group inserts into the phospholipid bilayer, sequentially recruit the Leu-Gly-Asn-repeat-enriched protein LGN (also known as GPSM2 in vertebrates and named Pins in *Drosophila* and GPR-1 and GPR-2 in *C. elegans*) and the protein NuMA (named Mud in *Drosophila* and LIN-5 in *C. elegans*) [31]. NuMA then targets the dynein-dynactin MT-motor complex, which in turn, being stably connected to the cell cortex, uses its retrograde movement towards MT minus-ends to generate pulling forces on astral MTs that orient the mitotic spindle [32] (figure 1.4).

In human osteosarcoma (U2OS) and retinal pigment epithelial-1 (RPE-1) cells in culture, the activation of traction forces acting on the mitotic spindle starts in late prometaphase [33], when the MT cytoskeleton is reorganized in a bipolar spindle, then stabilized in an orientation that is maintained through anaphase and telophase.

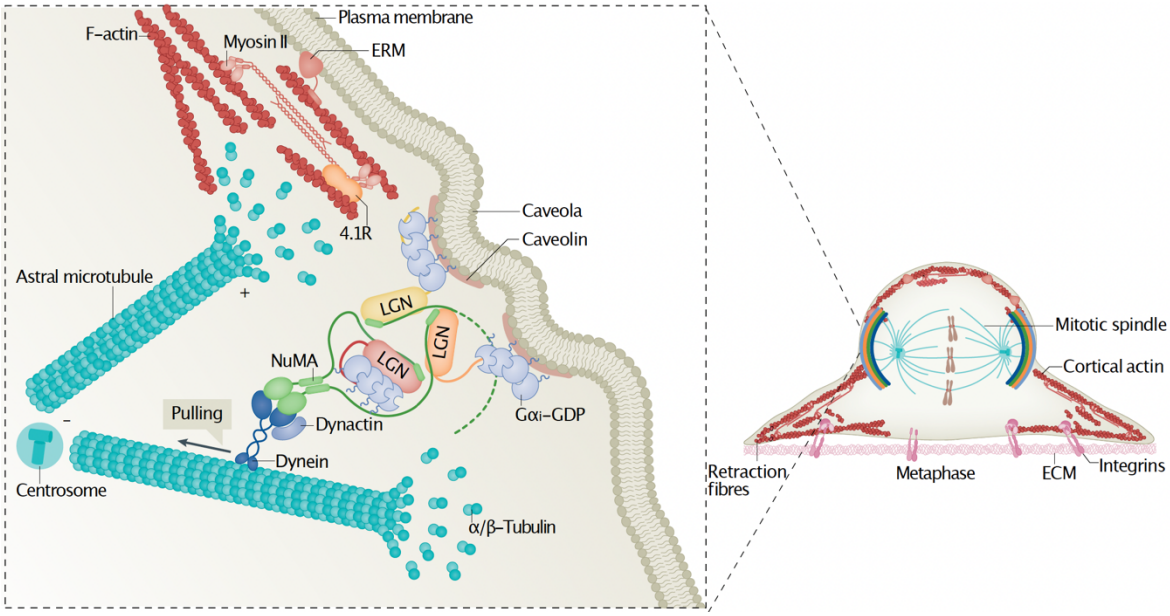

Figure 1.4 – Molecular events promoting cortical recruitment of force generators in metaphase

Cartoon representation of the molecular players implicated in spindle positioning at the mitotic cell cortex. The metaphase crescents of the cortically restricted force generating machines exerting traction forces on astral MTs are organized on the dynein-dynactin-NuMA complexes, targeted to the membrane by Gα$_i$-LGN via NuMA. Adapted from Lechler and Mapelli, Nat. Rev. Mol. Cell Biol., 2021 [20].

The force-generating Gα$_i$-LGN-NuMA-dynein macromolecular complex modulates the extent of MT-pulling forces in correlation with cortical LGN levels. Accordingly, ectopic overexpression of LGN but not of NuMA results in an increased rotation of the spindle ("spindle rocking") that is caused by excessive cortical forces [32].

In a more structural detail, vertebrate LGN is a 77-kDa protein consisting of eight amino-terminal (N-terminal) tetratricopeptide repeats (TPRs) and a carboxy-terminal (C-terminal) region coding for four GoLoco motifs interacting with four $G\alpha_i$-GDP subunits (figure 1.5a). LGN behaves as a conformational switch that in interphase is kept in an inactive closed conformation by a head-to-tail intramolecular interaction between the inner surface of the LGN TPR domain and the GoLoco motifs [31,34] (figure 1.5b). Cooperative binding of cortical $G\alpha_i$-GDP to the LGN GoLoco region induces a conformational opening of LGN that allows binding of the C-terminal region of NuMA (minimal LGN-BD$^{1900-1926}$, figure 1.6c) in the same TPR cleft previously occupied by the LGN GoLoco [35].

Recent biochemical and structural studies from our lab uncovered the heterohexameric architecture of the NuMA-LGN complexes in which three TPR domains of LGN interact with the C-terminal LGN-binding stretch of NuMA (longer LGN-BD$^{1861-1928}$, figure 1.6c) in a donut-shaped architecture (figure 1.5c). Of note, the heterohexameric rings are determined by a NuMA motif spanning residues 1861-1899 preceding the high-affinity LGN-binding peptide [36]. NuMA and LGN assemble in oligomers that can promote multivalent interactions key to sustain robust spindle pulling on astral MTs, as demonstrated in HeLa cells in adhesion and in Caco-2-polarized three-dimensional cysts [36].

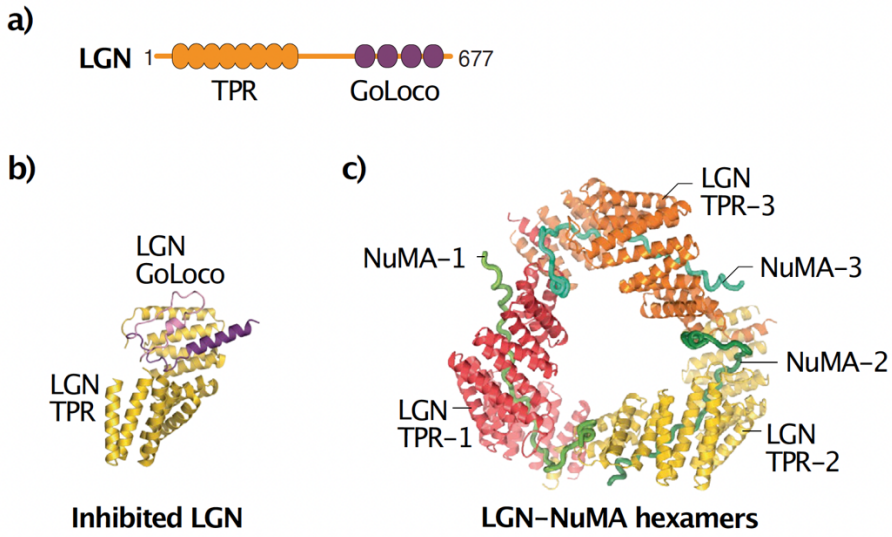

Figure 1.5 - Structural details of the LGN-NuMA binding

a) *Cartoon representation of human LGN domain structure.* ***b)*** *In the crystal structure of the LGN inhibited closed conformation, the TPR domain in yellow, folded as a helical cradle, is occupied by the GoLoco helices in purple (PDB ID: 4JHR).* ***c)*** *In the crystal structure of LGN-NuMA hexamers, LGN bound to $G\alpha_i$-GDP forms doughnut-shaped heterohexamers with the C-terminal portion of the protein NuMA (PDB ID: 6HC2).*

The $G\alpha_i$-LGN-NuMA-dynein-dynactin complex works as a pulling machinery at the cell cortex, which is a layer of actomyosin, F-actin and associated proteins forming on the inner side of the membrane and responsible for mitotic cell rounding (figure 1.4). The nearly spherical shape of the mitotic cell is essential for the assembly and the orientation of the mitotic spindle. The stiffness of the mitotic actomyosin cortex, which is needed to provide a rigid scaffold counterbalancing MT-pulling forces exerted by the dynein motor to position the spindle, is regulated by F-actin- and NuMA- binding 4.1R proteins and by ERM (ezrin–radixin–moesin) proteins connecting the plasma membrane to the actomyosin cortex (figure 1.4). These proteins are linked to spindle orientation by favouring LGN and NuMA enrichment into cortical crescents [37,38]. Recent structural and functional studies from our lab have also shown that in cultured HeLa cells the actin-binding protein Afadin (Canoe in *Drosophila*) localizes at the cell cortex and promotes the recruitment of LGN by direct interaction with its TPR domain [39].

The recruitment of force generators to specific sites is also guided by extracellular cues such as cell-cell contacts including adherens junctions. Even the cytoplasmic tail of the cell-cell adhesion protein E-cadherin is able to interact directly with the TPR domain of LGN [40]. E-cadherin and Afadin bind to LGN competitively with NuMA, as they all share a common negatively charged motif that binds to the TPR domain of LGN [35].

In addition, in murine mammary stem cells, NuMA competes with mInsc (mammalian homologue of Inscuteable) for LGN TPR binding, with mInsc showing higher affinity [41] and forming with LGN so stable tetramers that cannot be dissociated by NuMA [42].

1.2 NuMA-1 (Nuclear Mitotic Apparatus)

The NuMA-1 protein (here referred to as NuMA) was identified in 1980 and named after its localization pattern to both the interphase nucleus and mitotic spindle poles [43]. It is well conserved in vertebrates and dynamically changes its subcellular localization from the interphase nucleus to the mitotic spindle poles and the mitotic cell cortex.

Endogenous NuMA is highly abundant, at an estimated 10^6 molecules per cell [44], and is expressed at similar levels in different mouse tissues [15].

NuMA is essential for early embryonic development and viability in mice. Indeed, deletion of exon 22 of the mouse NuMA gene, which corresponds to exon 24 of human NuMA (figure 1.6c), is embryonic lethal when homozygous [15,45].

In mice, NuMA is required for epidermal morphogenesis, balancing proliferation and differentiation, and the symmetric or asymmetric outcome of division of stem and progenitor cells. As better described in the previous paragraph, NuMA is one of the core constituents

of the effector machinery that governs spindle positioning. In this context in the developing mouse skin, where progenitor cells switch to predominantly asymmetric divisions, concomitant with stratification at embryonic day 16.5, NuMA knockdown (KD) causes a shift to planar divisions [23,46]. In murine epidermal progenitors with deletion of NuMA' MT-binding domain 1 (MT-BD1, figure 1.6c), basal cells expand into suprabasal layers and mix with differentiated cells. Differentiation defects such as downregulation of later differentiation markers and upregulation of stress markers are evidenced [45].

During mitosis NuMA has an important role in spindle pole integrity: conditional deletion of NuMA in mouse embryo fibroblasts (MEFs) leads to spindle defects like apolar centrosomes and pole-defocusing phenotypes [15]. NuMA has critical roles in the generation of spindle bipolarity in acentrosomal human cells and in centrosome clustering [47]. In cancer cells with multiple centrosomes, NuMA overexpression results in a substantial increase in multipolar spindles, centrosome clustering defects as well as in multinucleated cells [48]. NuMA is highly expressed in epithelial ovarian cancer tumours and high NuMA levels correlate with micronuclei formation, aneuploidy and genomic instability [49].

1.2.1 Domain architecture of human NuMA

Human NuMA is a 238 kDa, 2115-residue-long protein. Its domain structure consists of an N-terminal globular domain predicted to fold as a calponin-homology (CH) domain [50], a central 1500-residue coiled-coil mediating dimerization that is organized into 7 coiled-coil segments separated by short nonhelical linkers [51], and an unstructured C-terminal region that contains several important domains including a nuclear localization signal (NLS) [52] (figure 1.6a).

In detail, the N-terminal region of NuMA encompassing residues 1-705 is the dynein-dynactin-BD identified by Kotak and colleagues by co-IP experiments with mitotic HeLa extracts and GFP-NuMA transfected constructs [32]. The shorter fragment NuMA$^{1-505}$ was recently found to be sufficient for cortical dynein recruitment [53]. Sequence alignment between different orthologues of NuMA identified a *spindly-like motif* in the N-terminal coiled-coil region that is well conserved in vertebrates and is homologous to the spindly motif present in dynein-dynactin cargo adaptors and interacting directly with the dynactin pointed-end complex (this will be better explained in paragraph 1.3.1.1) [53] (figure 1.6b).

The central long coiled-coil region of NuMA (residues 216-1694, figure 1.6a) undergoes homodimerization, as demonstrated by Harborth and colleagues for residues 199-432 and 670-1700 [54], by Forth and colleagues for residues 1-400 [55], and by our lab for residues 1592-1694 [36]. It is required for spindle pulling force generation [53], inhibits chromatin binding during anaphase, and promotes nuclear formation [56].

The C-terminal region of NuMA has been extensively studied, contains several important binding regions, and is highly regulated by phosphorylation events, which will be better described in paragraph 1.3 (figure 1.6c).

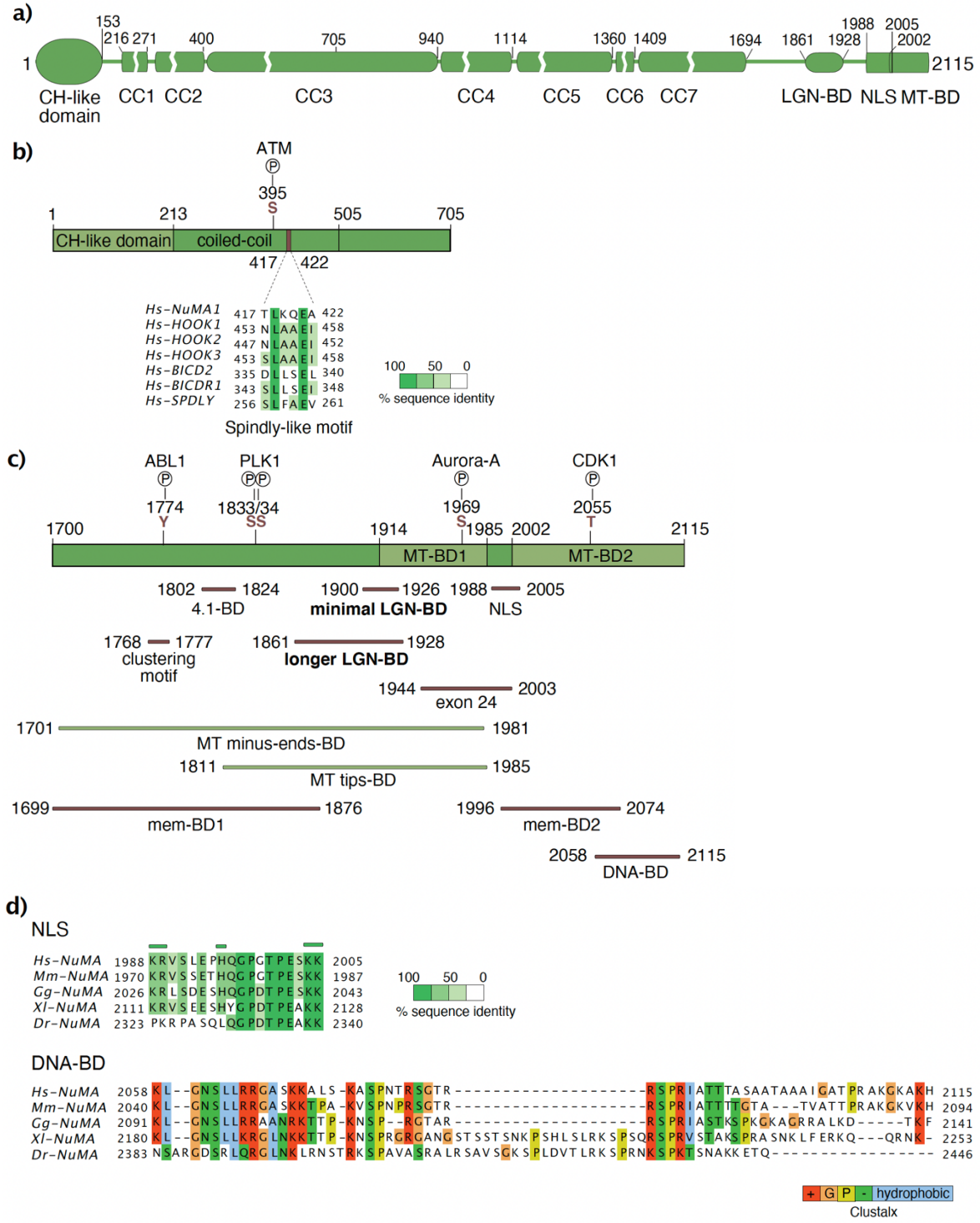

Figure 1.6 – Domain structure and interaction partners of NuMA

a) *Full-length human NuMA isoform 1.* ***b)*** *Close-up view of the NuMA N-terminal dynein-dynactin binding region. For the spindly-like motif the Homo sapiens sequences of NuMA (Uniprot entry Q14980), Hook1 (Uniprot entry Q9UJC3), Hook2 (Uniprot entry Q96ED9), Hook3 (Uniprot entry Q86VS8), BICD2 (Uniprot entry Q8TD16), BICDR1 (Uniprot entry Q6ZP65) and SPDL1 (Uniprot*

entry Q96EA4) were aligned with CLUSTALΩ and coloured in Jalview by percentage of identity. ***c)*** *Close-up view of the NuMA C-terminal region interacting with multiple factors.* ***d)*** *NuMA sequences from Homo sapiens, Mus musculus (Uniprot entry E9Q7G0), Gallus gallus (Uniprot entry D8MIU8), Xenopus laevis (Uniprot entry P70012) and Danio rerio (NCBI entry XP_009290241.1) were aligned with CLUSTALΩ and coloured in Jalview by percentage of identity for the NLS sequence and by Clustalx for the DNA-BD.*

As anticipated in paragraph 1.1.2.1, the NuMA$^{1900-1926}$ peptide is the minimal region required for binding to the inner groove of LGN TPR [35]. Our lab found that a longer NuMA$^{1861-1928}$ forms hetero-hexameric oligomers with LGN$^{7-367}$ in a donut-shaped architecture, that are essential for spindle orientation processes and epithelial morphogenesis [36] (figure 1.5c).
Recently Okumura and colleagues, using an optogenetic reconstitution system in HeLa cells, discovered a clustering domain in a conserved and hydrophobic region of NuMA C-terminus (residues 1768-1777) that promotes the formation of NuMA' punctate signals at the cell cortex, and is required for spindle pulling and positioning at metaphase [53]. Further studies are needed to explore whether this NuMA clustering activity functions synergistically with the NuMA-LGN oligomers to organize high-ordered structures at the cell cortex [36].
One of the most studied NuMA function is its ability to interact with MTs. NuMA contains two discontinuous MT-BDs that are important for its mitotic spindle functions (figure 1.6c). MT-BD1 (residues 1914-1985) was identified in 2002 by Du and colleagues by co-sedimentation experiments with taxol-stabilized MTs [57] and, as shown in figure 1.6c, partially overlaps with the LGN-BD. Recently our lab identified, by MT co-sedimentation and MT-bundling assays, a second MT-BD (MT-BD2, residues 2002-2115), which is compatible with LGN binding [58] (figure 1.6c). NuMA MT-BD1 is required for spindle-pole focusing in MEFs [15] and human HCT116 cells [9], and is critical for spindle orientation in mouse keratinocytes [45]. NuMA residues 1701-1981 are able to recognize MT minus-ends in mitotic kidney epithelial (PtK2) cells [59] and intriguingly the NuMA$^{1811-1985}$ fragment can accumulate at the curling MT ends and remain associated with the depolymerizing MT plus-ends in mouse keratinocytes [45] (figure 1.6c). In human cells MT-BD2 is required for spindle pulling activity [53], while it is dispensable for spindle-pole focusing [9]. It can recognize both the MT lattice and α/β-tubulin dimers, suggesting that NuMA could set the dynamic rate at the plus ends and increase dynein processivity on the MT lattice [36].
Two membrane binding regions (mem-BD1-2) [60,61] and a 4.1 protein binding region [62] allow the direct targeting of NuMA to the anaphase cell cortex independently of LGN (figure 1.6c). The C-terminal domain of NuMA is also important for NuMA targeting to the nucleus [52] and for its direct interaction with DNA [63] (figure 1.6c). Sequence alignment between

different orthologues of NuMA in the NLS sequence shows the three conserved motifs required for Importin-α binding and the same alignment in the DNA-BD highlights in red the conserved positively charged arginine and lysine residues involved in DNA binding (figure 1.6d). It is interesting to note that this DNA-BD partially overlaps with the MT-BD2 (figure 1.6c).

1.3 Mitotic regulation of NuMA at the spindle poles and the cell cortex

NuMA is highly regulated throughout the cell cycle. At mitotic onset, CDK1-mediated phosphorylation in late-prophase releases NuMA from chromatin. However, the single CDK1 site that uncouples NuMA from chromatin is not yet known [63]. Upon nuclear envelope break-down in prometaphase NuMA is released into the cytoplasm where it interacts with the dynein-dynactin MT-motor complex through its N-terminal region [32]. In mitosis, NuMA together with dynein-dynactin, plays major roles in all spindle functions, including spindle assembly, orientation, and elongation. Consistent with these activities, in unpolarized HeLa cells during metaphase, NuMA and dynein are distributed at the spindle poles and at the cortical regions facing the spindle poles, and in anaphase are enriched at the cortical crescents above the poles (figure 1.7).

To coordinate spindle organization with mitotic progression, the distribution of NuMA, and hence of dynein-dynactin, between the poles and the cortex is finely tuned by mitotic kinases. NuMA is phosphorylated by CDK1, which is counteracted by PP2CA-B55γ-PPP2R1B phosphatase activity, and these phosphorylation-dephosphorylation events are balanced to regulate NuMA binding to the plasma membrane phospholipids [64,65]. During metaphase, CDK1-mediated phosphorylation of NuMA at the evolutionary conserved Thr2055 residue (figure 1.6c) negatively regulates its direct membrane targeting, ensuring low cortical levels of NuMA and dynein for accurate spindle positioning. Thus, only NuMA not phosphorylated at Thr2055 localizes at the cell cortex (figure 1.7a). At anaphase onset, when CDK1 activity decreases, NuMA is dephosphorylated by PP2CA-B55γ-PPP2R1B, which allows the enrichment of NuMA, and thus of dynein, at the cortical crescents above the poles, generating stronger traction forces that assist spindle elongation and sister chromatin separation (figure 1.7b). This anaphase-specific cortical recruitment of NuMA and dynein is independent of LGN and $G\alpha_i$ but involves cortical 4.1R and 4.1G proteins and phosphoinositides (PIP/PIP2), which interact with the C-terminal region of NuMA (figure 1.6c) [60,61,66].

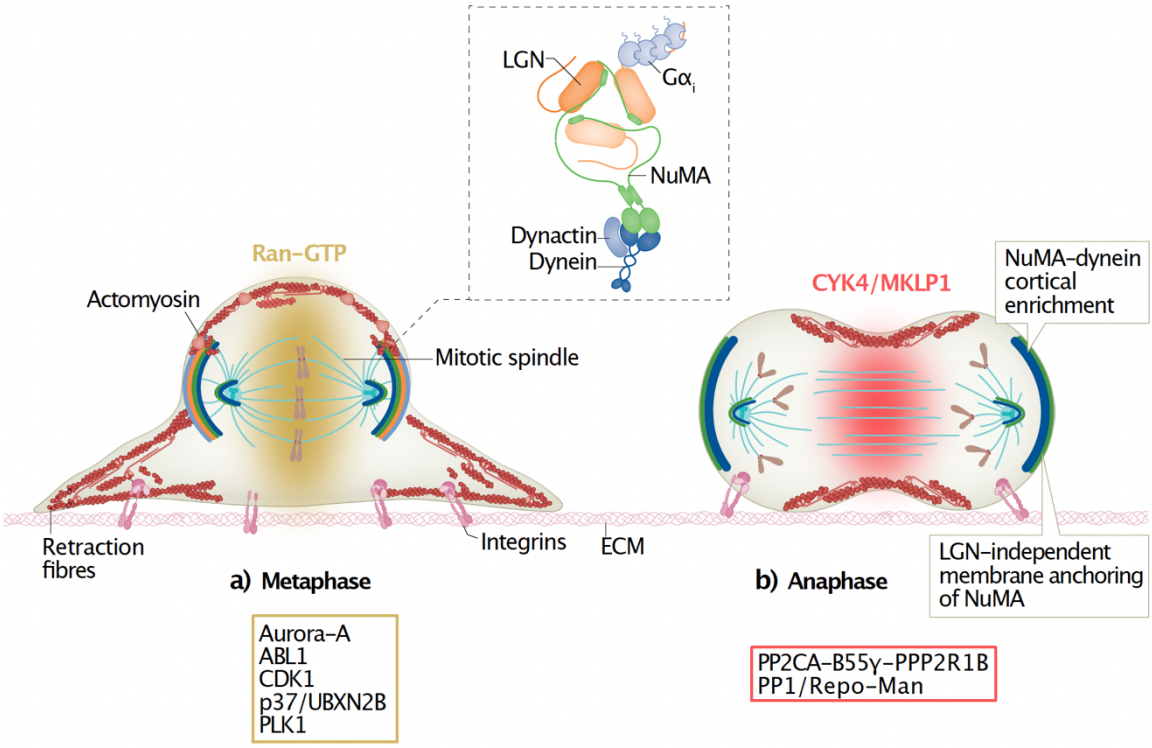

Figure 1.7 - NuMA is a master regulator of the mitotic spindle

a) *Scheme of the regulation of NuMA localization in metaphase HeLa cells for spindle positioning and centering. NuMA is phosphorylated by Aurora-A, ABL1, CDK1, whose activities are highest at the spindle poles and lowest at the cell cortex, and by PLK1, which is enriched at the spindle poles.* ***b)*** *Scheme of the regulation of NuMA localization in anaphase HeLa cells for robust spindle elongation. NuMA is dephosphorylated by PP2CA-B55γ-PPP2R1B. Adapted from Lechler and Mapelli, Nat. Rev. Mol. Cell Biol., 2021* [20].

Phosphorylation of NuMA Ser1969 by Aurora-A (figure 1.6c), a mitotic kinase activated by the MT-associated protein TPX2 at the spindle poles, positively regulates the cycling rates of NuMA at the poles, enabling its cortical recruitment at metaphase [58]. Cortical NuMA localization is maintained by another kinase, ABL1, which phosphorylates the well-conserved Tyr1774 residue of NuMA, located in the clustering motif (figure 1.6c), to regulate spindle orientation [67].

Interestingly, p37/UBXN2B, a cofactor of the p97 AAA ATPase, regulates spindle orientation in mammalian cells by limiting the levels of cortical NuMA via the phosphatase PP1 and its regulatory subunit Repo-Man. In anaphase PP1/Repo-Man promotes the accumulation of NuMA at the cortex, while in metaphase, p37 negatively regulates this function of PP1, resulting in lower cortical NuMA levels and correct spindle orientation (figure 1.7) [68].

PLK1 phosphorylates NuMA at Ser1833/34 residues (figure 1.6c), and this spindle-pole derived activity dissociates the NuMA-dynein complex from the membrane when the poles

get too close to the cortex, in this way generating asymmetric pulling forces critical to sustain spindle centering by oscillatory movements and to correct spindle mispositioning. The proximity of a spindle pole to the cortex excludes dynein from this cortical site. Concomitantly, dynein accumulates to the side of the cell facing the opposing and more distant spindle pole and generates pulling forces, which in turn reposition the spindle [69,70].

In addition to these kinases, the chromosome-derived Ran-GTP gradient, at metaphase, displaces cortical NuMA-LGN from regions close to chromatin in a distance dependent manner. The Ran-GTP gradient negatively regulates the interaction between $G\alpha_i$ and NuMA-LGN in the vicinity of the metaphase chromosomes in the spindle midzone. This helps to restrict cortical dynein to the polar cell cortex, downstream of NuMA-LGN (figure 1.7a) [69]. However, a recent finding from Kiyomitsu lab suggests that the Ran pathway is not essential to activate NuMA away from chromosomes [9]. Further studies are required to precisely understand the mechanism and significance of Ran-based regulation of NuMA. NuMA continuous exclusion from the equatorial region of the cell cortex during anaphase is dependent on the centralspindlin components of the cytokinetic machinery CYK4 and MKLP1 (figure 1.7b) [60].

In addition to being phosphorylated, NuMA is also subjected to other post-translational modifications (PTMs) that are important for its proper localization at the mitotic spindle poles. Specifically, NuMA is SUMOylated at Lys1766 [71] and subjected to O-linked β-N-acetylglucosamine glycosylation (O-GlcNAcylation) at Ser1844 [72].

NuMA can be considered as a dynein adaptor protein since it is required for the recruitment of the dynein-dynactin complex to the spindle poles [59] and the cell cortex. NuMA targets dynactin to MT minus-ends, localizing there the dynein activity of clustering spindle MTs into poles [59]. In order to study the NuMA function at the mitotic cell cortex, Okumura and colleagues used a light-induced hetero-dimerization system (iLID) to target different NuMA constructs to the membrane during mitosis, independently of the LGN-$G\alpha_i$ complex [53]. In HeLa cells, the $NuMA^{1-505}$ fragment was found to be sufficient to recruit dynein to the cell cortex, and both its N-terminal globular domain and short coiled-coil region were found to be required for cortical dynein recruitment. This fragment is not enough to pull on the spindle, instead requires the NuMA central coiled-coil and the C-terminal MT-BDs to generate proper spindle pulling forces in association with dynein.

1.3.1 The Dynein-1 complex

In this paragraph I will describe the structural details of the Dynein-1 complex and of the regulators that assemble and activate the complex on MTs.

In vertebrate cells, cytoplasmic Dynein-1 (here referred to as dynein) is the primary motor responsible for motility and force generation toward the minus-ends of MTs. Dynein drives long-distance transport of intracellular cargoes in the cytoplasm of interphase cells: it carries membrane-bound organelles (components of the endocytic pathway, Golgi vesicles, peroxisomes), viruses, transcription factors, misfolded proteins, and mRNA-containing particles toward the nucleus [73]. In neuronal axons, it is the only motor that drives retrograde transport toward the cell body. Consistent with its role as an essential retrograde motor, defects in dynein function impair neuronal integrity and lead to developmental and neurodegenerative disorders [74]. Dynein also plays critical roles in mitosis together with the protein NuMA, including positioning the spindle and focusing the MTs into poles (as discussed in paragraphs 1.1.1 and 1.1.2.1).

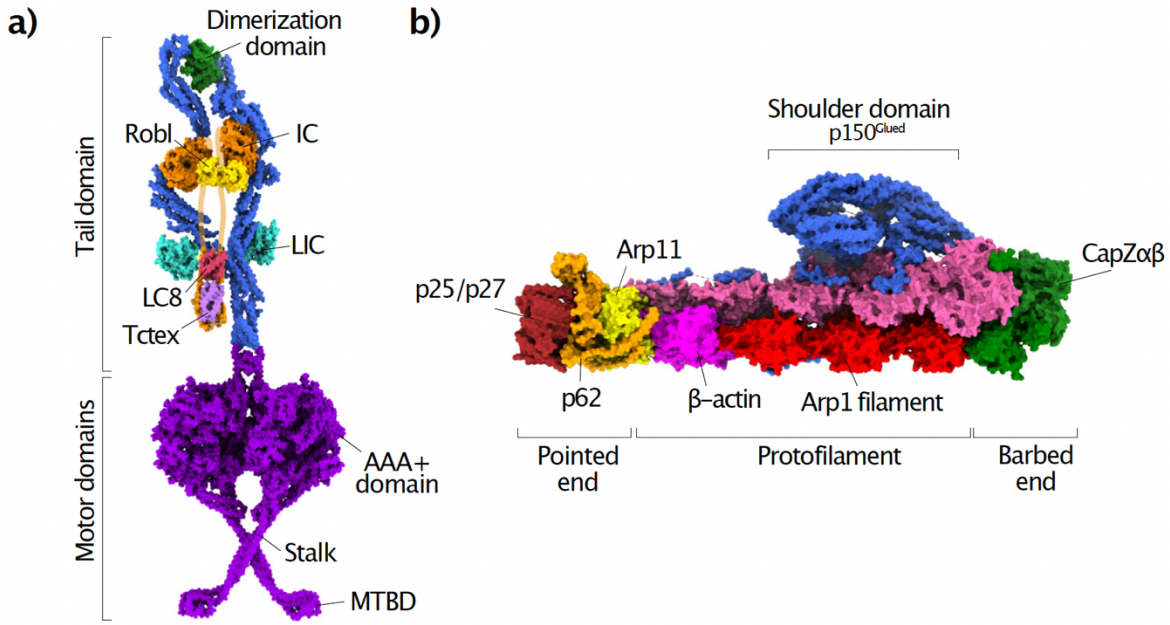

Figure 1.8 - The architecture of the dynein transport machinery

a) *Cryo-EM structure of the ϕ-particle conformation of the dynein complex (PDB ID: 5NVU).* ***b)*** *Cryo-EM structure of the dynactin complex (PDB ID: 5ADX). Adapted from Canty and Yildiz, Trends Biochem. Sci., 2020* [75].

Human dynein is a 1.4-MDa macromolecular complex composed of six polypeptide chains, each present in two copies (figure 1.8a). Dynein heavy chain (HC) (530 kDa) is the largest subunit and contains an N-terminal tail domain and a C-terminal catalytic motor domain of the AAA+ ATPase family [76]. The motor domain self assembles into a ring of six AAA+ modules that power dynein motility by ATP hydrolysis and binds to its track via a MT-BD located at the end of a long coiled-coil stalk. The tail domain is involved in the dimerization

of the HCs and contacts the AAA+ ring through a linker region, whose conformational changes contribute to dynein motility [76]. Two isoforms of several smaller non-catalytic components assemble on the N-terminal tail of dynein HC, including two intermediate chains (IC1-2), two light intermediate chains (LIC1-2), and two of the three light chains (LC1-2) Roadblock (Robl)/LC7, LC8 and Tctex, that are recruited by the ICs (figure 1.8a). In particular, LIC, the dynein subunit on which I will focus more in detail, comprises an N-terminal GTPase-like domain binding to dynein HC, followed by an extended C-terminal unstructured region contacting cargo adaptors (described in paragraph 1.3.1.1) [77].

The dynein transport machinery consists of dynein, a cargo adaptor and dynactin. The dynein essential cofactor dynactin is a 1.1 MDa complex composed of 23 subunits (figure 1.8b). It is built around two protofilaments that wrap around each other, containing eight copies of the actin-related protein 1 (Arp1) and one copy of β-actin. At the barbed (+) end, a CapZαβ heterodimer binds across both protofilaments. At the pointed (-) end, the filament is capped by another actin-related protein Arp11 that binds p25/p27 and p62, forming the pointed-end complex. On top sits the $p150^{Glued}$ subunit, which forms a large shoulder-like projection and contains an extended region consisting of three coiled-coil domains and an N-terminal Cap-Gly (cytoskeleton-associated protein glycine-rich) domain that binds to MTs [78]. Specifically, the Cap-Gly domain regulates the recruitment of dynactin to the MTs by binding to plus-end tracking proteins such as CLIP170 and end-binding (EB)1 [79], or through PTMs such as α-tubulin tyrosination, facilitating the assembly of the complex at the MT plus-ends [80] (figure 1.9). As mentioned in paragraph 1.2.1, in mouse keratinocytes the $NuMA^{1811-1985}$ fragment was found to interact with MT plus-ends without co-localizing with EB1, suggesting their mutually exclusive steric interactions or association with distinct MT end structures [45].

1.3.1.1 Assembly and activation of the Dynein transport machinery

Cryo-EM and *in vitro* reconstitution studies revealed that mammalian dynein adopts an autoinhibited conformation (ϕ-particle), where the motor domains self-dimerize in an antiparallel orientation, exhibiting low affinity to MTs and to the cofactor dynactin and little to no processive motility (figure 1.8a). Dynein remains in an inactive conformation on its own, and processive motility, the ability of the motor to take many steps before dissociating from its substrate, is activated when it forms a ternary complex with dynactin and an activating cargo adaptor protein. The cargo adaptor recruits and physically tethers dynein to specific intracellular cargoes and activates it for processive motility. Binding to dynactin and a cargo adaptor orients the dynein motor domains into a parallel conformation for processive movement along MTs [81–83]. Figure 1.9 shows a model of the assembly and activation of the

dynein-dynactin complex by the activating cargo adaptors BICD2 (Bicaudal D homolog 2) and BICDR1 (Bicaudal D-related protein 1): dynein and dynactin form a stable complex only in the presence of the N-terminal coiled-coil of the cargo adaptors that runs the length of the dynactin filament. This interaction activates dynein and primes it into a highly processive motor.

Recent cryo-EM studies have shown that the coiled-coil region of some cargo adaptors (as in the case of BICDR1 in figure 1.9) can extend along the dynactin filament to recruit a second dynein dimer to dynactin to increase the force production and velocity of the complex [84]. Activation of dynein motility is also regulated by accessory factors like the dimeric protein LIS1, which binds directly to the motor domain, promotes the formation of fully activated dynein-dynactin-cargo adaptor complexes containing two dynein dimers, and then dissociates from dynein leading to rapid motility [85] (figure 1.9).

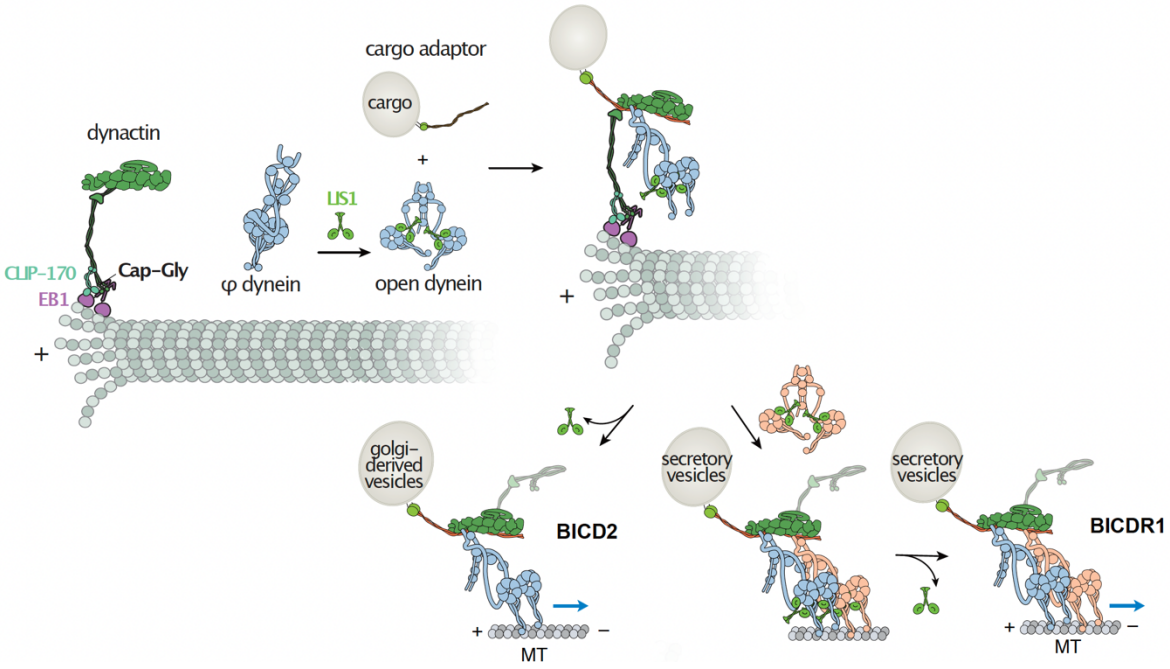

Figure 1.9 – Regulation of dynein motility by dynactin, an activating cargo adaptor and LIS1

Dynactin is recruited to MT plus-ends by the tip-tracking proteins EB1 and CLIP-170. LIS1 binds to the dynein motor domain and promotes the transition of dynein from the ϕ to the open conformation, which has higher affinity for dynactin. Plus-end localized dynactin recruits the cargo adaptor and LIS1-bound dynein in the open conformation to form the active complex. Following the complex assembly, LIS1 dissociates from dynein as it moves processively toward the MT minus-ends. The activating adaptor BICD2 is involved in the activation of dynein-driven transport of Golgi-associated vesicles, while BICDR1 activates the transport of secretory vesicles and can recruit a second open dynein dimer. Blue arrows indicate initiation of motility. Adapted from Canty et al., Annu. Rev. Biophys., 2021 [76], and Elshenawy et al., Nat. Cell Biol., 2020 [85].

Interestingly, a subset of cargo adaptors was found to be able to simultaneously recruit kinesin and dynein to the cargo, coordinating kinesin-dynein activity to determine which direction the cargo moves, therefore regulating bidirectional motility [86].

The activating adaptors identified so far through *in vitro* reconstitution experiments or studies in crude cell lysates are unrelated in sequence, instead the common features are the presence of a long N-terminal dimerizing coiled-coil, a binding site for the dynein subunit LIC, which can be either a *hook domain*, a globular domain located N-terminal to the coiled-coil, shared by Hook-family proteins, or a conserved coiled-coil motif, the *CC1-box* (consensus sequence: (D/E)xxxAAxxGxx(L/V), where x denotes any amino acid, figure 1.10g), shared by BICD2, BICDR1 and SPDL1 (spindle apparatus coiled-coil protein 1) (figure 1.10a), or pairs of *EF hands*. All of the adaptors identified thus far contain also a binding site for the dynactin pointed-end complex, the *spindly motif* (consensus sequence: L(F/A)xE, figure 1.10a), and a binding site for proteins that link the adaptors to their selective cargoes [73,87,88].

Lee and colleagues identified a conserved amphipathic helix within the unstructured C-terminal region of dynein LIC1 that mediates interactions with diverse hook domain and CC1-box containing adaptors [89].

The hook domain resembles the CH domain of tubulin-binding EB proteins, but cannot bind directly to MTs [90]. The CH module is common to various actin-binding proteins and is characterized by a globular α-helical fold, which is maintained by an hydrophobic core and contains seven α-helices in total [91] (figure 1.10b). The hook domain displays the canonical 7-helices of the CH-like fold, featuring an additional helix at the C-terminus termed helix α8 (figure 1.10c). This helix in the unbound structure of the hook domain of Hook3 is fully extended, since it interacts in an antiparallel fashion with the same helix from a symmetry-related molecule in the crystal lattice (figure 1.10f). This interaction is not physiological since Hook3$^{1-160}$ is monomeric, as determined by static light scattering (SLS) [87]. As shown in figure 1.10d, the structure of the LIC1 helix bound to the hook domain of Hook3 reveals that the helix α8 bends back to create a V-shaped hydrophobic cleft for binding of the LIC1 helix, like that of the uncomplexed structure of the hook domain of Hook1 (figure 1.10e). In figure 1.10d are highlighted the two strictly conserved hydrophobic phenylalanine residues in the middle of LIC1 helix (Phe447 and Phe448) that are part of the binding interface together with Hook3 surface residues Met140, Gln147 and Ile154 in helix α8 [87,89].

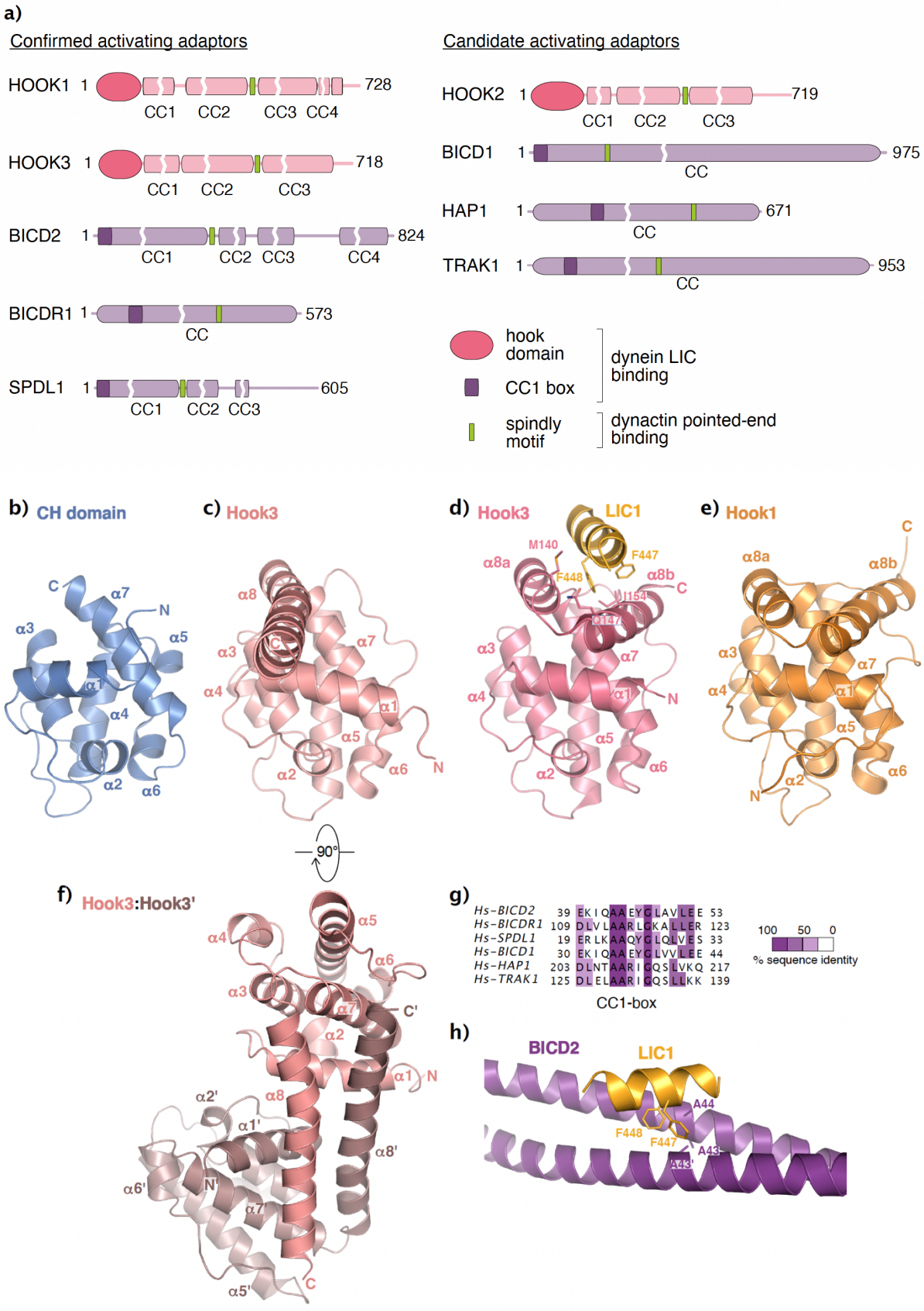

Figure 1.10 - The hook domain and the CC1-box for LIC1 binding in cargo adaptors

a) *Some examples of confirmed and candidate cargo activating adaptors (demonstrated or not to be active by in vitro motility assays) containing the hook domain (in dark pink) or the CC1-box (in dark violet) as dynein LIC binding site, and a spindly motif (in light green) binding to the dynactin pointed-*

end complex. ***b)*** *NMR solution structure of the CH domain located at the N-terminus of the actin binding protein Calponin (PDB ID: 1H67).* ***c-f)*** *Crystal structure of the hook domain of Hook3 at the two orthogonal views (PDB ID: 5J8E). In the orientation of panel f), the antiparallel interaction driven by the crystal lattice is visible.* ***d)*** *Crystal structure of the hook domain of Hook3 with a LIC1 peptide (PDB ID: 6B9H).* ***e)*** *NMR solution structure of the hook domain of Hook1 (PDB ID: 1WIX). The structures in panels b-e) were aligned with PyMOL in the same orientation.* ***g)*** *For the CC1-box, the Homo sapiens sequences of BICD2 (Uniprot entry Q8TD16), BICDR1 (Uniprot entry Q6ZP65), SPDL1 (Uniprot entry Q96EA4), BICD1 (Uniprot entry Q96G01), HAP1 (Uniprot entry P54257), and TRAK1 (Uniprot entry Q9UPV9) were aligned with CLUSTALΩ and coloured in Jalview by percentage of identity.* ***h)*** *Close-up view of the crystal structure of the CC1-box of BICD2 with a LIC1 peptide (PDB ID: 1H67).*

Recently Lee and colleagues also determined the crystallographic structure of the CC1-box of BICD2 in complex with LIC1 helix. As shown in figure 1.10h, residues Phe447 and Phe448 on the hydrophobic face of LIC1 helix insert into an hydrophobic pocket formed at the interface between the two chains of the coiled-coil BICD2 by highly conserved alanine and glycine residues in the CC1-box [92].

SPDL1 and Hook2 are the only mitotic dynein-dynactin adaptors identified so far (figure 1.10a), with SPDL1 the only one demonstrated to activate dynein by *in vitro* motility reconstitution assays with purified components [82]. While SPDL1 targets dynein-dynactin to the kinetochore for spindle assembly checkpoint inactivation and sister chromatid separation [88], Hook2 promotes centrosome separation at mitotic entry, astral MT nucleation and cytokinesis, and its depletion results in spindle pole defects and spindle misorientation [17].

Several lines of evidence support the notion that NuMA is the mitotic dynein-dynactin adaptor responsible for spindle orientation activities. As already discussed, NuMA anchors dynein at the cell cortex, where it captures the plus-ends of dynamic MTs. NuMA is a good candidate that can function similarly to known dynein LIC-binding cargo adaptors, since it has an N-terminal globular head predicted to fold as a CH domain, a long coiled-coil region and a spindly-like motif (figure 1.6b), which are all essential features for cortical dynein recruitment [53].

1.4 Functions of NuMA in the nucleus

NuMA accumulates in the nucleus in interphase (figure 1.11a), then leaves the nucleus in prometaphase, and localizes back to the nucleus upon nuclear envelope reformation in telophase (figure 1.11b), since it contains a tripartite NLS in its C-terminus: the highly conserved Lys1988-Arg1989, His1995, and Lys2004-Lys2005 NuMA residues (highlighted

in the sequence alignment of figure 1.6c) interact respectively with the minor site, the linker region, and the major site on Importin-α [52]. Importin-β bound to Importin-α sterically inhibits NuMA MT-BD2 *in vitro* and a Ran-GTP-independent pathway dissociates NuMA from Importins in the nucleus and activates it away from chromosomes [9,52]. CDK1-mediated phosphorylation in late-prophase is also involved in the release of NuMA from chromatin at mitotic onset [63].

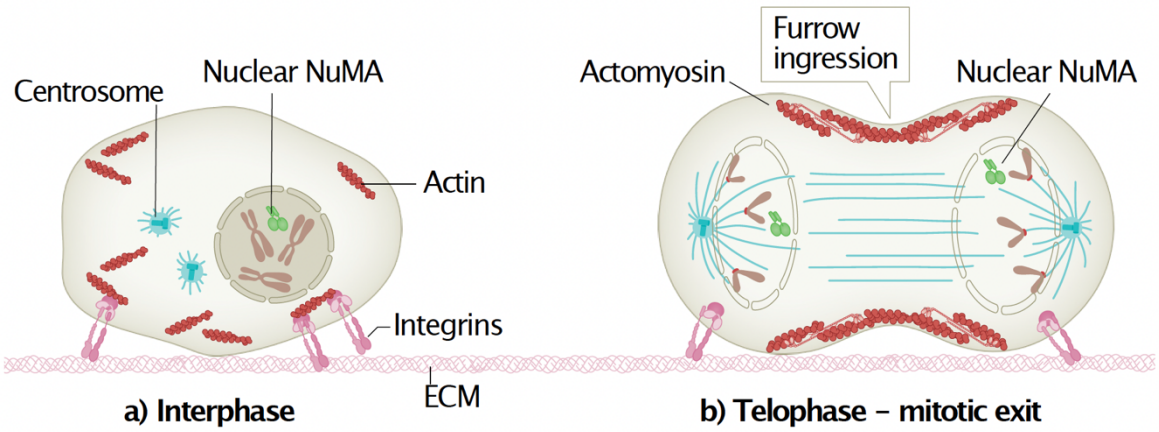

Figure 1.11 - NuMA nuclear localization in interphase and telophase

a) Interphase. *In the interphase nucleus NuMA is involved in nuclear mechanics [56], regulation of gene expression [93], and DNA repair [2].* ***b) Telophase.*** *At mitotic exit, nuclear NuMA functions in the regulation of chromosome decondensation and in nuclear reformation [56,63]. Adapted from Lechler and Mapelli, Nat. Rev. Mol. Cell Biol., 2021 [20].*

Electron microscopy studies revealed that NuMA organizes high-ordered structures in the interphase nucleus to generate a mechanically robust nucleus [94].

NuMA was defined for years as a "nuclear matrix" protein, being a structural constituent of the insoluble nuclear scaffold [95], and was reported to interact *in vitro*, through its negatively charged N- and C-terminal S/TPXX motifs, with defined AT-rich DNA sequences called matrix attachment regions (MARs), fastening chromatin to the nuclear matrix [96].

Recently, Rajeevan and colleagues demonstrated that the basic amino acids within the C-terminal region of NuMA encompassing residues 2058-2115 (figure 1.6d) are sufficient to bind DNA *in vitro* and to interact with chromatin in cells. When endogenous NuMA is replaced with mutated versions lacking this DNA-binding region, HeLa cells show improper chromosome decondensation during mitotic exit and an abnormal nuclear shape in interphase, due to the potential of NuMA-ΔDNA-BD to polymerize into higher-order fibrillar structures capable of mechanically deforming the nuclear envelope [63]. This suggests that NuMA-DNA interactions are critical for proper regulation of chromatin decompaction

during nuclear reformation and for maintaining the proper nuclear architecture (figure 1.11b) [63]. Furthermore, Serra-Marquez and colleagues, by inducing mitotic exit in NuMA knockout (KO) RPE-1 cells without spindles, demonstrated that the NuMA contribution to nuclear formation is independent from its mitotic functions. NuMA promotes nuclear mechanical robustness, offering structural support throughout the nucleus by cross-linking chromosomes and preventing the nuclear envelope from penetrating into the chromosome mass [56].

NuMA contributes to several interphase events, including chromatin organization, gene expression, and DNA repair. NuMA is known to influence higher order chromatin organization [97], to regulate p53-dependent gene transcription [93] and to interact with transcription-associated proteins, such as GAS41 (glioma-amplified-sequence 41) [98]. Even though immunofluorescence studies have always shown a nuclear NuMA localization excluded from nucleoli, recently Jayaraman and colleagues provided evidence that NuMA is present in the nucleolus and participates in rDNA transcription, and that downregulation of NuMA expression induces a p53-independent nucleolar stress response [99].

1.4.1 NuMA roles in the regulation of DNA double-strand break (DSB) repair

NuMA plays an important role in the DNA DSB signalling, which is critical for the maintenance of cellular homeostasis and genome integrity.

Unrepaired DSBs can trigger cell cycle arrest and cell death. Two mechanistically distinct pathways are involved in the repair of DSBs: non-homologous DNA end-joining (NHEJ), which rejoins the broken ends without the use of homology [100] and homologous recombination (HR) [101], which requires an identical DNA template in the sister chromatid for DNA repair (figure 1.12b).

The DDR initiates with the recruitment and activation of the serine/threonine kinase ataxia-telangiectasia mutated (ATM) at DNA DSBs by the MRE11-RAD50-NBS1 (MRN) complex. ATM phosphorylates several key DNA repair proteins including 53BP1, BRCA1 (breast cancer type 1 susceptibility protein) and H2AX. Poly (ADP-ribose) polymerase (PARP) proteins play also a key role in DNA repair, mediating poly-ADP-ribosylation of proteins [102].

NuMA is phosphorylated at Ser395 by ATM [103] in response to ionising radiation (IR) (figure 1.6b) and accumulates at sites of DNA damage in a PARP-dependent manner [104], since it is PARsylated by the telomeric protein tankyrase 1 and interacts with PARP3 [105,106]. Silencing of NuMA gene impairs H2AX phosphorylation (known as γH2AX), which in turn

participates in the recruitment and retention of DDR proteins, including repair factors and chromatin remodelling complexes at DSB sites [107].

The mechanisms regulating the access of repair factors to chromatin in the absence of DNA damage are largely unexplored. Such mechanisms may be the key to prevent undue activation of the DDR. Recently, Moreno and colleagues reported that NuMA interacts with 53BP1, a component of the DNA damage foci, and controls its diffusion throughout the nucleoplasm, sequestering it in the absence of DNA damage [2]. In this context, NuMA phosphorylation by ATM at Ser395 serves as a release mechanism, allowing 53BP1 accumulation at damaged chromatin [2]. 53BP1 plays an important role in the DNA repair pathway choice: it competes with BRCA1 and, consequently, antagonizes HR in favour of NHEJ (figure 1.12b). The negative regulation of 53BP1 DSB repair function is consistent with the NuMA pro-HR activity [104]. NuMA has also been reported to interact with the chromatin remodeler ISWI ATPase SNF2h, regulating its accumulation at DNA damage sites [104]. Chromatin remodelling factors play an active role in the DDR by shaping chromatin to facilitate the repair process. Therefore, the control of the activity of SNF2h corroborates a function for NuMA also in chromatin remodelling.

1.4.2 The DNA damage response (DDR) protein 53BP1

As mentioned in the previous paragraph, the DDR factor 53BP1 is a central mediator and effector of chromatin based DSB signalling. It localizes specifically to damaged chromatin and preserves genomic integrity by coordinating DSB repair pathway choice, favouring repair by NHEJ during the G1 phase of the cell cycle over BRCA1-dependent HR occurring in S-G2, by antagonizing DSB resection (figure 1.12b). 53BP1 plays a prominent role in determining the efficacy of PARP1 inhibitory drugs ($PARP_i$) in BRCA1-deficient cancers and promotes the end-joining of distal DNA ends, such as during the fusion of deprotected telomeres [108] as well as during V(D)J recombination and class switch recombination (CSR), which are important for a functional adaptive immune response [109,110].

In response to DSBs, 53BP1 rapidly accumulates on the chromatin surrounding the break site. 53BP1 recruitment can be monitored by microscopy to track the formation of subnuclear foci at damaged chromatin (figure 1.12a). The stable association of 53BP1 with DSBs is driven by a signalling cascade that is initiated by the ATM-mediated phosphorylation of H2AX at Ser139 (γH2AX), followed by the recruitment of MDC1 (mediator of DNA damage checkpoint protein 1**)** and activation of RING finger protein 8 (RNF8)-RNF168-dependent chromatin ubiquitylation [109] (figure 1.12b).

The domain structure of human 53BP1 consists of 28 N-terminal Ser/Thr-Gln sites, which are phosphorylated by the ATM kinase in response to DSBs, followed by the ionizing radiation-induced foci (IRIF) region, and the BRCA1 C-terminal (BRCT) repeats that bind to γ-H2AX and EXPAND1 and that are dispensable for the focal recruitment of 53BP1 (figure 1.12c). 53BP1 acts as a scaffold that recruits to damaged chromatin additional DSB-responsive proteins such as RIF1 (replication timing regulatory factor 1) and PTIP (PAX transactivation activation domain-interacting protein), which interact with ATM-phosphorylated residues in 53BP1 [111]. The IRIF region, the minimal domain necessary for the focal recruitment of 53BP1 to DSBs, spans the dynein light chain LC8 binding motif that promotes 53BP1 oligomerization and stimulates the recruitment of 53BP1 to sites of DNA damage [112], the oligomerization domain (OD), a Gly- and Arg-rich (GAR) motif, a tandem Tudor domain, an ubiquitylation-dependent recruitment (UDR) motif, and a NLS [113] (figure 1.12c).

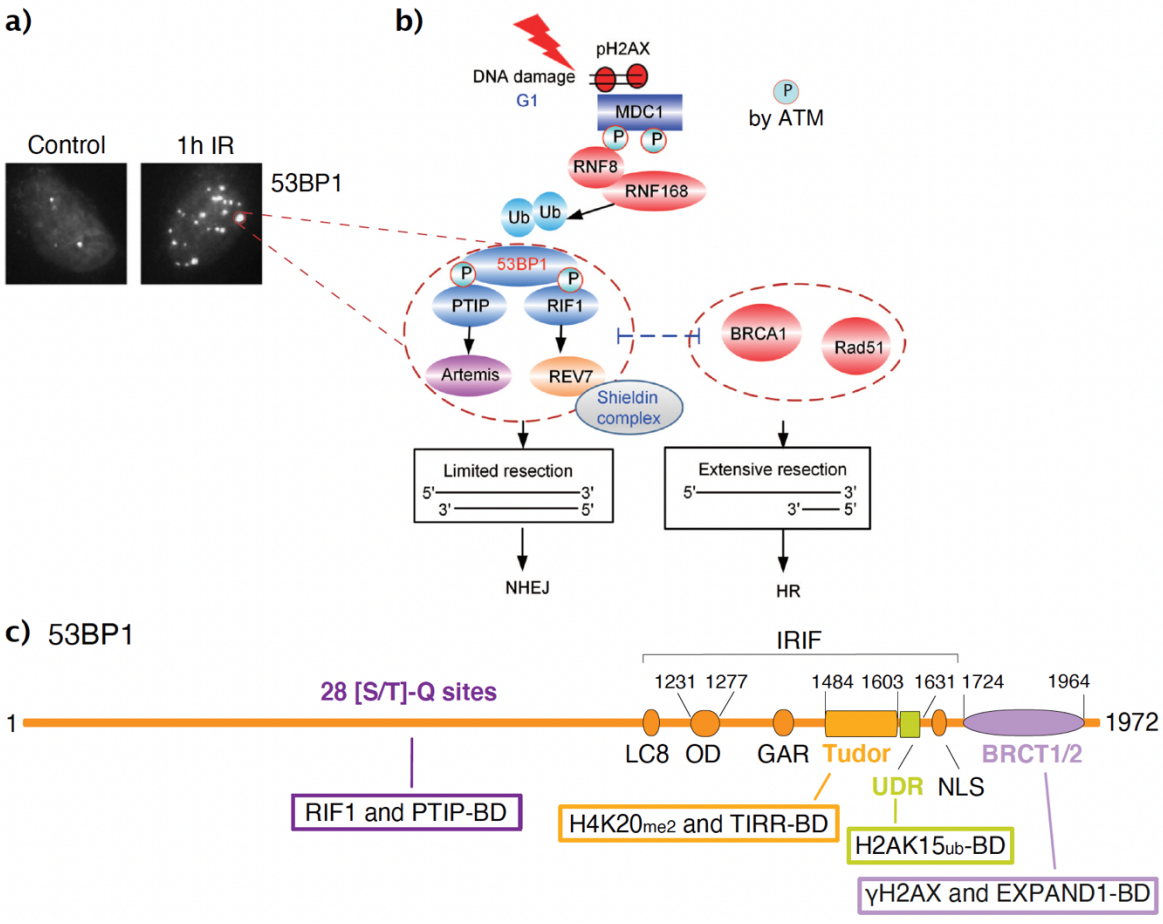

Figure 1.12 – 53BP1 as a key determinant of DNA DSB repair

a) *Representative confocal images of U2OS cells treated or not with 0.5 Gγ of IR, allowed to recover for 1h, and stained for 53BP1. The formation of 53BP1 DNA damage foci is visualized.* ***b)*** *Regulation of DSB repair pathway choice (NHEJ vs HR): focus on the 53BP1 protein. In response to DNA*

damage in G1, 53BP1 recruits to sites of DNA breaks two downstream sub-pathways that are mediated by PTIP-Artemis and RIF1-REV7-Shieldin complex, restricting DSB resection and counteracting BRCA1-dependent HR-mediated DNA repair. ***c)*** *Domain structure and interaction partners of human 53BP1-1. 53BP1 is a large scaffold protein that contains interaction surfaces for numerous DSB-responsive proteins and for specific epigenetic histone marks, as described in the text. Adapted from Zhang and Gong, J. Zhejiang Univ. Sci. B, 2021* [113]*, and Kilic et al., EMBO J., 2019* [114].

The recruitment of 53BP1 to damaged chromatin depends on combinatorial PTMs. 53BP1 is a bivalent histone modification reader that directly recognizes a DSB-specific histone code: the Tudor and UDR domains in the IRIF of the protein interact respectively with constitutive di-methylated Lys20 of histone 4 (H4K20me2) and with damage-induced RNF168-mediated mono-ubiquitylated Lys15 of histone H2A (H2AK15ub) [115–117] (figure 1.12c). Hence, multiple independent histone marks cooperate to recruit 53BP1 to the chromatin surrounding the DSB and this accumulation is even further stimulated by the OD and the LC8 domains of the protein [110]. Furthermore, the nuclear kinesin-8 family member KIF18B contains a Tudor-interacting motif that, in response to damage, enhances the interaction between the 53BP1 Tudor domain and H4K20me2 [118].

In the absence of DNA damage, the Tudor-interacting repair regulator (TIRR) directly binds the 53BP1 tandem Tudor domain and masks its H4K20me2 binding motif (figure 1.12c). Upon DNA damage, the 53BP1-TIRR complex is dissociated, leading to 53BP1 accumulation at chromatin proximal to DSBs [119].

1.4.2.1 The role of 53BP1 in the centrosome surveillance pathway

53BP1 assembly in DNA damage foci is precluded during mitosis, when CDK1 activity is high and chromosomes are heavily condensed. Mitotic phosphorylation of 53BP1 by CDK1 and PLK1 impairs the ability of 53BP1 to bind H2AK15ub and to properly localize to the sites of DNA damage [120] (figure 1.13a).

53BP1 has a mitotic role in the centrosome surveillance pathway that does not require its recruitment to sites of DNA damage. The centrosome surveillance pathway triggers cell cycle arrest to block the growth of potentially unfit daughter cells and is activated by both centrosome loss and prolonged mitosis [121] (figure 1.13b). 53BP1 mediates signalling through the mitotic surveillance pathway together with the deubiquitinase USP28 (ubiquitin carboxyl-terminal hydrolase 28), adopting noncanonical roles to function in this pathway. 53BP1 and USP28 act upstream of p53, leading to the activation of the p53 signalling pathway for cell cycle arrest (figure 1.13b). Both USP28 and p53 interact with the tandem-

BRCT domains of 53BP1, which, as mentioned before, are dispensable for the DNA damage response activity of 53BP1 (figure 1.13a). Therefore, this new 53BP1 function in the centrosome surveillance pathway is independent of its canonical role in DNA damage signalling. Notably, the 53BP1-USP28-p53 signalling module regulates centrosome integrity without localizing to centrosomes [122].

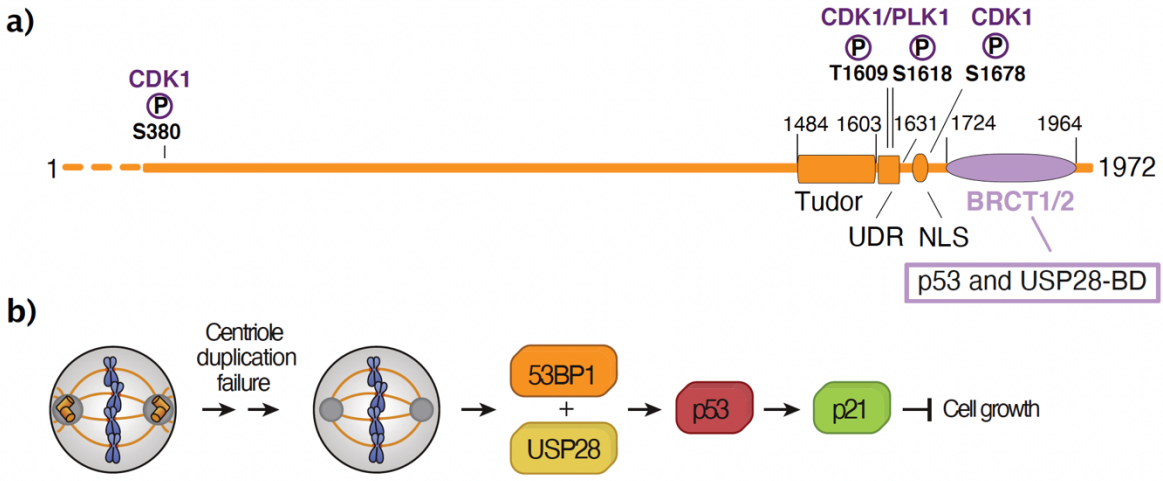

Figure 1.13 – Mitotic regulation of 53BP1

a) *Domain structure of 53BP1 with highlighted the CDK1 and PLK1 phosphorylation sites. 53BP1 interacts with USP28 and p53 through its C-terminal BRCT repeats.* ***b)*** *A scheme of the mitotic surveillance components involved in cell cycle arrest following centrosome loss. Adapted from Lambrus and Holland, Trends Cell Biol., 2017* [121].

1.5 The liquid-liquid phase separation (LLPS) process

LLPS is recently emerging as a mechanism to dynamically sub-divide the intracellular space in membrane-less compartments such as the nucleolus, nuclear speckles, RNA granules, silent heterochromatin domains, gene promoters, super-enhancers, and DNA damage foci [123] (figure 1.14a). Its misregulation is associated with the emergence of diverse pathologies, such as neurogenerative diseases and cancer [124,125].

LLPS is a process in which a solution of proteins spontaneously separates into two phases, a dense phase that is enriched for the macromolecules and a surrounding dilute phase that is depleted of the macromolecules. Because the formed dense phase allows selective access of certain macromolecules and exchanges components with its surroundings, it can function as a dynamic compartment with properties of liquid condensates. Proteins that mediate phase separation in the cellular environment often contain multiple self-interaction domains and have a high fraction of intrinsic disorder. Maintenance of these droplet compartments requires a network of interactions, many of which are weak and transient [126].

Protein condensation has been shown to be driven by the action of both electrostatic and hydrophobic interactions, including charge-charge, cation-π, dipole-dipole, and π-π stacking interactions (figure 1.14b). Liquid condensates dissociate when exposed to a range of additional components acting as phase separation disruptors, such as 1,6 hexanediol, an aliphatic alcohol that disrupts weak protein-protein hydrophobic interactions and selectively dissolve liquid condensates, and ATP and poly-uridine (polyU) RNA, both highly negatively charged molecules with the ability to modulate electrostatic and polar interactions [127] (figure 1.14c).

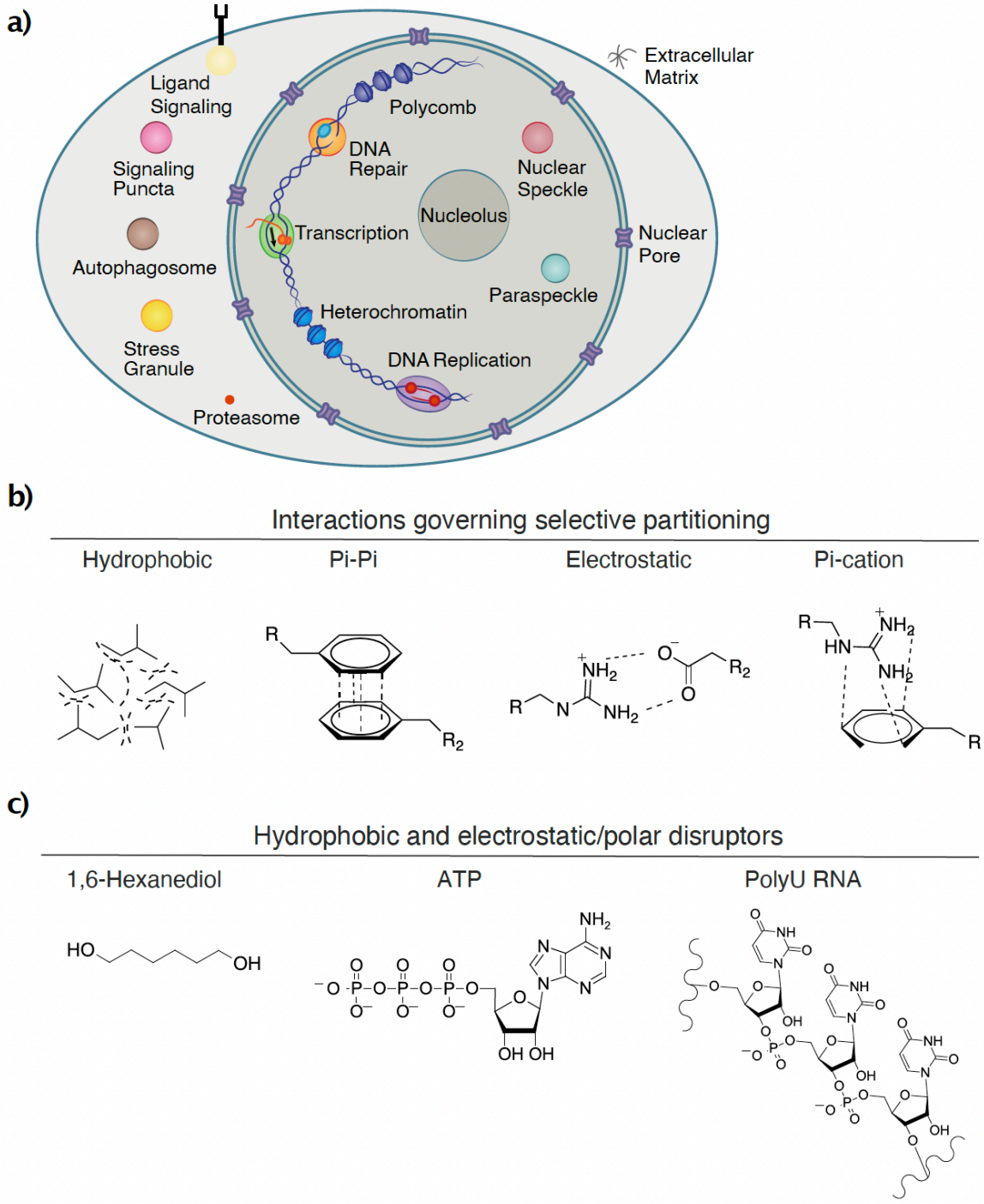

Figure 1.14 – Intracellular liquid phase condensation

a) *Schematic of the numerous condensates in the nucleus, cytoplasm and membranes of eukaryotic cells.* ***b)*** *Overview of different kinds of contacts, which have been observed in protein phase separation.* ***c)*** *Phase separation disruptors can be hydrophobic, such as 1,6-hexanediol, or electrostatic/polar, such as ATP and PolyU RNA. Adapted from Boija et al., Cancer Cell, 2021* [125]*, and Krainer et al., Nat. Commun., 2021* [127]*.*

Condensates can be spatiotemporally regulated by protein concentration, RNA molecules and PTMs [128].

Most notably, examples of phase-separating proteins are 53BP1 in the DNA damage foci [114] and TPX2 in the regulation of MT nucleation [129].

53BP1 foci at DSBs show LLPS characteristics as 1,6 hexanediol treatment perturbs 53BP1 liquid-like droplets [130]. 53BP1 undergoes phase separation and both the OD and the BRCT domains contribute to this behaviour *in vivo*. These domains are required for the stabilization of p53 and to promote global p53 target gene expression [114]. Surprisingly, both p53 and its co-activator USP28 were found enriched in 53BP1 nuclear bodies, suggesting that phase-separated 53BP1 compartments might play a role not only for the DNA damage response, but also for the mitotic surveillance pathway [114].

The OD promotes self-assembly of 53BP1 into phase-separated condensates, that recently Ghodke and colleagues found to be regulated by the large scaffolding protein AHNAK [131].

1.6 Aim of the project

My PhD project is divided into two parts. In the first part I focused on the characterization of the interaction between the N-terminal region of NuMA and the dynein-dynactin complex in mitosis, which I carried out with other members of the group and was published last year on *Structure* [1]. In the second part of the project, I dissected with biochemical approaches the NuMA-53BP1 binding interface and characterized the LLPS properties of the C-terminal portion of NuMA, potentially involved in the regulation of the interaction with the DNA damage response protein 53BP1 in the nucleus outside DNA damage foci and/or in mitosis.

<u>Aim 1: organizational principles of the NuMA-dynein interaction interface and implications for mitotic spindle functions</u>

Optogenetic approaches conducted in human HeLa and HCT116 cells showed that direct targeting of endogenous dynein to the cortex is insufficient to move the spindle, suggesting that effective pulling is promoted by a defined spatial organization of cortical dynein-dynactin complexes in specialized clustered focal structures assembled by the protein NuMA

[53]. NuMA is supposed to be the mitotic dynein-dynactin adaptor responsible for spindle orientation activities. Accordingly, binding of NuMA to dynein-dynactin is required for its cortical targeting, and hence for spindle positioning [32,53]. Mapping experiments revealed that the NuMA portion encompassing the first 705 residues is sufficient for the interaction with dynein and dynactin [32]. However, the structural details of the NuMA-dynein interaction interface are not well known. As discussed before, NuMA contains at the N-terminal region a CH-like domain, a long coiled-coil, and a spindly-like motif (figure 1.6b), essential for cortical dynein recruitment, which suggest that NuMA could function similarly to known cargo adaptors interacting directly with the dynein LIC subunit.

To address the putative dynein activating adaptor function of NuMA, we set out to characterize the organizational principles of the NuMA-LIC interaction with structural and biochemical assays. Since NuMA plays essential functions in mitotic spindle assembly and positioning, we decided to study the relevance of the NuMA-LIC interaction in mitotic HeLa cells.

Aim 2: organizational and functional principles of the NuMA-53BP1 interaction

During interphase, NuMA regulates the diffusion of 53BP1 outside DNA repair foci. 53BP1 interacts with NuMA by co-IP and this interaction is reduced after DNA damage induction using laser-microirradiated tracks in U2OS cells, suggesting that NuMA prevents 53BP1 accumulation at DNA breaks and sequesters 53BP1 in the absence of DNA damage [2]. The protein TPX2 together with Aurora-A has a similar role during replication stress by counteracting 53BP1 function [132]. Since NuMA was recently found to be part of the same complex with TPX2 in mitosis [133] we hypothesized that NuMA could work with TPX2 in regulating the DNA damage response via 53BP1. However, the molecular basis under this interaction is completely not known.

Both 53BP1 and TPX2 have been shown to undergo LLPS [114,129]. Since we discovered that NuMA has an intrinsically disordered C-terminal region with the potential to form liquid droplets, we hypothesized that the regulation of 53BP1 by NuMA and TPX2 could occur by forming dynamic LLPS condensates.

Therefore, the set out to map the domains of the large proteins NuMA and 53BP1 involved in the interaction and then we analysed the LLPS properties of NuMA through *in vitro* droplets assays.

2. RESULTS: molecular insights into the NuMA-dynein mitotic complex

I started this first project aiming at characterizing the interaction interface between NuMA and dynein, and its relevance for mitotic spindle assembly and orientation functions during my master internship, in which I characterized biochemically the N-terminal region of NuMA, and I obtained NuMA$^{1-153}$ crystals. The crystallographic structure of the N-terminus of NuMA was solved by Sebastiano Pasqualato, the Head of the Biochemistry and Structural Biology Unit at IEO, and Manuel Carminati, the PhD student that followed me at the time. During the first years of my PhD, I continued to dedicate myself to the biochemical characterization of the NuMA-dynein interaction together with the now post-doctoral fellow Francesca Rizzelli. I performed SEC and isothermal titration calorimetry (ITC) experiments to test the proteins' direct interaction and I generated and purified all the constructs used in the pulldown experiments. The cell biology functional assays were performed by the technician Chiara Gaddoni with the help of the post-doctoral fellow Laura Pirovano.

2.1 NuMA$^{1-705}$ is the shortest fragment retaining full binding to dynein and dynactin

As explained in the introduction (paragraph 1.2.1), the N-terminal region of NuMA encompassing residues 1-705 is the dynein-dynactin-BD identified in 2012 by Kotak and colleagues by co-IP experiments with mitotic HeLa cell lysates and GFP-NuMA transfected constructs [32].

To validate the interaction between purified NuMA N-terminus and dynein-dynactin and to identify the minimal BD on NuMA, I performed a maltose binding protein (MBP) pulldown assay using bacterially purified MBP-tagged NuMA N-terminal constructs as bait (spanning residues 1-705, 1-400, 1-260, and 1-153, figure 2.1a), and testing their ability to pulldown endogenous dynein and dynactin from HEK293T cells blocked in mitosis by 16 h nocodazole treatment. Nocodazole is a drug that depolymerizes astral MTs, causing cells to arrest in prometaphase. As shown in figure 2.1b and in the quantifications of panels c and d, NuMA$^{1-705}$ was demonstrated to be the shortest fragment retaining full binding to dynein and dynactin. This technique of pulldown with cell lysates allows to use a higher concentration of bacterially produced bait proteins on beads as compared to co-IP, keeping all the PTMs on the endogenous prey proteins potentially needed for the interaction.

Therefore, this result suggests that NuMA$^{1-705}$ does not require PTMs to bind to dynein and dynactin.

This data is consistent with the ability only of NuMA$^{1-705}$ and of NuMA$^{1-505}$ to recruit the dynein complex to the cell cortex [53]. In optogenetic reconstitution assays in human cells, neither the globular head alone (residues 1-213), nor the fragment lacking the globular head (residues 214-705), nor the fragment lacking the spindly-like motif (residues 1-413) were found to be sufficient for the cortical dynein recruitment [53]. We conclude that NuMA$^{1-705}$ requires both the N-terminal globular domain and the initial coiled-coil region until residue 705 to keep dynein and dynactin together in a stable complex.

Of note, in this case we decided to perform an MBP pulldown since the dimeric GST may interfere with the dimeric nature of the NuMA coiled-coil.

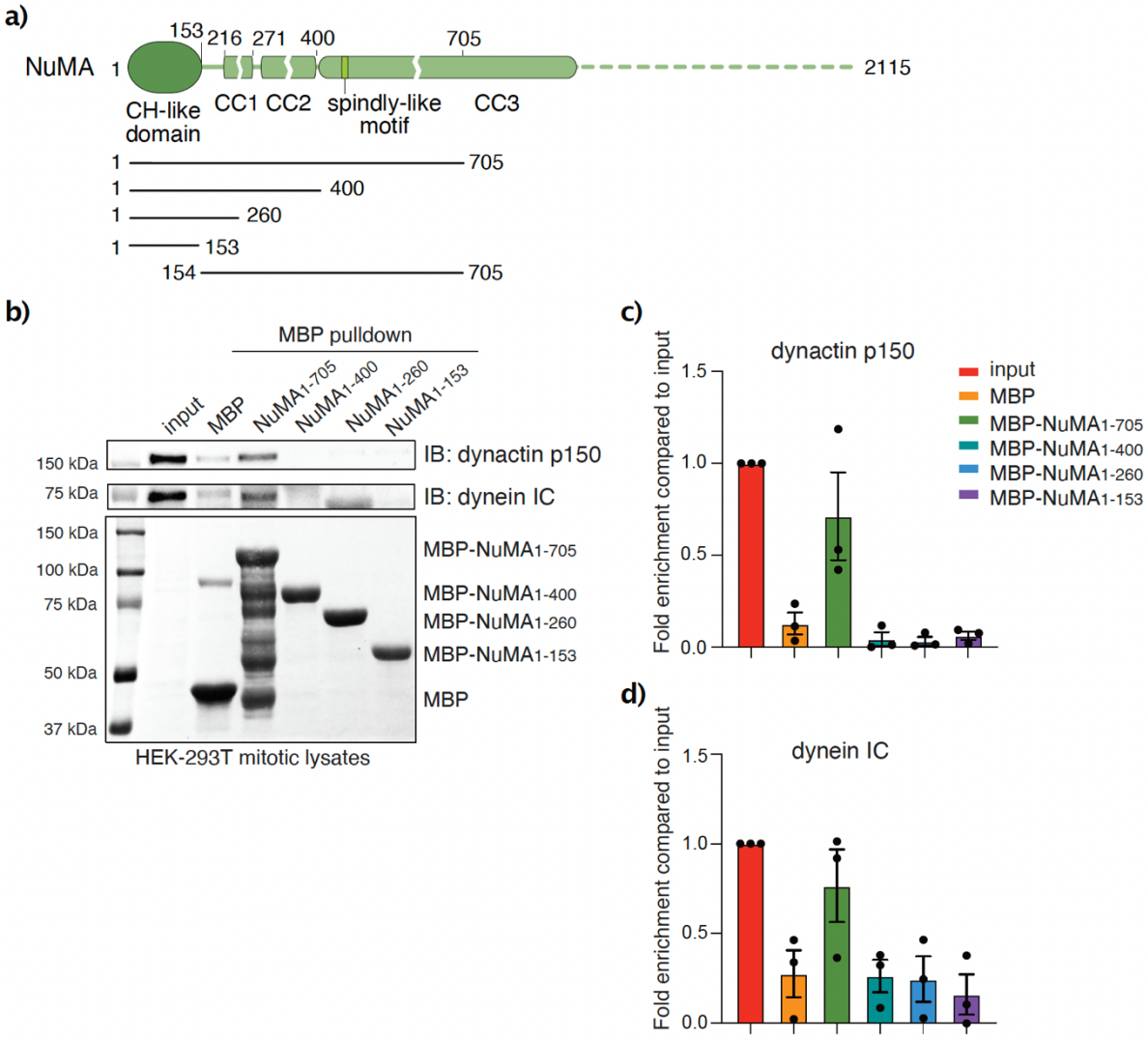

Figure 2.1 – NuMA$^{1-705}$ binds to dynein-dynactin in HEK293T mitotic cell lysates

a) *Schematic representation of the domain structure of human NuMA N-terminal region. Bold lines with numbers indicate protein subdomains used in the bottom experiments.* ***b)*** *MBP pulldown*

experiment with 5 μM of MBP-tagged NuMA N-terminal constructs bound to amylose resin, and 2 mg of HEK293T mitotic cell lysates. MBP was included in the experiment as negative control. Species retained on beads were analysed by immunoblotting for dynein IC and the p150^{Glued} subunit of dynactin, 5 μg of lysate were loaded as input. The amount of MBP and of each MBP-NuMA construct was assessed by ponceau staining (bottom panel). ***c-d)*** *Quantification of bound dynactin p150^{Glued} and dynein IC levels normalized to input signals. Error bars represent SEM from three independent experiments.*

2.2 NuMA$^{1-705}$ consists of a monomeric head and a dimeric coiled-coil

To start inspecting biochemically the NuMA dynein-dynactin-BD (NuMA$^{1-705}$), I first set out to purify the construct from bacterial sources. The sample was expressed and purified to homogeneity, adopting a stepwise purification protocol, comprising affinity chromatography on NTA-beads, ion-exchange chromatography (IEC) and SEC, as described in the materials and methods section (paragraph 5.2). SEC analysis consists in the separation of proteins according to their size and shape. On a Superose-6 10/300 size-exclusion column, NuMA$^{1-705}$ elutes in a single peak, although at higher M_w then the theoretical one of 80 kDa, just after the void volume, the elution volume of solutes that do not enter the pores of the chromatography resin (figure 2.2a, red profile). This evidence suggests that the construct is oligomeric or elongated in solution.

To determine the oligomerization state of NuMA$^{1-705}$, we used a size-exclusion column coupled to SLS instrument (see paragraph 5.3). SLS is an optical technique that measures the absolute M_w of a molecule, regardless of its shape, by recording the intensity of the light scattered by the sample in solution. Larger proteins scatter proportionally more light than smaller ones.

SLS analysis performed on the bacterially purified protein NuMA$^{1-705}$ revealed the presence of different oligomeric populations (figure 2.2c-f), despite its elution as a single peak from gel filtration (figure 2.2a, red profile). Therefore, we generated two shorter constructs (NuMA$^{1-153}$ and NuMA$^{154-705}$) by molecular cloning and site-directed mutagenesis (paragraph 5.1). NuMA$^{1-153}$ and NuMA$^{154-705}$ were expressed and purified to homogeneity from bacterial sources, as for NuMA$^{1-705}$ (see paragraph 5.2 for details). As shown in figure 2.2b, NuMA$^{1-153}$ elutes from the SEC column as a monodisperse monomer. We further checked the monodispersity of the sample by SLS, which confirmed the presence of a homogeneous population of molecules with a M_w consistent with the theoretical one of 17.4 kDa (figure 2.2d-f). The purified NuMA$^{154-705}$, which comprises the coiled-coil portion, elutes at the same M_w of NuMA$^{1-705}$ on the size-exclusion column (figure 2.2a, orange

profile), but from SLS analysis we appreciated that the construct is dimeric, as the measured M_w is double the theoretical one (figure 2.2e-f).

Based on the SEC and SLS data on the NuMA N-terminal constructs, we conclude that the globular domain of NuMA spanning residues 1-153 is monomeric in solution, while from residue 154 onward a dimerizing portion starts.

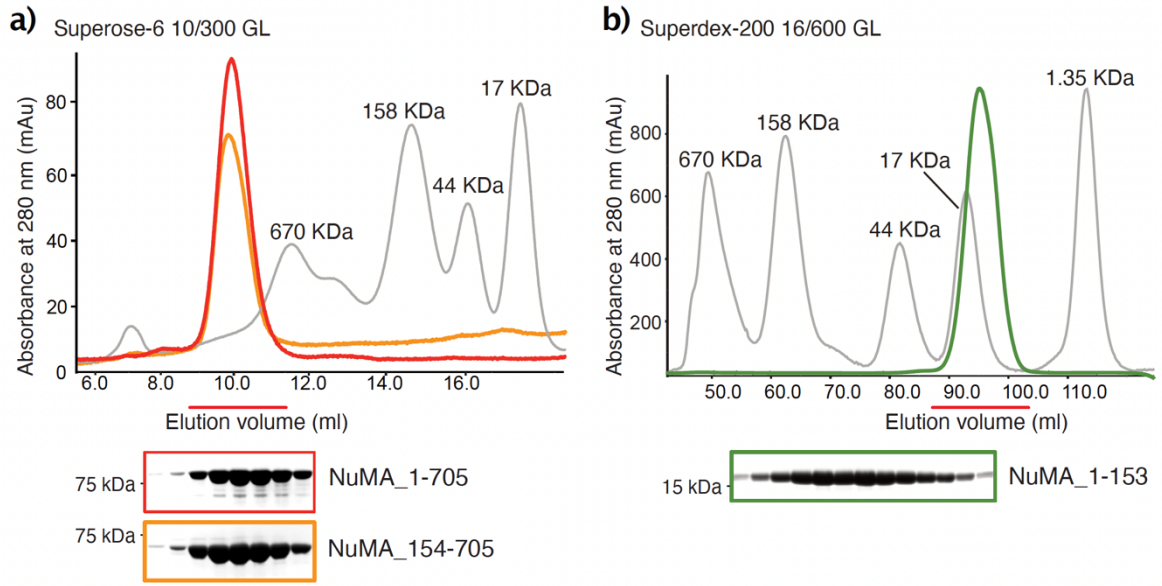

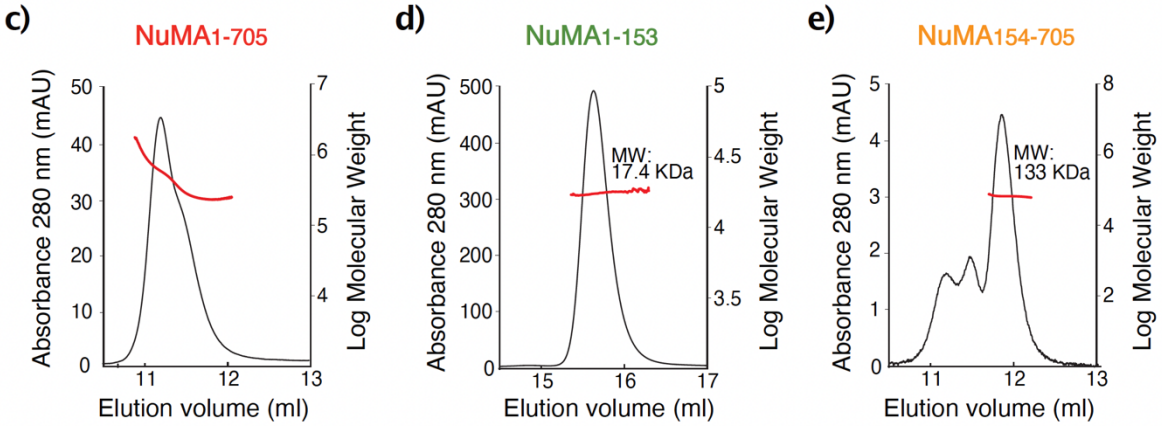

f)

	Molecular Weight (KDa) theoretical monomer	dimer	measured (SLS)
NuMA1-705	80	160	/
NuMA1-153	17.4	/	**17.4**
NuMA154-705	64	128	**133**

Figure 2.2 – SEC and SLS analyses on NuMA N-terminal constructs

a) *Representative SEC analyses on NuMA$^{1-705}$ and on NuMA$^{154-705}$ loaded on a Superose-6 10/300 column. The protein elution profiles are shown in red and orange, respectively, and are overlaid with the trace of globular M_w markers (grey line). The peak fractions corresponding to the horizontal*

red bar were separated by SDS-PAGE and visualized by Coomassie-staining. ***b)*** *Representative SEC analysis on NuMA$^{1-153}$ performed on a Superdex-200 16/600 column. The protein elution profile is shown in light green.* ***c)*** *SLS analysis on NuMA$^{1-705}$ indicating that the sample is polydisperse in solution.* ***d)*** *SLS analysis on NuMA$^{1-153}$ indicating that the sample is monodisperse and monomeric in solution.* ***e)*** *SLS analysis on NuMA$^{154-705}$ indicating that in solution the sample is polydisperse with a main dimeric population.* ***f)*** *Table indicating the theoretical and measured M_w of the proteins analysed by SLS.*

2.3 NuMA$^{1-705}$ interacts directly with dynein LIC1 and LIC2

NuMA can be considered as a candidate dynein-dynactin activating adaptor in mitosis, since its N-terminal domain (residues 1-705), which comprises a long coiled-coil portion, interacts with dynein and dynactin [32] (paragraph 2.1).

As described in the introduction (paragraph 1.3.1.1), the common features of the dynein-dynactin cargo activating adaptors are the presence of a long N-terminal dimerizing coiled-coil, a binding site for the LIC subunit of dynein, which can be either a hook domain or a CC1-box, and a binding site for the dynactin pointed-end complex, termed spindly motif [73,87,88].

Since NuMA is a long coiled-coil containing protein, consists of a globular CH-like domain potentially at the binding interface with dynein, and a spindly-like motif potentially at the binding interface with dynactin (figure 1.6b), we speculated that NuMA could behave like a dynein-dynactin cargo activating adaptor.

Therefore, we decided to investigate whether NuMA interacts directly with the LIC subunit of dynein. LIC proteins exist in two closely related isoforms (LIC1 and LIC2, figure 2.3a) and, as described in paragraph 1.3.1, comprise an N-terminal GTPase-like domain binding to dynein HC, and an unstructured C-terminal region containing a conserved helix that associates with cargo adaptors [89]. Interestingly, in vertebrate cells the dynein subpopulation containing the LIC2 isoform was found to be implicated in the establishment of proper mitotic spindle orientation and to work in spindle assembly by focusing MT minus ends together with NuMA [134]. Based on this evidence, we set out to study the interaction between NuMA and both dynein LIC isoforms. To this aim, Francesca Rizzelli performed a glutathione S-transferase (GST) pulldown assay with bacterially purified GST-LIC1 and GST-LIC2, full-length or N-terminally truncated, immobilized on Glutathione Sepharose (GSH) beads, and His-tagged NuMA$^{1-705}$ in solution, purified to homogeneity by affinity and ion-exchange chromatography. All tested LIC1 and LIC2 constructs interacted with NuMA$^{1-705}$, with full-length LIC proteins (LIC1$^{1-523}$ and LIC2$^{1-492}$) displaying higher affinity than the

C-terminal portions (LIC1$^{390-523}$ and LIC2$^{379-492}$). Surprisingly, *in vitro* LIC1 showed slightly higher affinity for NuMA compared to LIC2 (figure 2.3b-c).

Therefore, we concluded that the N-terminal region of NuMA interacts directly with the LIC subunits of dynein, without discriminating between the two isoforms and without preference for LIC2.

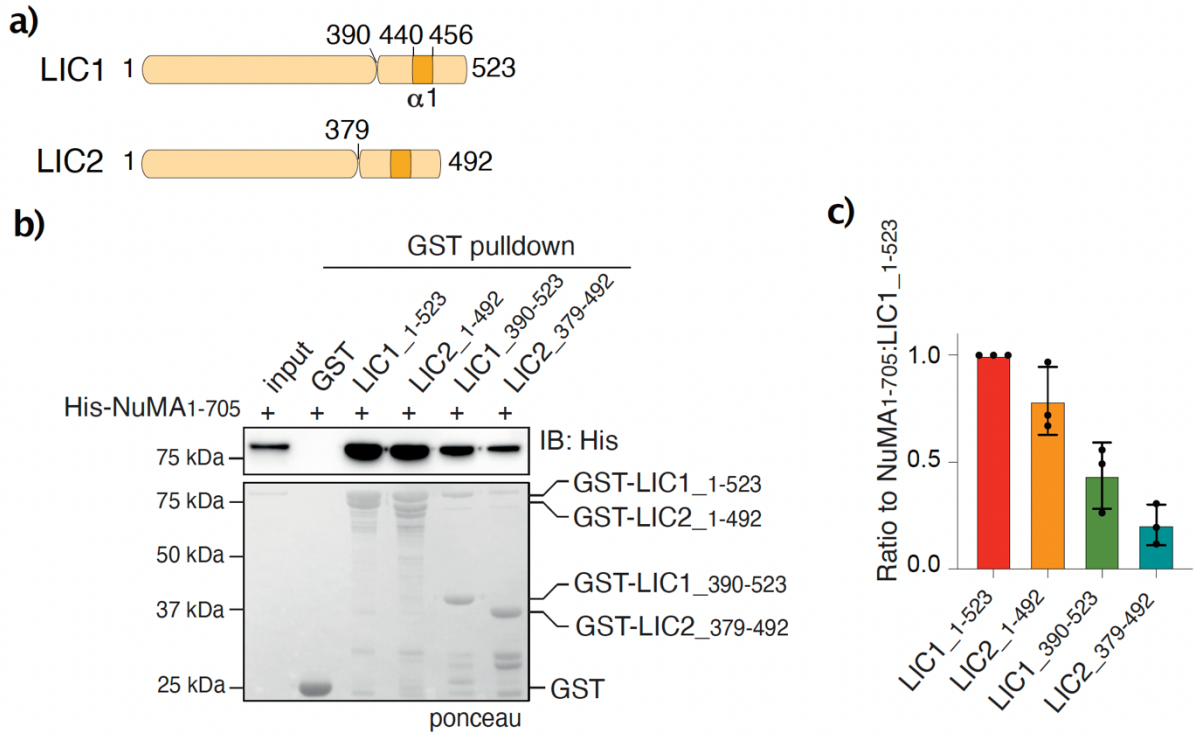

Figure 2.3 – NuMA$^{1-705}$ interacts with dynein LIC isoforms

a) *Schematic representation of human dynein LIC1 and LIC2 domain structure, with the C-terminal helix α1 highlighted in gold.* ***b)*** *GST pulldown experiment with 0.8 µM of GST-tagged full-length or C-terminal portions of LIC1 and LIC2 bound to glutathione resin, and 7 µM of His-tagged NuMA$^{1-705}$ in solution. Proteins retained on beads were analysed by immunoblotting using anti-His antibody, and 150 ng of His-NuMA$^{1-705}$ was used as input. GST proteins used in the experiment were visualized by ponceau staining.* ***c)*** *Ratio of bound NuMA$^{1-705}$ band intensity to NuMA$^{1-705}$/LIC1$^{1-523}$ signal. Mean and SD are shown for three independent experiments.*

2.4 NuMA$^{1-153}$ folds into a hook domain like Hook3$^{1-160}$

To start exploring the interface between NuMA and dynein LIC on the side of NuMA, we set out to determine the crystallographic structure of the NuMA globular head. To this aim, to obtain a crystallization quality sample, the monodisperse and monomeric NuMA$^{1-153}$ construct (figure 2.2d) was bacterially purified by AC and IEC, and then further polished on a Superdex-200 16/600 size-exclusion column equilibrated in 10 mM Tris (pH 6.8), 0.1 M NaCl, 5% glycerol, and 1 mM DTT (figure 2.2b). Peak fractions were analysed by SDS-

PAGE and fractions containing pure protein were pooled and concentrated to 33 mg/ml (2 mM).

Initial crystallization screenings were conducted in 200 nl vapor diffusion sitting-drops using commercially available kits and a mosquito Crystal nano dispenser (TTP Labtech) in MRC-2 well plates. At the two NuMA$^{1-153}$ concentrations tested (33 and 16.5 mg/ml), 100 nl of protein solution were mixed with an equal volume of reservoir solution and drops were equilibrated at 4 °C and 20 °C. Crystals appeared after two days, with a spherulite shape, in drops set at 16.5 mg/ml and equilibrated at 4 °C, with a reservoir containing 30% PEG-4000, 0.2 M $MgCl_2$, and 0.1 M Tris-HCl (pH 8.5), from the Crystal Screen 1 and 2 (Hampton Research) (figure 2.4a). This condition was selected for manual optimization and reproduced in 2 µl vapor diffusion hanging-drops in 24-well VDX plates. 1 µl of protein solution was mixed with an equal volume of reservoir solution and drops were equilibrated at 4 °C. The manual grid screening yielded better crystals, though not single, appearing overnight, with fast nucleation and growth kinetics (figure 2.4b).

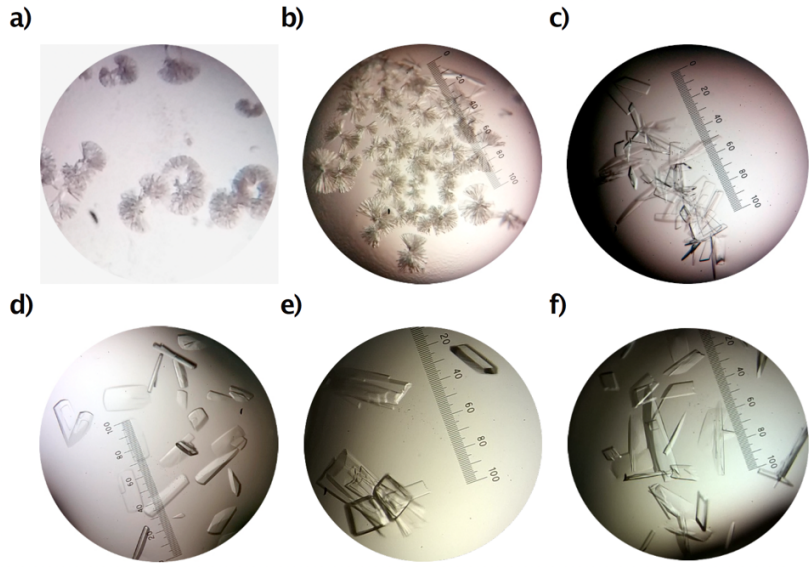

Figure 2.4 – NuMA$^{1-153}$ crystals

a) *Initial crystals obtained by sitting-drop vapor diffusion in 30% PEG-4000, 0.2 M $MgCl_2$, 0.1 M Tris-HCl (pH 8.5).* ***b)*** *Optimized crystals grown by hanging-drop vapor diffusion in 28% PEG-4000, 0.2 M $MgCl_2$, 0.1 M Bis-Tris-Propane (pH 8.5).* ***c)*** *Crystals optimized by streak seeding and by the addition of 4 mM TCEP with respect to the condition in panel b).* ***d-f)*** *Crystals grown in 0.1 M Bis-Tris-Propane (pH 8.5), 27% PEG-4000, 0.2 M $MgCl_2$, 4 mM TCEP, with the addition of 20% of 0.1 M Phenol, 0.1 M NaBr, or 1.0 M Glycine, respectively. Scale bar, 100 mm.*

To decouple crystal growth from nucleation, we employed streak seeding, a technique that consists in the introduction of preformed micronuclei into a low supersaturated condition,

where slow growth is optimal for the formation of diffracting crystals but spontaneous nucleation is unlikely. Practically, a seed stock solution is produced by crushing a crystal formed in a supersaturated solution with a metal bead. Then the seeds are introduced into a pre-equilibrated drop by streaking a thin whisker previously swept into the seed stock solution. The new crystals are often observed to grow along the direction of the streak containing the nuclei. To optimize crystals of $NuMA^{1-153}$, streak seeding was performed after four hours of equilibration, using fresh crystals as source of seeds. Seeding improved crystallization, slowing down crystal growth and generating single large crystals. $NuMA^{1-153}$ crystals were further improved by the addition of the reducing agent TCEP to the protein solution (figure 2.4c).

Diffraction-quality crystals were obtained as shown in figure 2.4d-f. The best diffracting crystals grew in crystallization drops consisting of a 1:1 (v/v) mixture of protein solution and well solution of 27% PEG-4000, 0.2 M $MgCl_2$, 0.1 M Bis-Tris Propane (pH 8.5), 4 mM TCEP, with 20% of the additive 0.1 M NaBr (figure 2.4e). $NuMA^{1-153}$ crystals were cryoprotected by stepwise addition of glycerol directly to the crystallization drops to a final concentration of 15% prior to flash-cooling in liquid N_2. X-ray diffraction data were collected to 1.54 Å resolution at the PXIII beamline X06DA of the Swiss Light Source (SLS, Villigen) (table 2.1).

The crystallographic work performed to solve and refine the structure of $NuMA^{1-153}$ was carried out by Manuel Carminati and Sebastiano Pasqualato and is described in the materials and methods section (paragraph 5.4). Briefly, the $NuMA^{1-153}$ structure was solved using experimental single-wavelength anomalous diffraction (SAD) phases derived from Seleno-methionine (Se-Met) containing crystals, which were grown similarly to the native ones. Crystals belonged to the orthorhombic space group $P2_12_12_1$, with unit-cell parameters consistent with four copies of the protein per asymmetric unit. The final crystallographic model was refined with an R_{free} of 21.5% and an R_{work} of 17.0%, with good stereochemistry, and covers all the 153 residues of the construct (table 2.1).

	Native	Derivative – SAD (SeMet)
Data Collection		
	PXIII – SLS	PXIII–SLS
Wavelength (Å)	1.000	0.979
Space group	$P2_12_12_1$	$P2_12_12_1$
Cell dimensions		
a, b, c (Å)	45.73,112.85,135.81	43.65,116.57,130.26
α,β,γ (°)	90.0, 90.0, 90.0	90.0, 90.0, 90.0
Resolution range (Å)	67.90–1.54 (1.57–1.54)	58.28–2.75 (2.84–2.75)
R_{sym} or R_{merge}	3.6 (139)	21.3 (256)
R_{meas}	3.9 (151)	21.5 (270)
$CC_{1/2}$	1.00 (0.54)	1.00 (0.71)
I/σI	22.9 (1.3)	22.1 (1.5)
Completeness (%)	100 (100)	100 (100)
Observed reflections	685,672	914,857
Unique reflections	104,874	18,013
Multiplicity	6.5 (6.3)	50.8 (27.1)
Refinement		
Resolution (Å)		67.90–1.54
R_{work}/R_{free}		17.0/21.5
Average B factors		
Proteins		39.26
Ions		33.74
Solvent		46.49
Root–mean–square deviations		
Bond lengths (Å)		0.02
Bond angles (°)		1.81
Ramachandran values (%)		
Favored		99.5
Allowed		0.5
Outliers		0.0

Table 2.1 – Data collection and refinement statistics table

By superposing the crystal structure of $NuMA^{1-153}$ to that of the hook domain of Hook3 in the same orientation, we found that $NuMA^{1-153}$ folds into a hook domain (figure 2.5a-b). The hook domain of Hook3 displays the canonical 7-helix CH-like fold, plus an additional helix at the C-terminus, termed helix α8, that divides into two short helices (α8a and α8b, figure 2.5c). These last helices create a V-shaped hydrophobic cleft for binding to a conserved LIC1 C-terminal helix (α1) [89]. In figure 2.5c are highlighted the two highly conserved hydrophobic phenylalanine residues (Phe447 and Phe448) in the middle of the LIC1 helix that are part of the binding interface with Hook3.

Two topological features distinguish the hook domain of NuMA from the analogous domain found in the Hook-family of dynein activating adaptors. The first lies in NuMA residues 111–117 (figure 2.6a), corresponding to helix α8a of Hook3, that adopt an extended flexible conformation rather than being helical (termed α7-α8 loop, figure 2.5b). The second sit in

the presence of an extra helix α9 that packs against helix α8 and inserts residues Leu147, Phe150, and Leu151 into a hydrophobic cavity contributed by helices α7 and α1, in this way stabilizing the core of the fold (figure 2.5d). More specifically, the hydrophobic pocket formed by helices α1, α7, α8 and α9 comprise residues Leu11 of α1, Met100 of α7, Ile130 and Phe133 of α8, and Leu147, Phe150, and Leu151 of α9. An electrostatic interaction is also formed between Asp146 of helix α9 and His137 of helix α8 to further stabilize the hook domain of NuMA (figure 2.5d).

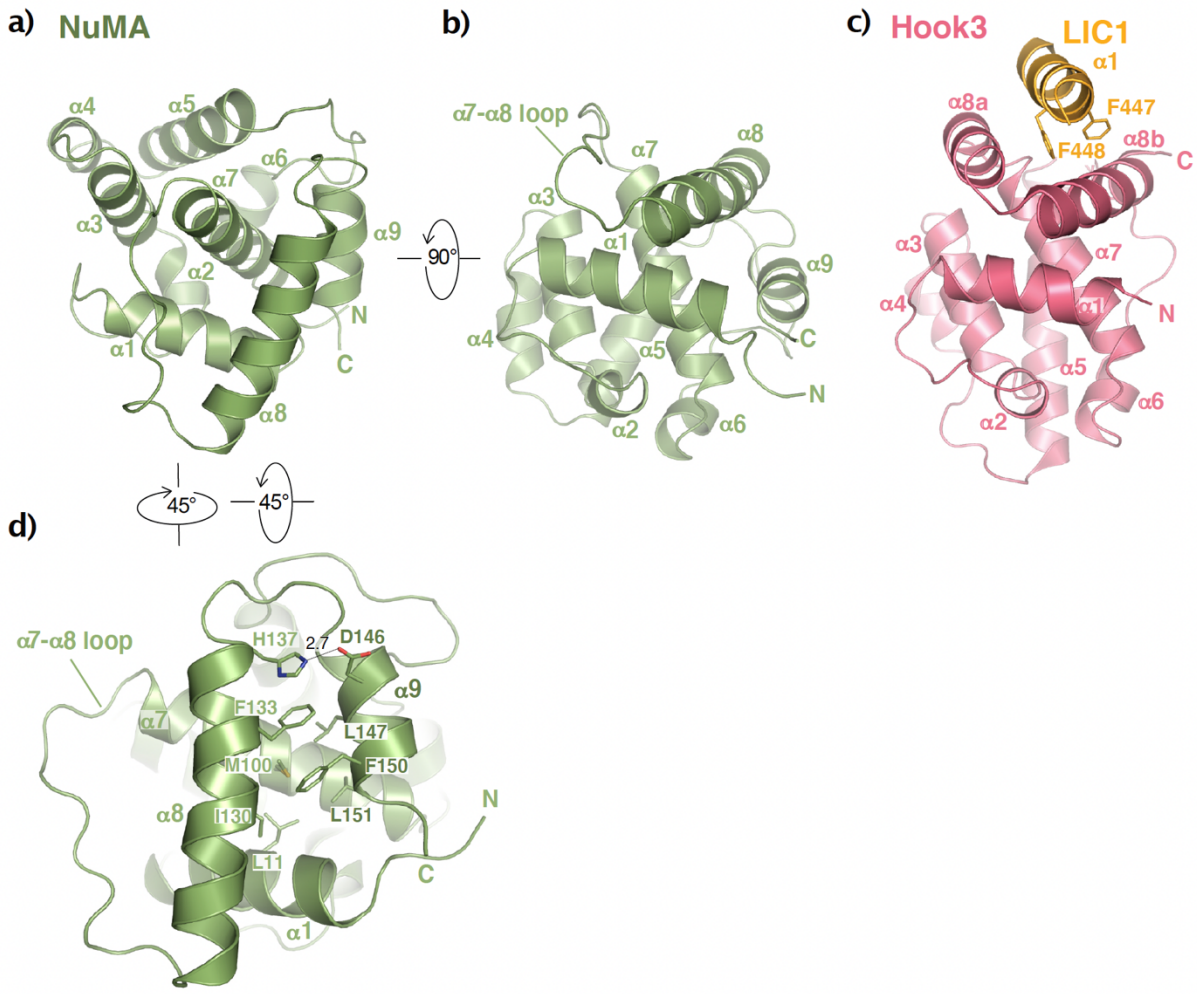

Figure 2.5 – NuMA$^{1-153}$ folds as a hook domain

a-b) *Cartoon representation of the crystal structure of NuMA$^{1-153}$ at the two orthogonal views (PDB ID: 6QJA).* ***c)*** *Cartoon representation of the crystal structure of the hook domain of Hook3 in complex with LIC1-α1 (PDB ID: 6B9H). Pink, Hook3; gold, LIC1. Hook3 is shown in the same orientation as NuMA in panel b). The side chains of Phe447 and Phe448 of LIC1-α1 are shown as balls-and-sticks.* ***d)*** *Cartoon representation of the crystal structure of NuMA$^{1-153}$ rotated of 45° in xy with respect to NuMA in panel a), in order to display the residues involved in CH-fold stabilizing interactions. In balls-and-sticks are shown the side chains of the hydrophobic residues of helix α9 (Leu147, Phe150 and Leu151) that contact Leu11 of helix α1, Met100 of helix α7, and Ile130 and*

Phe133 of helix α8. A hydrogen bond is formed between Asp146 of helix α9 and His137 of helix α8. α9 residues are in dark green.

We conclude that the domain structure of NuMA N-terminus ($NuMA^{1-705}$) is fully consistent with that of known dynein-dynactin activating adaptors, being organized into an initial monomeric hook domain ($NuMA^{1-153}$) followed by a dimeric coiled-coil, and interacting with dynein LIC.

We next asked whether the NuMA hook domain is the LIC-BD, as in the case of the hook domain of Hook-family proteins.

2.5 The hook domain of NuMA binds dynein LIC1 and LIC2 directly

The hook domain, a globular portion located N-terminal to the coiled-coil, is one of the motifs that Hook-family cargo adaptors use to interact with dynein LIC. Structural studies on Hook proteins revealed that the helix α1 of LIC1 fits into a hydrophobic cavity of the hook domain organized by the Hook3 helices α8a and α8b, in which the conserved residues Met140, Gln147, and Ile154 of Hook3 contact Phe447 and Phe448 of LIC1 (figure 2.6a-b) [87,89].

Hook3 residues required for LIC1 binding are conserved in NuMA, as shown in figure 2.6a. In the hook domain of NuMA, residues corresponding to helix α8α of Hook3 assume a flexible conformation, resulting in a less-structured hydrophobic pocket (figure 2.6c). To assess whether the hook domain of NuMA can nonetheless recognize helix α1 of LIC1, we moved to the biochemical characterization of the binding interface, and I generated His-tagged purified $NuMA^{1-705}$ mutants in the region encompassing the α7-α8 loop and helix α8 (figure 2.6g), testing their ability to bind GST-tagged LIC1 full length (Fl) by GST-pulldown experiments. The pulldown assays, conducted by Francesca Rizzelli, revealed that alanine substitutions of $Gln124^{NuMA}$ and $Leu131^{NuMA}$, corresponding to the Gln147 and Ile154 residues of Hook3, abrogated binding to LIC1, as well as alanine replacement of $Arg114^{NuMA}$ and $Leu135^{NuMA}$, whereas the mutations Trp116Ala and Tyr121Ala did not affect $NuMA^{1-705}$ binding to LIC1 (figure 2.6d-e). The same experiment was performed with the LIC2 isoform, and the result was the same (figure 2.6f).

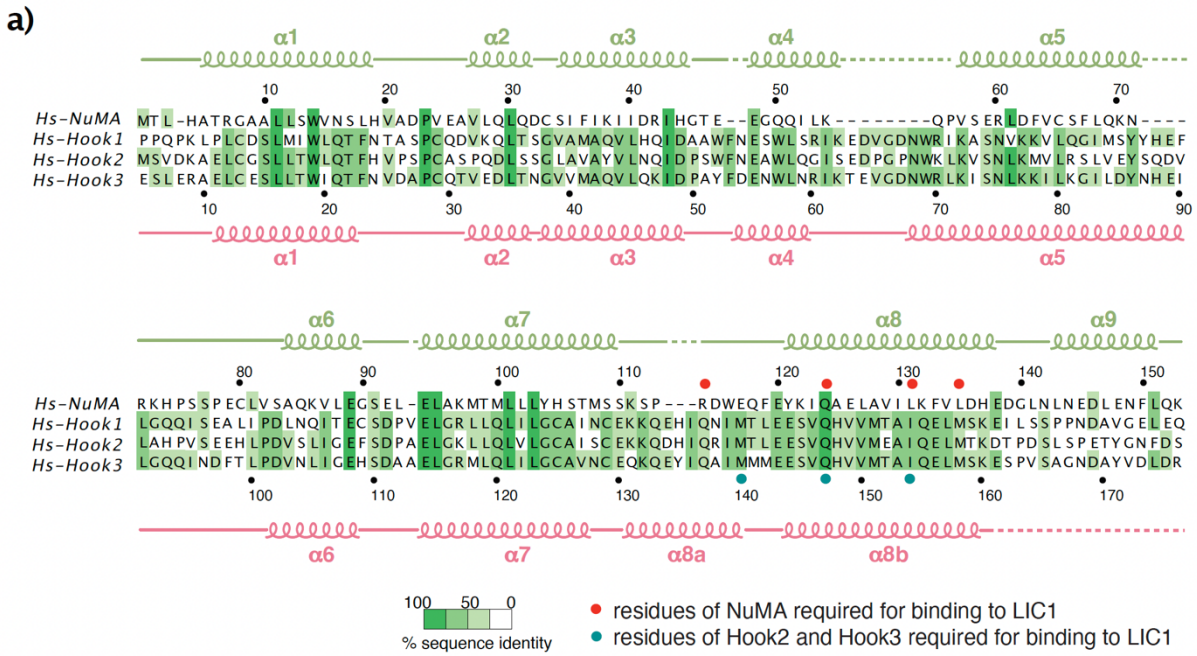
a)
α1 α2 α3 α4 α5
Hs-NuMA
Hs-Hook1
Hs-Hook2
Hs-Hook3
α6 α7 α8 α9
α8a α8b
100 50 0
% sequence identity
residues of NuMA required for binding to LIC1
residues of Hook2 and Hook3 required for binding to LIC1

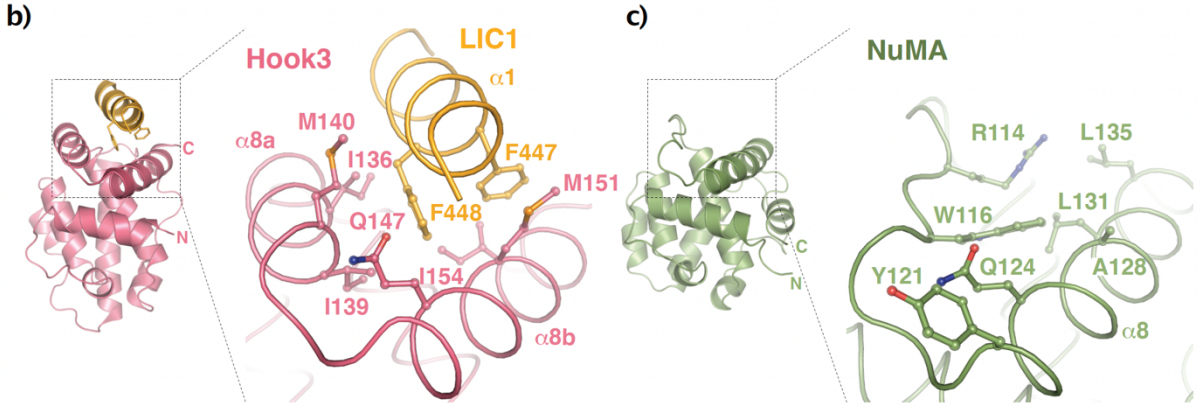
b)
Hook3
LIC1
α1
α8a
M140
I136
F447
M151
Q147
F448
I154
I139
α8b
c)
NuMA
R114
L135
W116
L131
Y121
Q124
A128
α8

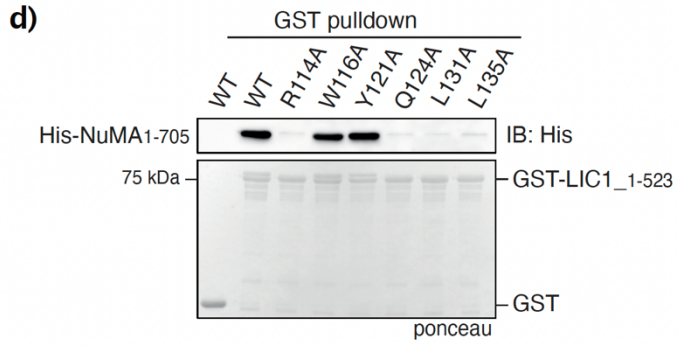
d)
GST pulldown
WT
R114A
W116A
Y121A
Q124A
L131A
L135A
His-NuMA1-705
IB: His
75 kDa
GST-LIC1_1-523
GST
ponceau

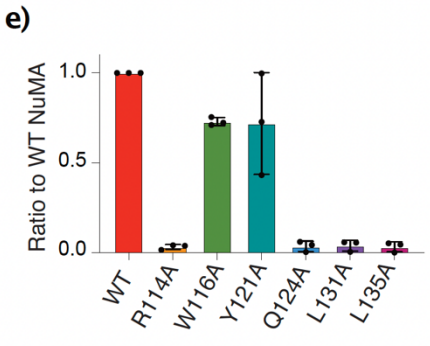
e)
Ratio to WT NuMA
1.0
0.5
0.0
WT
R114A
W116A
Y121A
Q124A
L131A
L135A

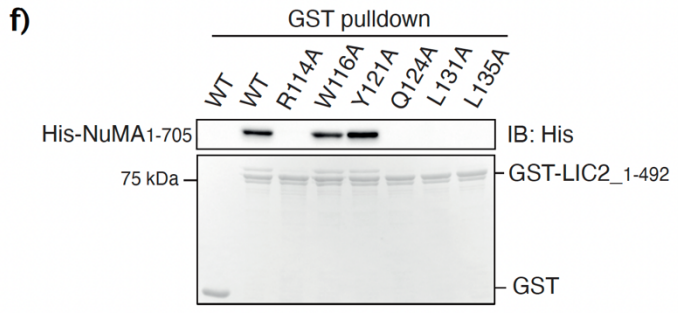
f)
GST pulldown
WT
R114A
W116A
Y121A
Q124A
L131A
L135A
His-NuMA1-705
IB: His
75 kDa
GST-LIC2_1-492
GST

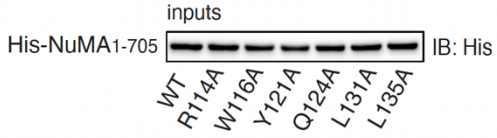
g)
inputs
His-NuMA1-705
IB: His
WT
R114A
W116A
Y121A
Q124A
L131A
L135A

Figure 2.6 – The hook domain of NuMA binds dynein LIC1 and LIC2 directly

a) *Sequence alignment of the hook domain of human NuMA, Hook1, Hook2, and Hook3, with secondary structure elements based on the crystallographic structures of NuMA and Hook3. Residues are coloured by percentage of sequence identity according to the alignment of different orthologs of NuMA, Hook1, Hook2, and Hook3. Red and green circles indicate residues of NuMA, Hook2, and Hook3 required for LIC1 binding.* ***b)*** *Close-up view of the Hook3/LIC1-α1 complex, with balls-and-sticks representation of the residues at the binding interface.* ***c)*** *Close-up view of the α7-α8 loop and helix α8 of NuMA in the same orientation as Hook3 in b), with balls-and-sticks representation of the residues at the putative binding interface, mutated in the pulldown experiments of panel d) and f).* ***d)*** *Pulldown assay with 0.8 μM of GST-LIC1$^{1-523}$ on glutathione resin, and 7 μM of His-NuMA$^{1-705}$ in solution, either wild-type (WT) or carrying the indicated mutations. Proteins retained on beads were visualized by immunoblotting using anti-His antibody, and GST proteins on beads by ponceau staining.* ***e)*** *Ratio of NuMA mutants band intensity to WT NuMA signal. Mean and SD are shown for three independent experiments.* ***f)*** *Pulldown assay with 0.8 μM of GST-LIC2$^{1-492}$ on glutathione resin, and 7 μM of His-NuMA$^{1-705}$ in solution, either WT or carrying the indicated mutations. Proteins retained on beads were visualized by immunoblotting using anti-His antibody, and GST proteins on beads by ponceau staining.* ***g)*** *Input proteins were analysed by immunoblotting using anti-His-antibody.*

2.5.1 The hook domain of NuMA cannot fully recapitulate the interaction with dynein LIC1 and LIC2

The evidence that mutations in the hook domain impair the interaction of NuMA$^{1-705}$ with LIC1 and LIC2 dynein subunits prompted us to test whether the hook domain alone could recapitulate the interaction with LIC1 and LIC2 C-terminal regions in solution.

Thus, I purified to homogeneity the NuMA$^{1-153}$ fragment, and the His-LIC1$^{390-523}$ and His-LIC2$^{379-492}$ constructs, as described in the materials and methods section (paragraph 5.2). In order to check the interaction between NuMA$^{1-153}$ and His-LIC1$^{390-523}$, I conducted an analytical SEC experiment. SEC analysis monitors the formation of protein complexes based on differences in their elution profile as compared to the proteins in isolation, meaning that we expect that protein complexes elute earlier than proteins in isolation. Purified NuMA$^{1-153}$ and His-LIC1$^{390-523}$ were loaded on a Superdex-75 Increase 10/300 column at millimolar concentrations in a 1:1 molar ratio. NuMA$^{1-153}$ and His-LIC1$^{390-523}$ elute from the SEC column in two separate peaks, as confirmed by the Coomassie-stained SDS-PAGE analysis of the eluted fractions (figure 2.7a, light blue line). The first peak is consistent with the elution profile of His-LIC1$^{390-523}$ in isolation (figure 2.7a, yellow line), while the second peak with the individual run of NuMA$^{1-153}$ (figure 2.7a, green line). The same result was obtained by loading on the SEC column 1.0 mM of NuMA$^{1-153}$ and 0.5 mM of His-LIC2^{379-}

[492] after 1 hour of incubation (figure 2.7b). Of note, only a small fraction of NuMA$^{1-153}$ enters a complex with the C-terminal portion of both LIC1 and LIC2 (figure 2.7a-b).
Therefore, we speculated that the coiled-coil region of NuMA is required for full binding to LIC or that LIC PTMs are a key regulator of NuMA binding [135].

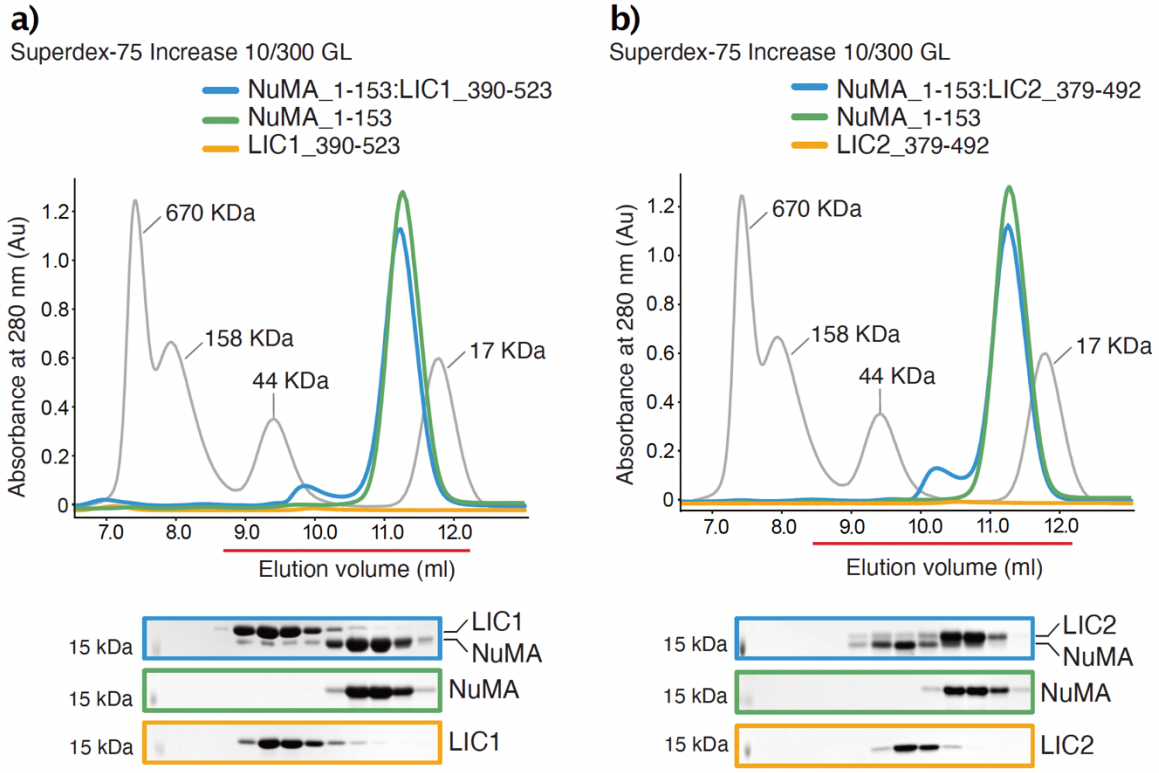

Figure 2.7 – The binding affinity of NuMA for LIC chains is low

a-b) *SEC elution profiles and Coomassie-stained SDS-PAGE analyses of NuMA$^{1-153}$ (1.0 mM) incubated with His-LIC1$^{390-523}$ (1.0 mM) or with His-LIC2$^{379-492}$ (0.5 mM) showing that in solution only a small portion of NuMA$^{1-153}$ forms a complex with the C-terminal domain of LIC1 or LIC2, while most of the sample elutes at the same volumes as the protein in isolation injected on the same column. The run of globular M_w markers is shown in grey. The presence of the proteins in the elution was monitored by absorbance at 280 nm and subsequently checked by SDS-PAGE of the peak fractions corresponding to the horizontal red bar. LIC1$^{390-523}$ and LIC2$^{379-492}$ are not visible by absorbance at 280 nm, as there are no aromatic residues nor cysteine residues in the constructs. For this reason, the concentration of the final samples was determined by BSA titration on Coomassie-stained SDS-PAGE gels.*

2.6 A CC1-box-like motif in the coiled-coil region of NuMA (NuMA$^{365-376}$) contributes to the NuMA-LIC interaction

As explained in the introduction (paragraph 1.3.1.1), the binding sites for dynein LIC characterized so far can be either a hook domain, shared by Hook-family proteins, or a

conserved N-terminal coiled-coil motif named CC1-box (consensus sequence: (D/E)xxxAAxxGxx(L/V)), where x denotes any amino acid, figure 1.11g), shared by the dynein activating adaptors BICD2, BICDR1 and SPDL1 (figure 1.11a), or pairs of EF hands [73].

Since the hook domain of NuMA cannot fully recapitulate the NuMA interaction with LIC1 and LIC2, we reasoned that NuMA$^{1\text{-}705}$ could harbour additional LIC-binding motifs. Sequence analysis excluded the existence of EF hands in the N-terminal portion of NuMA but highlighted the presence of a conserved motif encompassing residues 365-376 in the coiled-coil region (figure 2.8a). Intriguingly, this motif aligns with the CC1-box of known dynein-dynactin activating adaptors, although it does not entirely conform to the (D/E)xxxAAxxGxx(L/V) consensus sequence as the alanine couple A368-A369^{NuMA} is out of frame of one residue and the glycine residue is entirely missing (figure 2.8a).

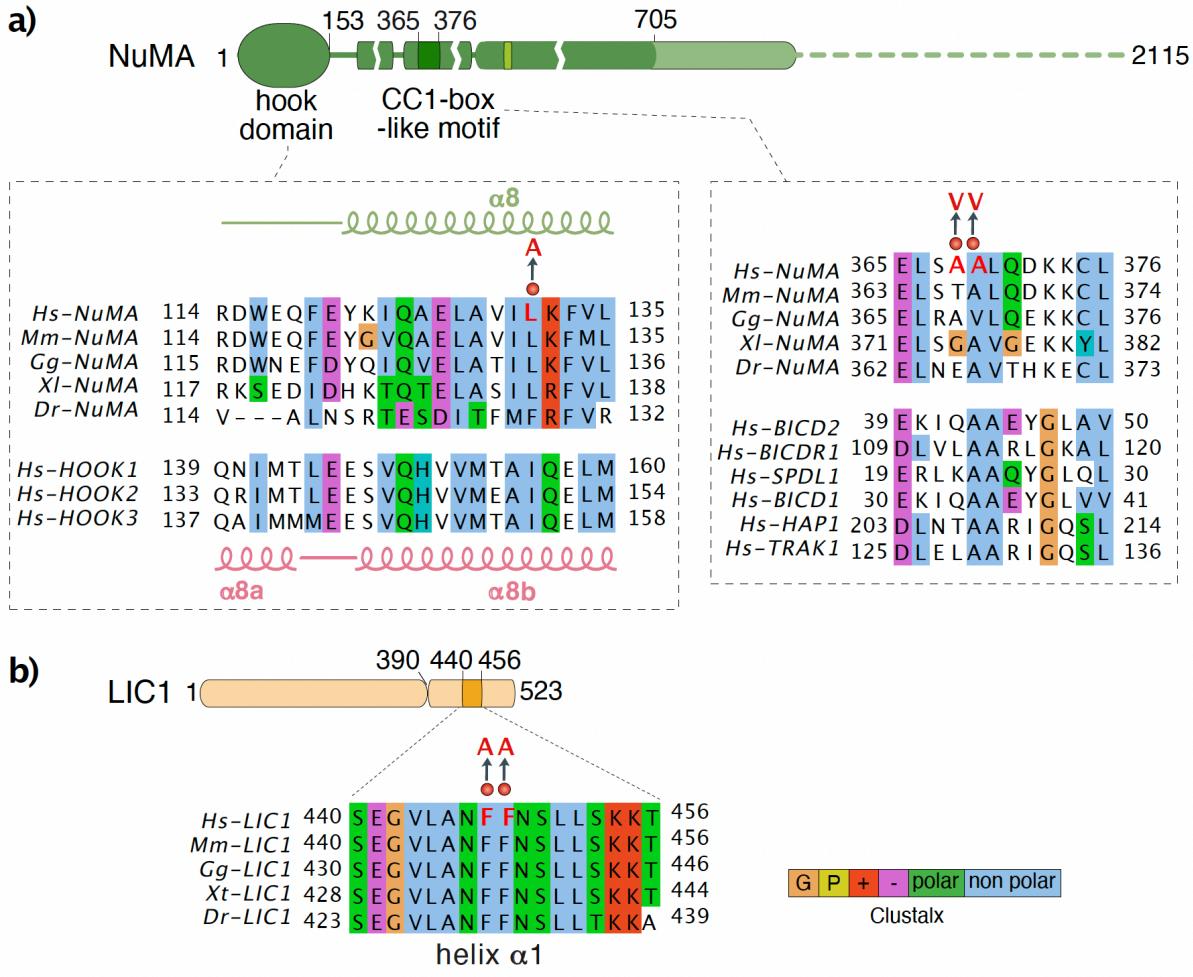

Figure 2.8 – Multiple sequence alignment of the hook domain and the CC1-box-like motif of NuMA and of the LIC1-α1

a) *Close-up views of a portion of the hook domain of NuMA sequence aligned with Hook-family proteins and of the CC1-box like motif of NuMA sequence aligned with CC1-box containing dynein*

adaptors. The sequence alignments were performed as described in the materials and methods section (paragraph 5.7). ***b)*** *LIC1-α1 sequences from Homo sapiens (Uniprot entry Q9Y6G9), Mus musculus (Uniprot entry Q8R1Q8), Gallus gallus (Uniprot entry Q90828), Xenopus tropicalis (NCBI entry NP_001072301.1), and Danio rerio (NCBI entry NP_001095898.1) were aligned with CLUSTALΩ and coloured in Jalview by Clustalx. Residues mutated in the GST pulldown experiments of figure 2.9 are highlighted in red.*

To understand whether this conserved NuMA motif is implicated in LIC recognition, we analysed the interaction properties of the NuMA$^{1-705}$ mutant where the alanine couple was mutated into valines (A368V/A369V). This mutation is commonly used to address the specificity of the CC1-boxes of dynein adaptors for LIC proteins [88]. GST pulldown experiments were performed testing the ability of NuMA$^{1-705}$ WT or mutated to interact with GST-LIC1$^{1-523}$ bound to GSH beads. As shown in figure 2.9a and in the quantification of panel b, NuMA$^{1-705}$-A368V-A369V displayed only residual binding to LIC1, confirming that this region of the NuMA coiled-coil is part of the NuMA-LIC interface.
Given the sequence similarity of this NuMA stretch encompassing residues 365-376 to that of the CC1-box, we called this newly identified LIC-BD of NuMA *CC1-box-like motif*.

2.7 Both the hook domain and the CC1-box-like motif contact LIC1-α1

Activating effectors structurally and functionally unrelated such as Hook proteins and CC1-box containing proteins have been shown to contact the same surface on the C-terminal half of LIC chains centred on helix α1, which, as we can see in the sequence alignment of figure 2.8b, is highly conserved between species [89]. To test whether also NuMA engages in hydrophobic interactions mediated by the LIC-α1 helix, we mutated Phe447 and Phe448 of LIC1 into alanine residues and tested the binding of the mutated protein to NuMA$^{1-705}$ WT, mutated only in the hook domain or mutated only in the CC1-box-like motif (L131A^{NuMA} or A369V/A369V^{NuMA}, figure 2.8a). GST pulldown experiments showed that GST-LIC1-F447A-F448A is totally impaired in NuMA binding, indicating that both the hook domain and the coiled-coil NuMA regions contact LIC1-α1 (figure 2.9c-e).
We conclude that NuMA contains two different LIC-BDs, the hook domain and the CC1-box-like motif, that share the same binding interface described for dynein activating adaptors, which is organized on the C-terminal helix α1 of LIC1.

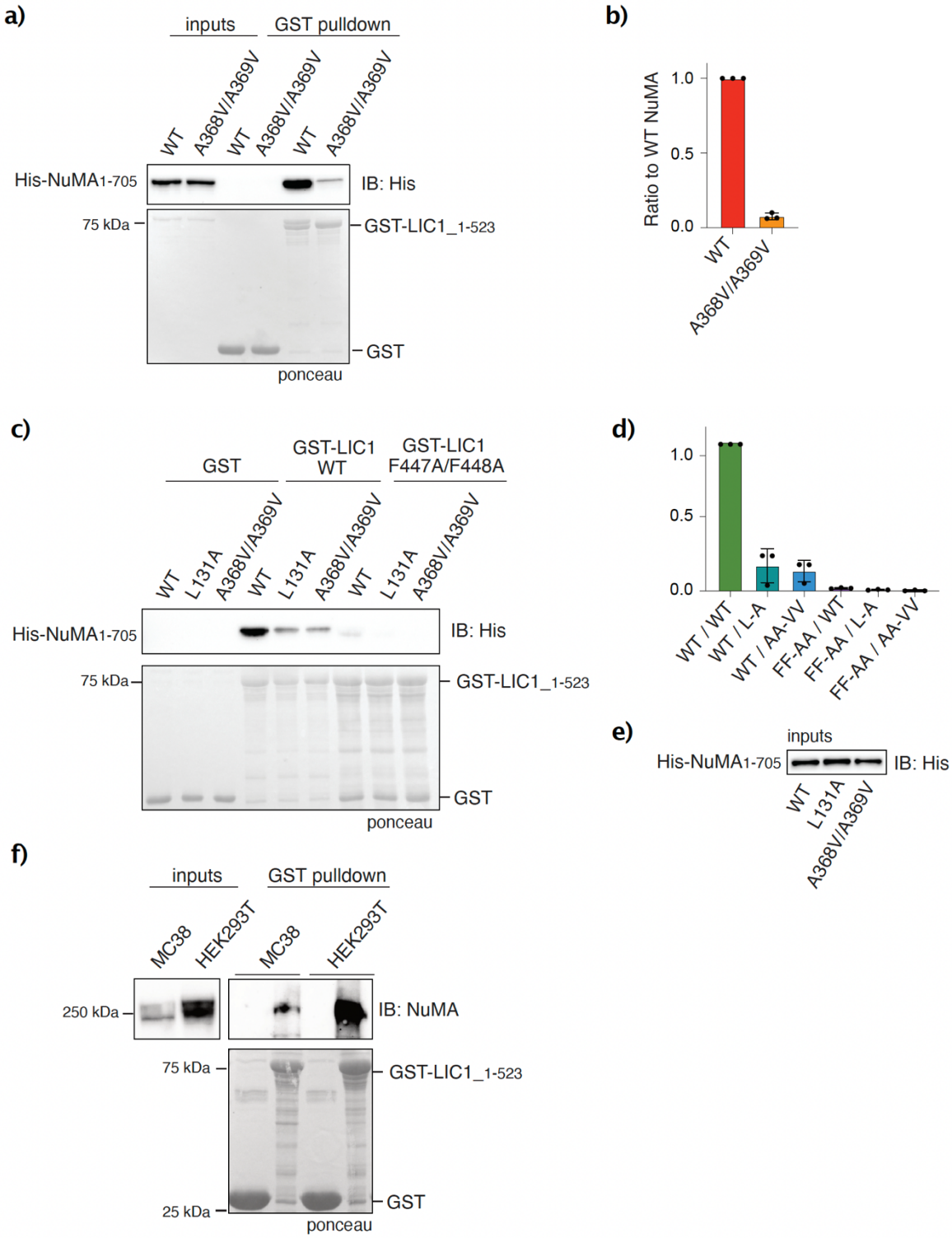

Figure 2.9 – NuMA N-terminus contains two LIC1-α1 binding interfaces

a) *Pulldown assay performed with 0.8 µM of GST-LIC1$^{1-523}$ on GSH beads and 7 µM of purified His-NuMA$^{1-705}$ WT or carrying the A368V-A369V^{NuMA} mutation in solution. Proteins retained on beads and input proteins were analysed by immunoblotting using anti-His antibody. GST proteins used in the experiment were visualized by ponceau staining.* ***b)*** *Ratio of band intensity to the WT NuMA$^{1-705}$ signal. Mean and SD are shown for three independent experiments.* ***c)*** *Pulldown assay with 0.8 µM of GST-LIC1$^{1-523}$ WT or carrying the F447A-F448A mutation on beads, and 7 µM of His-NuMA$^{1-705}$ WT, mutated in the hook domain (L131A), or mutated in the CC1-box-like motif (A368V/A369V) in*

solution. Proteins bound to beads were visualized by immunoblotting using anti-His antibody. GST proteins on beads were monitored by ponceau staining. ***d)*** *Ratio of band intensity to the signal of binding between WT NuMA$^{1-705}$ and WT LIC1$^{1-523}$ (WT/WT). Mean and SD are shown for three independent experiments.* ***e)*** *Equal amounts of prey proteins of the pulldown of panel c) were analysed by immunoblotting.* ***f)*** *2 μM of GST-LIC1 full-length bound to GSH resin was incubated with 1 mg of MC38 or HEK293T mitotic lysates at 10 mg/ml and 5 mg/ml concentration, respectively. Murine and human endogenous NuMA retained on beads were analysed by immunoblotting using anti-NuMA antibody. The blot on the left shows the NuMA expression levels in the two cell lines. 20 μg of MC38 and HEK293T mitotic cell lysates were loaded.*

As shown in the sequence alignment of figure 2.8a, the CC1-box-like motif of NuMA does not fully conform to the CC1-box consensus sequence, as the human NuMA alanine couple A368-A369 is out of frame of one residue, and the glycine residue (highly conserved in CC1-box containing adaptors) is entirely missing. Of note, comparing different NuMA orthologues sequences, we found that the alanine couple present in human NuMA is not conserved between species, as in the case of mouse NuMA sequence where the first alanine is substituted by a threonine residue (figure 2.8a).

Therefore, to address the conservation of this newly identified CC1-box-like motif, we performed a GST pulldown experiment with purified GST-LIC1$^{1-523}$ immobilized on GSH beads, testing its ability to pulldown endogenous NuMA from human HEK293T cells or murine colon adenocarcinoma (MC38) cells synchronized in mitosis by 16h nocodazole treatment. In more detail, 1 mg of extracts at 10 mg/ml for MC38 cells, and 5 mg/ml for HEK293T cells, depending on the different NuMA expression level, were incubated with 2 μM of bait proteins (figure 2.9f). The experiment revealed that, despite the limited conservation of the CC1-box like motif, the NuMA-LIC1 interaction is preserved throughout species. This suggests that Ala368 in the human NuMA alanine couple could be not essential for the interaction, and that the Leu370 hydrophobic residue which, together with the Ala369 conserved NuMA residue perfectly aligns with the CC1-box alanine couple, could be part of the LIC-binding interface.

2.7.1 Both the hook domain and the CC1-box-like motif cannot fully recapitulate the interaction with dynein LIC

To quantify accurately the binding affinity, we decided to measure the strength of the binding between NuMA and LIC by ITC. ITC is a technique that allows the determination of the thermodynamic parameters of a binding reaction, including the dissociation constant (K_d), the enthalpy and entropy, and the binding stoichiometry. Specifically, this method is based

on the measurement of the heat exchange occurring during the formation of a complex, when protein molecules are titrated to saturation into a cell containing the ligand. The heat released or absorbed upon binding is then plotted as a function of time and fitted with a non-linear model, generating for a binary interaction a sigmoidal curve from which thermodynamic parameters can be extrapolated. I titrated 5 mM of LIC1 α1 peptide (residues 433-458) into 0.4 mM of purified NuMA$^{1-414}$ N-terminal construct, containing both the hook domain and the CC1-box-like motif. Unfortunately, no interaction was scored, and the stoichiometry of NuMA-LIC1 binding was not measurable (figure 2.10a).

Hence, we supposed that NuMA requires all residues 1-705 to interact with LIC1. Accordingly, I conducted an analytical SEC experiment to check the interaction between NuMA$^{1-705}$ and His-LIC1$^{390-523}$ in solution. Unfortunately, I could not test the binding of LIC1 C-terminus to millimolar amounts of NuMA$^{1-705}$ as this construct is prone to aggregation at high concentration. Purified NuMA$^{1-705}$ and His-LIC1$^{390-523}$ were loaded on a Superose-6 10/300 column at 0.27 mM and 1.0 mM concentrations respectively, and no substantial binding was detected (figure 2.10b). NuMA$^{1-705}$ and His-LIC1$^{390-523}$ elute from the SEC column in two distinct peaks, as confirmed by the Coomassie-stained SDS-PAGE analysis of the eluted fractions (figure 2.10b, light blue line). The first peak is consistent with the elution profile of NuMA$^{1-705}$ in isolation (figure 2.10b, green line), while the second peak with the individual run of His-LIC1$^{390-523}$ (figure 2.10b, yellow line).

We then hypothesized that the C-terminus of LIC1 is not sufficient to reconstitute the interaction. Therefore, I conducted an analytical SEC experiment to check the interaction between NuMA$^{1-705}$ and MBP-LIC1-His Fl. Being LIC1 Fl insoluble and easily degraded in solution, an N-terminal MBP-tag was added to increase the solubility of the protein and a C-terminal His-tag to discard the LIC1 degraded products at the C-terminus [89]. The NuMA$^{1-705}$ and MBP-LIC1-His purified proteins were loaded on a Superose-6 10/300 column at 0.15 mM and 0.2 mM concentrations and eluted from the SEC column in two separate peaks, as confirmed by SDS-PAGE analysis of the eluted fractions (figure 2.10c). Despite the very high concentrations, no interaction was scored between NuMA$^{1-705}$ and MBP-LIC1-His, supporting the hypothesis that the binding affinity is low and that in solution the complex dissociates easily.

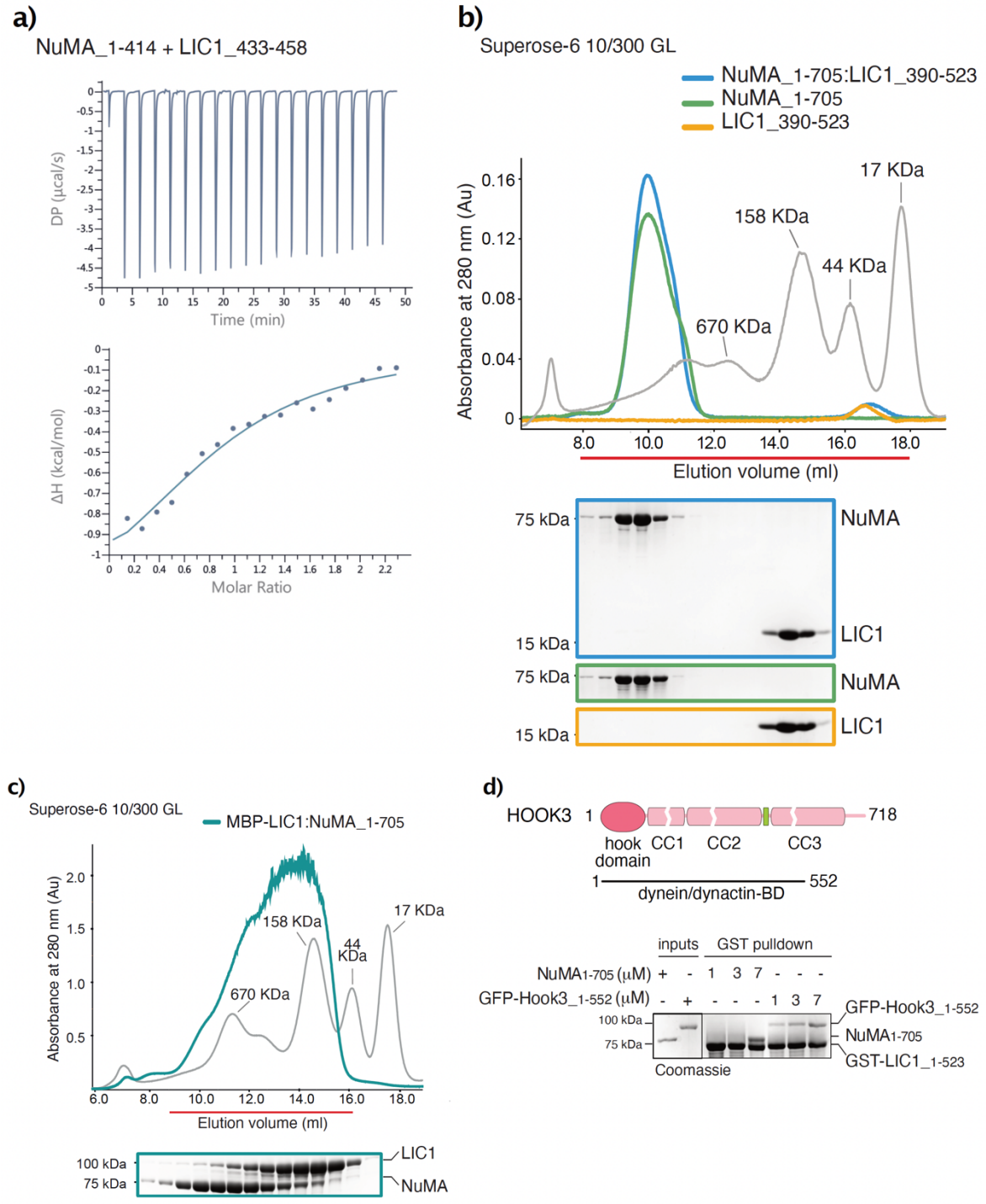

Figure 2.10 – NuMA-LIC1 interaction is not recapitulated in solution

a) *ITC isotherm in which 5 mM of LIC1-α1 peptide was injected in a cell containing 0.4 mM of NuMA$^{1-414}$.* ***b)*** *SEC elution profiles and Coomassie-stained SDS-PAGE analyses of NuMA$^{1-705}$ (0.27 mM) incubated with LIC1$^{390-523}$ (1.0 mM) showing that the two proteins do not form a complex in solution. Individual runs and SDS-PAGES are shown as reference.* ***c)*** *SEC elution profile and Coomassie-stained SDS-PAGE analysis of NuMA$^{1-705}$ (0.15 mM) incubated with MBP-LIC1$^{1-523}$-His (0.2 mM) showing that the two proteins do not form a complex in solution. The presence of the proteins in the elution was monitored by absorbance at 280 nm and subsequently checked by Coomassie-stained SDS-PAGE of the peak fractions corresponding to the horizontal red bar.*

Globular Mw markers are in grey. ***d)*** *Domain structure of human Hook3 and comparative analysis of NuMA$^{1-705}$ and Hook3$^{1-552}$ binding to LIC1. The pull-down experiment was performed with 0.8 μM of GST-LIC1 full-length on GSH beads, and 3-5-7 μM of His-NuMA$^{1-705}$ or GFP-Hook3$^{1-552}$ in solution. After washes, proteins retained on beads were separated by SDS-PAGE and visualized by Coomassie staining.*

Together these biophysical data suggest that the affinity of NuMA for LIC chains is substantially lower than the one measured between LIC1 and Hook3 (of about 12 μM) [89]. Comparative pull-down experiments conducted with GST-LIC1$^{1-523}$ adsorbed on GSH beads and increasing concentrations of purified NuMA$^{1-705}$ or Hook3$^{1-552}$ in solution confirmed that this is indeed the case (figure 2.10d).

In addition to the low binding affinity between NuMA and LIC, it is possible to envision other explanations to the lack of binding in solution: mitotic PTMs could be required for the interaction, the binding surface of dynein on NuMA could be more extended than the one beween NuMA and LIC, or NuMA binding to dynactin potentially through the spindly-like motif could have an important role in the formation of a stable complex.

Further structural and biochemical studies on the entire dynein-dynactin-NuMA assembly are needed to address the overall topology of the NuMA-dynein-dynactin complexes forming during mitosis to sustain mitotic spindle functions.

2.8 NuMA LIC-binding motifs are required for proper mitotic spindle assembly and orientation

NuMA, together with the dynein-dynactin complex, plays major roles in all mitotic spindle functions, including assembly and orientation, as explained in the introduction (paragraph 1.3). Consistent with these activities, in unpolarized HeLa cells during metaphase, NuMA and dynein-dynactin are distributed at the spindle poles and at the cortical regions facing the spindle poles (Figure 1.7a).

On this line, we set out to study the functional relevance of the NuMA-dynein LIC interaction in mitotic HeLa cells. To this aim, Chiara Gaddoni and Laura Pirovano in the lab generated mCherry-tagged NuMA truncation mutants devoid of the entire N-terminal dynein-dynactin binding portion (NuMA-Δ1-705) or of the individual LIC-BDs, the hook domain (NuMA-Δ1-153) or the CC1-box-like motif (NuMA-Δ154-705), or mutated only in the alanine couple of the CC1-box-like motif (NuMA-A368V/A369V) (figure 2.11a). These constructs were transfected in mitotic HeLa cells infected with a control short hairpin RNA (shRNA) or stably depleted of NuMA (shNuMA), and tested their ability to rescue spindle

defects observed in HeLa cells lacking endogenous NuMA (figure 2.11b, see paragraphs 5.5 and 5.5.1 in the materials and methods section for technical details).

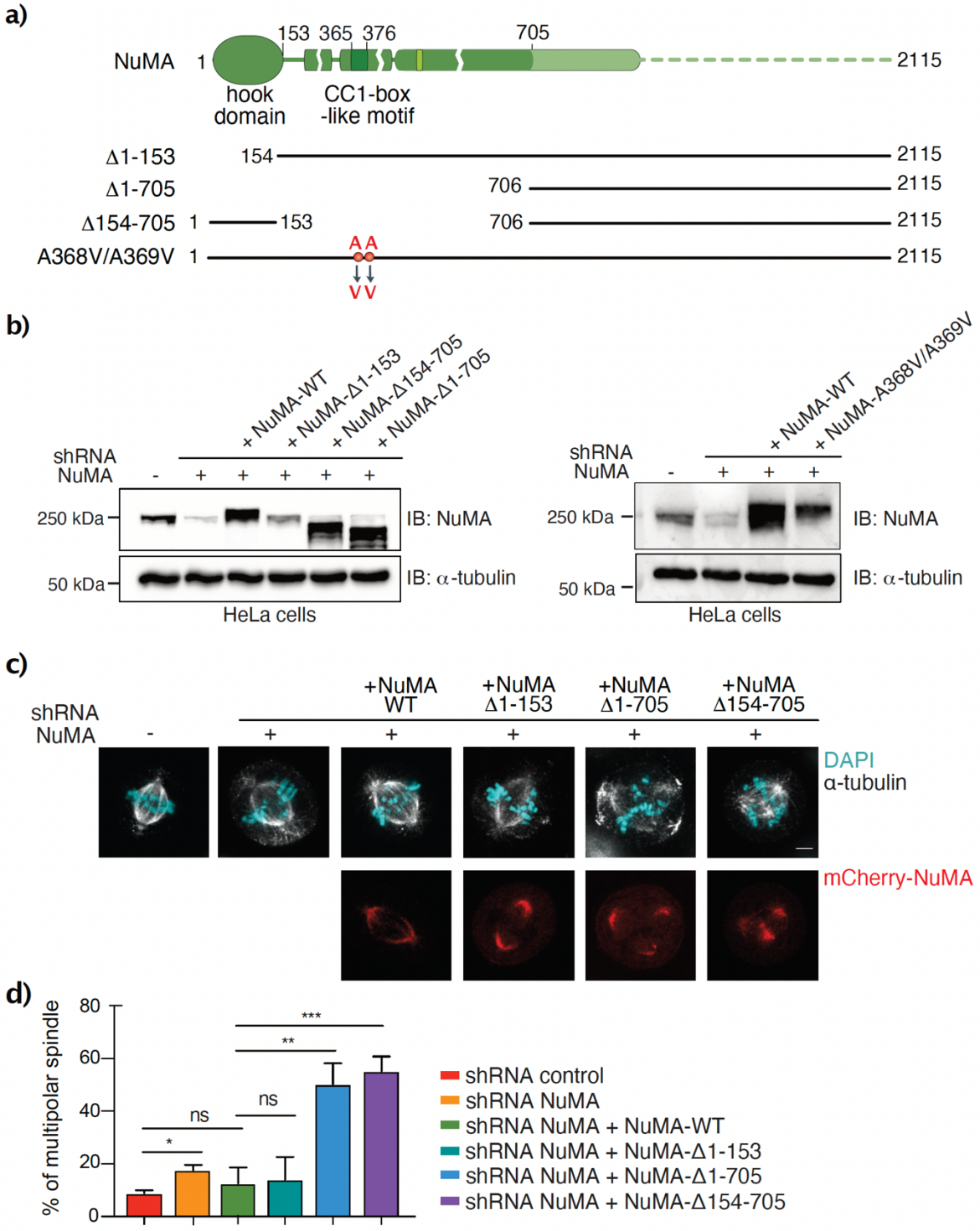

Figure 2.11 – Analysis of spindle multipolarity in HeLa cells expressing mCherry-NuMA mutants

a) *Schematic representation of the domain structure of human NuMA. Bold lines with numbers indicate protein constructs used in the bottom experiments and in figure 2.12.* ***b)*** *Immunoblot of mitotic lysates of HeLa cells infected with a control shRNA or stably depleted of endogenous NuMA and transfected with the mCherry-tagged rescue constructs NuMA-WT, NuMA-Δ1-153, NuMA-Δ1-*

705, NuMA-Δ154-705 and NuMA-A368V/A369V. α-tubulin was used as loading control. ***c)*** *Confocal sections of mitotic HeLa cells expressing a scrambled control shRNA, or stably depleted of endogenous NuMA and expressing mCherry-tagged NuMA-WT, NuMA-Δ1-153, NuMA-Δ1-705 or NuMA-Δ154-705. Cells were stained for α-tubulin (white) to visualize the spindle, and DAPI (cyan) to visualize the metaphase plate. The localization of the NuMA rescue constructs was monitored by mCherry fluorescence. Scale bar, 5 mm.* ***d)*** *Quantification of multipolar spindle of HeLa cells imaged in panel c. Mean ± SD are shown for 3 independent experiments, with n > 70. *** indicates p < 0.001; ** p < 0.01; ns, not significant, by Fisher's exact test.*

Depletion of NuMA causes abnormal spindles morphology, multipolar mitoses, and chromosome congression errors. Multipolar spindle defects are rescued upon expression of NuMA full-length and partly of NuMA-Δ1-153, whereas the NuMA-Δ1-705 and NuMA-Δ154-705 truncation mutants fail to restore bipolar spindles and display a strong dominant negative phenotype conceivably due to other NuMA functions (figure 2.11c-d). Of note, all truncation mutants were found to localize at the spindle poles as the WT protein, confirming that NuMA localizes to the poles in the absence of dynein (figure 2.11c). This is in line with the reported ability of NuMA to target dynein activity to MT minus-ends to cluster spindle MTs into poles, serving as a mitosis-specific minus-end cargo adaptor [59].

NuMA is also known to recruit the dynein-dynactin complex to the cell cortex to position the spindle [32,53]. In vertebrate systems, to study the molecular details of spindle orientation, *in vitro* cultured epithelial cells are used. One of the most frequently used *in vitro* model are HeLa cells cultured on a fibronectin substrate to assess integrin-mediated division orientation. This human cell line in WT condition orients the mitotic spindle parallel to the substratum [20]. Therefore, we next asked whether NuMA truncation mutants unable to interact with LIC can sustain spindle orientation in HeLa cells depleted of endogenous NuMA.

Major defects of spindle organization can result in spindle mispositioning. Hence, to address the spindle orientation functions of NuMA truncation mutants, Chiara Gaddoni and Laura Pirovano analysed only the subpopulation of HeLa cells with correct bipolar spindle assembly and properly congressed chromosomes. Measurements of the spindle axis angle of metaphase HeLa cells plated on fibronectin coated cover slides showed that cells lacking NuMA undergo misoriented divisions that are rescued by NuMA full-length but not by any of the truncation mutants (figure 2.12a-c), suggesting that in epithelial cells NuMA-LIC interaction is essential for spindle orientation. Notably, the point mutant NuMA-A368V/A369V restored spindle alignment to the substrate almost to the same extent of WT

NuMA, indicating that, in this kind of assay, the disruption of the CC1-box like motif is tolerated within the NuMA-dynein complex (figure 2.12a-c).

In conclusion, we suggest that NuMA binding to LIC is crucial for dynein mediated NuMA functions in mitotic spindle assembly and positioning. Further experiments are required to study the co-localization of NuMA and LIC in mitotic cells to better understand the functionality of the complex.

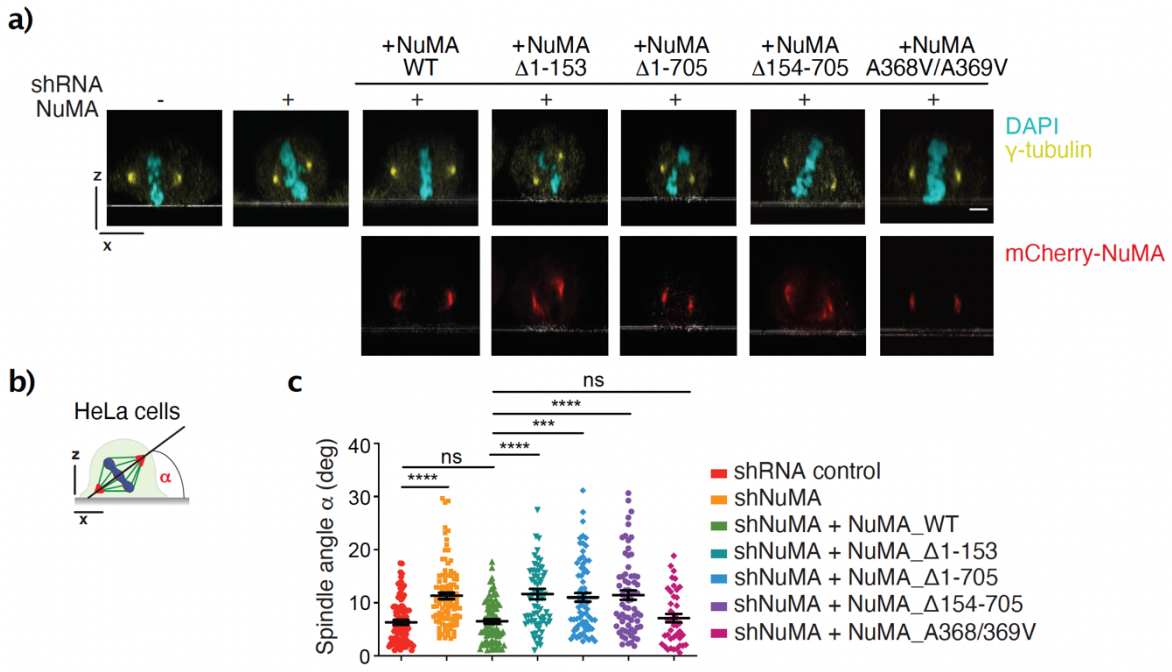

Figure 2.12 – LIC-binding motifs of NuMA are required for mitotic spindle orientation

a) *Confocal x-z sections of mitotic HeLa cells expressing a scrambled control shRNA, or stably depleted of endogenous NuMA and expressing mCherry-tagged NuMA-WT, NuMA-Δ1-153, NuMA-Δ1-705, NuMA-Δ154-705, or NuMA-A368V/A369V. Cells were stained with γ-tubulin (yellow) to visualize the spindle poles, and with DAPI (cyan) to show DNA. The white line represents the plane of the coverslip. The expression of the NuMA rescue constructs was monitored with the mCherry signal. Scale bar, 5 μm.* ***b)*** *Scheme showing that quantification of spindle orientation is performed by measuring the angle formed by a line passing through the spindle poles and the coverslip.* ***c)*** *Quantification of the spindle angle distribution of HeLa cells shown in panel c). Means ± SEM are shown for three independent experiments, with n=94 for control cells, n=102 for NuMA-shRNA expressing cells, n=88 for NuMA-depleted cells expressing NuMA-WT, n=70 for NuMA-depleted cells expressing NuMA-Δ1-153, n=75 for NuMA-depleted cells expressing NuMA-Δ1-705, n=68 for NuMA-depleted cells expressing NuMA-Δ154-705 and n=40 for NuMA-depleted cells expressing NuMA-A368V/A369V. The Kruskal-Wallis test was applied. **** indicates p < 0.0001; *** indicates p < 0.001; ns, not significant.*

3. RESULTS: molecular insights into the NuMA-53BP1 complex

The role of nuclear NuMA in the DDR is mainly focused on the regulation of the access of the protein 53BP1, a crucial component of DNA DSB signalling and repair in mammalian cells, to DNA repair compartments [2]. Based on this, the second part of my PhD project aimed at characterizing the biochemical binding interface between the proteins NuMA and 53BP1, which I found to interact not only in the nucleus in the absence of DNA damage, but also during mitosis when 53BP1 plays a prominent role in the centrosome surveillance pathway (paragraph 1.4.2.1).

3.1 NuMA associates with chromatin

As mentioned in the introduction (paragraph 1.4), NuMA accumulates in the nucleus during interphase and upon nuclear envelope reformation during telophase (figure 1.11). NuMA was defined for years as a nuclear matrix protein and demonstrated recently to interact with DNA *in vitro* and with chromatin in cells [63]. Molecular analyses on the role of NuMA in the cell nucleus are recent and a clear understanding of these NuMA functions requires further studies.

To confirm the localization of NuMA on chromatin during interphase, I performed a nuclear fractionation experiment in HEK293T cells. I divided the cytoplasmic and nuclear compartments, extracting the cytosol with a hypotonic buffer. The nucleus was then further divided in the soluble nucleosol and in the chromatin and insoluble nuclear matrix fraction, the first obtained in a buffer at high concentration of salt, and the second extracted in a buffer containing high concentration of urea.

In more detail, cells were harvested, washed, and divided in two pellets of the same volume. One pellet was resuspended in S300 extraction buffer (S300) containing 20 mM Tris-HCl (pH 8.0), 0.3 M NaCl, 10% glycerol, 0.2% NP40, 1 mM DTT and protease inhibitors. After 20 minutes of incubation, sonication, and centrifugation at 13,000 rpm, the supernatant, representing the total extract, was collected for western blot analysis (figure 3.1a). The second pellet was resuspended in nuclear prep buffer (NPB) containing 10 mM Tris-HCl (pH 8.0), 0.1 M NaCl, 2 mM $MgCl_2$, 0.3 M Sucrose, 0.2% NP40, 1 mM DTT and protease inhibitors, kept 5 minutes on ice and then centrifuged at 3,000 rpm to separate the cytosolic fraction. The remaining pellet was washed with NPB buffer and then resuspended in S300 buffer. After 20 minutes of incubation and centrifugation at 13,000 rpm, the supernatant was collected. This represents the nucleoplasmic fraction used in the GST-pulldown experiment of figure 3.5c. The pellet was washed with S300 buffer and then resuspended in urea extraction buffer consisting of 8 M Urea, 25 mM Tris-HCl (pH 6.8), 1 mM EDTA (pH 8),

10% glycerol. After sonication and centrifugation at 13,000 rpm, the chromatin and nuclear matrix fraction was extracted (figure 3.1b).

As shown in figure 3.1c, in HEK293T cycling cells NuMA was found to fractionate both in the nucleosol and in the chromatin and nuclear matrix fraction, as recently seen also by Rajeevan and colleagues in HeLa Kyoto cells [63].

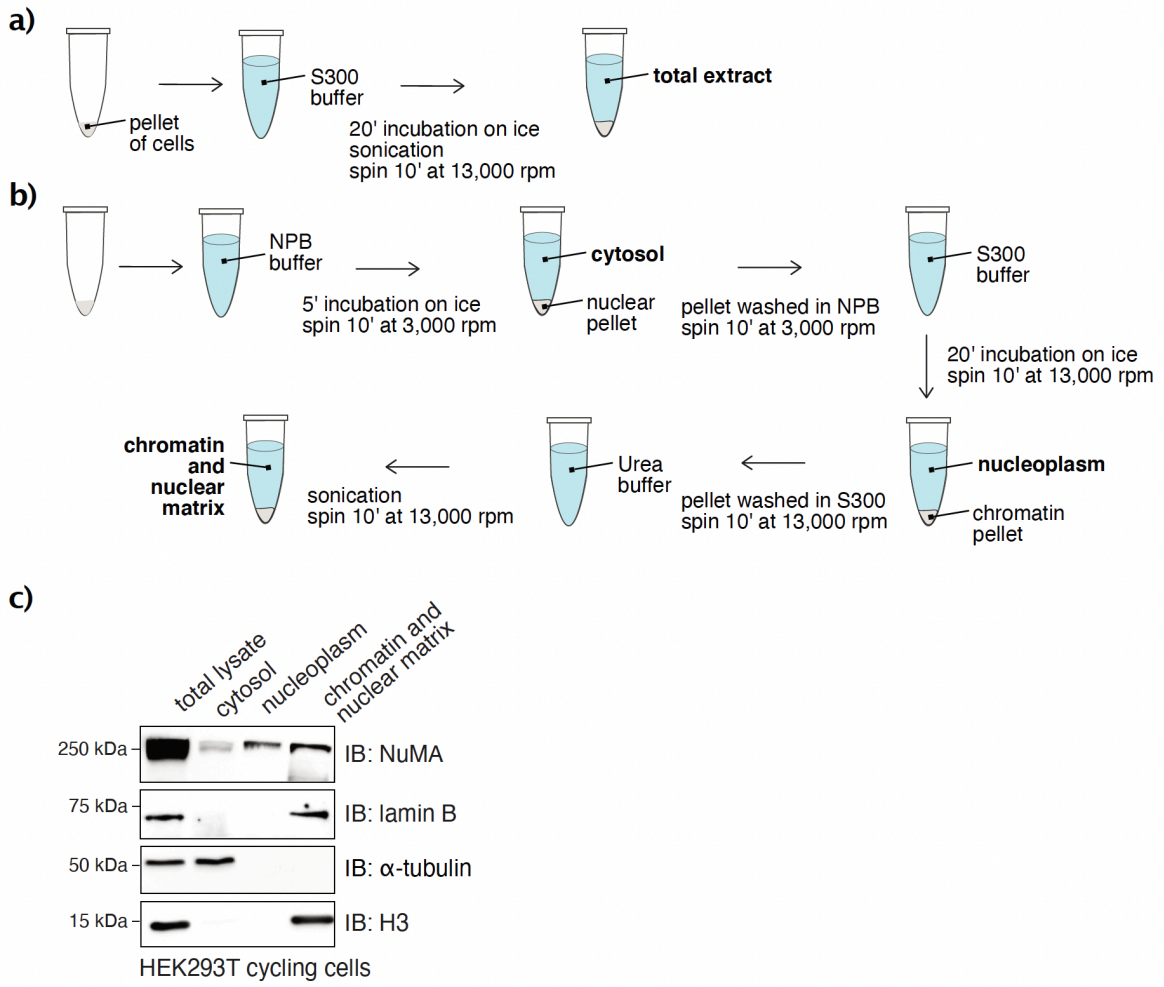

Figure 3.1 –NuMA fractionates with chromatin in the interphase nucleus

a) *Protocol for the extraction of total lysate as reference.* ***b)*** *Protocol for the extraction of the nucleoplasm, and chromatin and nuclear matrix fractions.* ***c)*** *Immunoblot analysis of protein extracts prepared from HEK293T cells, which were later fractionated into cytosol, nucleoplasm, and chromatin fractions. These fractions were probed for NuMA, α-tubulin, lamin B and H3. α-tubulin was used as cytoplasmic marker, lamin B as nuclear matrix marker, and histone H3 as chromatin marker. 40 μg of each fraction was loaded on the SDS-PAGE before immunoblotting.*

Rajeevan and colleagues [63] together with the Dumont laboratory [56] last year precisely mapped the DNA-BD of NuMA (residues 2058-2115, figure 1.6d). On this line we decided to perform co-IP experiments to study the binding of NuMA with histone proteins. To this

aim, I used an α-NuMA monoclonal antibody that I obtained using as epitope the purified NuMA construct encompassing residues 1-705 and I tested its ability to immunoprecipitate endogenous NuMA (figure 3.2c-d). Consequently, I performed a co-IP experiment with this α-NuMA antibody, and I evaluated the capability of NuMA to co-immunoprecipitate the histone protein H3. As shown in figure 3.2c and in the quantification of panel g, a strong interaction was scored between the two proteins.

Altogether these data suggest that a portion of NuMA freely diffuses in the nucleus and a pool is associated with chromatin. This is in line with FRAP experiments performed by Rajeevan and colleagues indicating that the half-time for the recovery ($t_{1/2}$) of GFP-NuMA is ∼13 s, a value similar to that of various transcription factors transiently associated with chromatin in interphase [63]. However, the molecular details and the functional role of NuMA association to chromatin are still largely unknown.

3.2 Molecular dissection of the NuMA-53BP1 interaction interface with functional implications

In addition to its role in chromatin organization, in the mammalian cell nucleus NuMA was found to play a role in regulating DSB repair by both HR and NHEJ pathways [104]. However, the regulatory mechanism of this process is still not known.

As explained in the introduction (paragraph 1.4.1), the protein NuMA was recently reported to colocalize and interact with the DDR protein 53BP1 and identified as a negative regulator of 53BP1 in the repair of DSBs, preventing the access of the repair factor to chromatin in the absence of DNA damage [2].

In this respect, NuMA may phenocopy the protein TIRR, a soluble factor binding to the tandem Tudor domain of 53BP1 and preventing 53BP1 interaction with H4K20me2 [119] (figure 1.12c). Like 53BP1-NuMA, the interaction between 53BP1 and TIRR has been reported to decrease in response to DNA damage, enabling 53BP1 binding to chromatin proximal to DSBs. Hence, being NuMA a component of the insoluble nuclear matrix fraction, NuMA and TIRR may act as distinct negative regulators of 53BP1 in the different compartments (soluble nucleoplasm and insoluble nuclear matrix) of a normal cell nucleus.

Another finding possibly connected to the role of the NuMA-53BP1 complex in DSB repair came from the laboratory of Mosammaparast, which found that the MT- and Aurora A-binding protein TPX2 interacts with 53BP1 by counteracting its DDR function during replication stress [132]. Because NuMA downregulates the 53BP1 DNA repair activity and was recently found by Polverino and colleagues to be part of the same complex with TPX2 at

mitotic spindle poles [133], we hypothesized that NuMA could work with TPX2 also in the interphase nucleus in the DDR regulation via 53BP1.

Based on these premises we decided to start testing whether endogenous NuMA interacts with 53BP1 and TPX2 in the nucleus of human HEK293T cells. To this aim I performed a fractionation experiment with a protocol suitable for the subsequent co-IP experiment, without separating the soluble and the insoluble nuclear fractions. After extracting the cytosol, the nuclear pellet was resuspended in a buffer containing 0.15 M NaCl, 0.5% NP40 and the Benzonase nuclease, this latter required for the digestion of DNA and the release of nuclear proteins strongly associated with DNA (figure 3.2a).

In more detail, cells were harvested, washed, and two volumes of hypotonic buffer, consisting of 10 mM Tris-HCl (pH 7.6), 1.5 mM $MgCl_2$, 10 mM KCl, 1 mM DTT, protease inhibitors and phosphatase inhibitors, were added, compared to the volume of the pellet. Cells were kept on ice for 10 minutes and then 10% triton was added (1/30 of the original pellet volume). After centrifugation at 11,000 rpm, the supernatant, representing the cytoplasmic fraction, was collected. Nuclear extraction buffer (NEB), containing 50 mM Tris-HCl (pH 7.6), 0.15 M NaCl, 0.5% NP40, 20% glycerol, 2 mM $MgCl_2$, 1 mM DTT, protease and phosphatase inhibitors, was added to the pellet (1/3 of the original volume) after washing with hypotonic buffer. Benzonase nuclease was added to the solution in a 1:100 ratio. After 1 hour of incubation on a rotating wheel and centrifugation at 13,000 rpm, the supernatant, representing the nuclear extract, was collected. Cytosolic and nuclear fractions were quantified by Bradford assay before immunoblotting (figure 3.2a-b).

The IP experiment was performed with this nuclear fraction, testing the capability of endogenous NuMA to immunoprecipitate 53BP1 and TPX2 under physiological conditions. The co-IP experiment was performed as detailed in the materials and methods section (paragraph 5.6.5): 10 μg of the α-NuMA antibody was incubated with 0.5 mg of nuclear lysate at 5 mg/ml of concentration. As shown in figure 3.2c and in the quantification of panels e and f, nuclear NuMA was found to bind efficiently to both 53BP1 and TPX2, suggesting that the three proteins could be stabilized in the same biological complex.

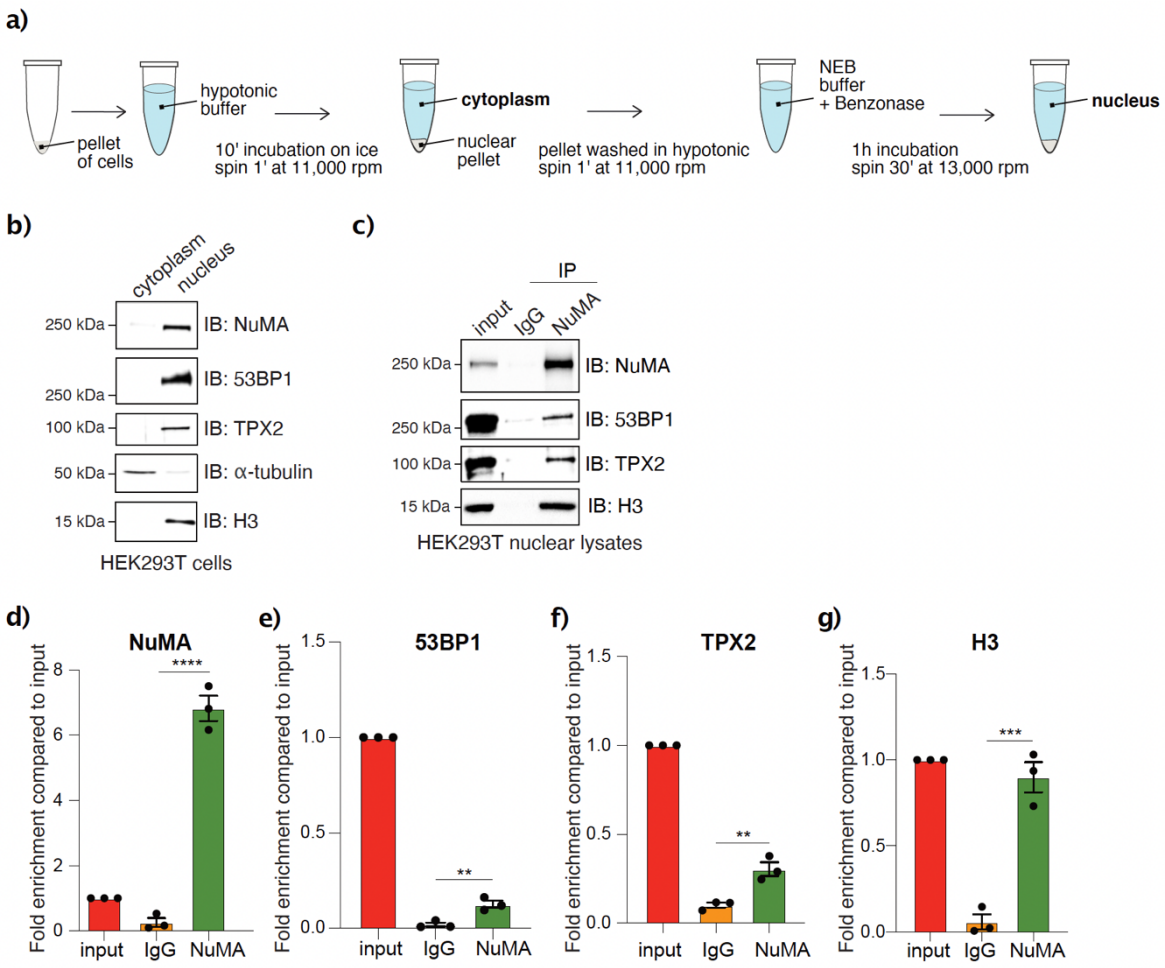

Figure 3.2 – Multiple binding partners of NuMA in the nucleus of human cells

a) *Protocol to obtain the nuclear fraction for the IP experiment.* ***b)*** *Immunoblot analysis of extracts prepared from HEK293T cells, which were fractionated into cytosolic and nuclear fractions. 30 μg of each fraction was loaded on the SDS-PAGE and probed for NuMA, 53BP1, TPX2, α-tubulin, and H3. α-tubulin, and H3 were used as cytoplasmic and nuclear markers.* ***c)*** *IP experiment with 0.5 mg of nuclear extracts and 10 μg of α-NuMA antibody to test the interaction of endogenous NuMA with the nuclear proteins 53BP1, TPX2, and H3. 20 μg of lysate was loaded as input. IgG were used as negative control for the IP.* ***d-g)*** *Quantification of NuMA-bound 53BP1, TPX2, and H3 levels normalized to input signals. Error bars represent SEM from three independent experiments. **** indicates $p < 0.0001$; by one way ANOVA Tukey's multiple comparisons test.*

3.2.1 NuMA-53BP1 binding is reduced upon doxorubicin treatment

We decided to test the modulation of the interaction between NuMA and 53BP1 in the nucleus of HEK293T cells treated for 12 hours with 200 nM of doxorubicin, which is a drug that damages DNA through intercalation or direct alkylation, causing the formation of DNA DSBs. In response to DNA damage, the protein KAP1 is highly phosphorylated by ATM at serine 824 and hence phopsho-KAP1 was used as marker of DNA damage induction (figure

3.3a-c). I performed co-IP experiments as in figure 3.2c and evaluated the interaction between NuMA and 53BP1 in the presence and absence of doxorubicin treatment. As shown in figure 3.3b and in the quantification of band intensities of panels d and e, upon doxorubicin treatment, the amount of 53BP1 immunoprecipitating with NuMA is much reduced with respect to the physiological one.

We conclude that, in response to doxorubicin induced DNA damage, the 53BP1-NuMA interaction is reduced.

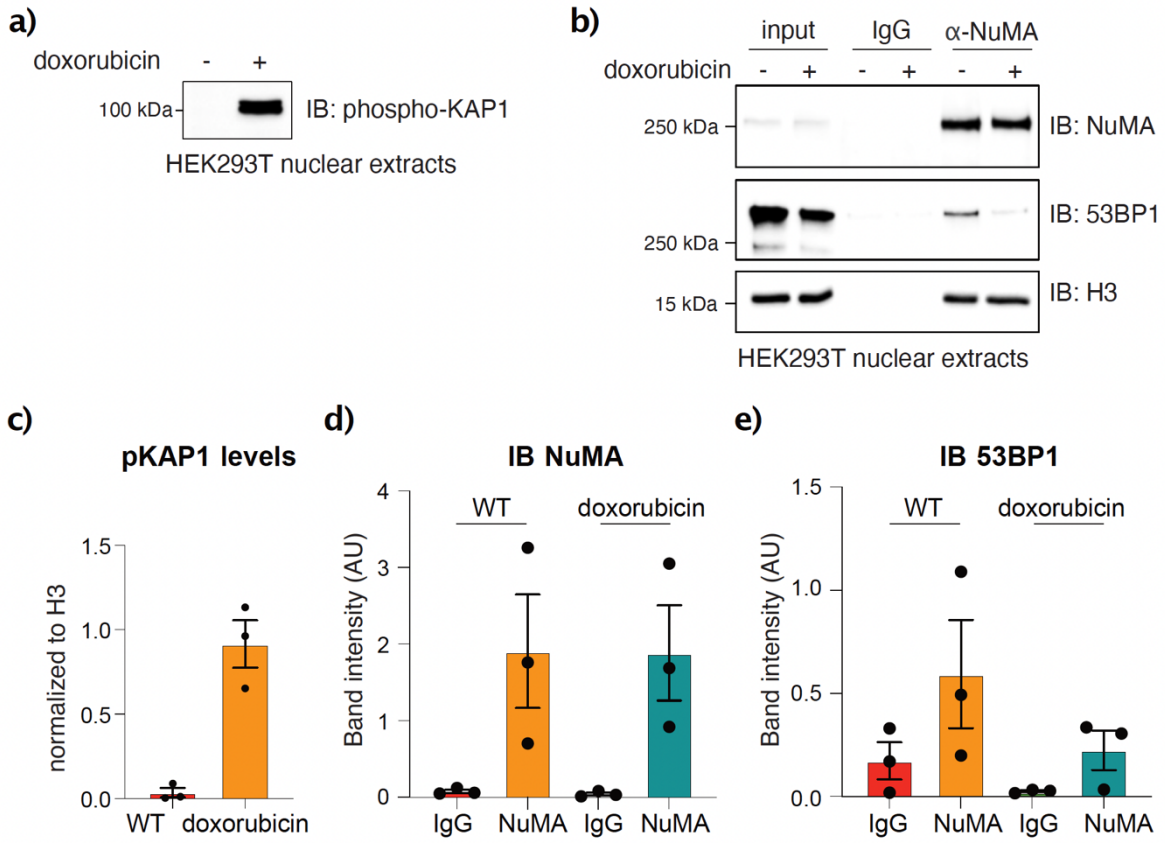

Figure 3.3 – Doxorubicin reduces NuMA-53BP1 binding

a) *30 μg of HEK293T nuclear lysates treated or not with doxorubicin were loaded on SDS-PAGE and the resulting blot was probed for phospho-KAP1, to assess the DNA damage induction.* ***b)*** *IP experiment with 10 μg of α-NuMA antibody to test the interaction of endogenous NuMA with 53BP1 in the nucleus of HEK293T cells (0.5 mg) with and without doxorubicin treatment (12h, 200 nM). IgG were used as negative control for the IP, and histone H3 was loaded as positive control for the co-IP. 15 μg of lysates was loaded as input.* ***c)*** *Quantification of pKAP1 levels normalized to that of H3. Error bars represent SEM from three independent experiments.* ***d-e)*** *Quantification of bound NuMA and 53BP1 band intensities as arbitrary units (AU). Error bars represent SEM from three independent experiments.*

3.2.2 NuMA-53BP1 interaction occurs also in mitosis

Besides being a nuclear protein, NuMA has been well-characterized for a long time for its multiple roles during mitosis in the regulation of spindle assembly and positioning. Consistent with these activities, mitotic NuMA accumulates at the spindle poles and at cortical regions facing the spindle poles during metaphase (figure 1.7a). In mitosis, 53BP1 was found to be a key effector of the mitotic surveillance pathway that upon centrosome loss or prolonged mitosis mediates p53 activation for cell-cycle arrest [121] (see paragraph 1.4.2.1). Once confirmed the interaction between NuMA and 53BP1 in the nucleus of human cells in WT condition (figure 3.2c), we then asked whether the binding occurs also in mitosis. To test this idea, I synchronized HEK293T cells in prometaphase by 16h nocodazole treatment and then performed a co-IP experiment using the α-NuMA antibody suitable for IP and immunoblotting 53BP1 to evaluate its retention on beads. The NuMA-53BP1 interaction was scored also under these conditions (figure 3.4).

This suggests that the NuMA-53BP1 complex seen in interphase in the absence of DNA damage, could be important also during mitosis, and possibly be involved in the mitotic surveillance pathway in which 53BP1 is known to be implicated. Notably, we also observed an interaction between endogenous NuMA and TPX2 during mitosis (figure 3.4), further validating the same experiment performed with transfected proteins [133].

This biochemical finding of the formation of a complex between NuMA, 53BP1 and TPX2 requires supplemental studies to understand its physiological role both in the nucleus in the absence of DNA damage and in mitosis.

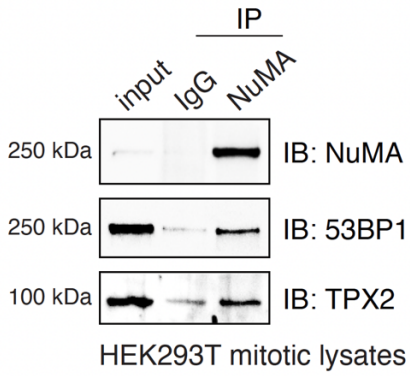

Figure 3.4 –NuMA-53BP1 binding is also mitotic

IP experiment with 10 μg of α-NuMA antibody to study the binding of endogenous NuMA with 53BP1 and TPX2 in HEK293T cells (0.5 mg) synchronized in mitosis by 16h nocodazole treatment. 15 μg of lysate was loaded as input.

3.2.3 53BP1$^{1285\text{-}1972}$ is the NuMA-binding region

To test whether the NuMA-53BP1 interaction is direct and map the NuMA-53BP1 interacting domain on the side of 53BP1, I generated four GST-tagged 53BP1 constructs encompassing the full-length protein (residues 1-595, 596-1219, 596-1284, and 1285-1972) (figure 3.5a), and performed GST-pulldown experiments with mitotic and nuclear HeLa cell lysates.

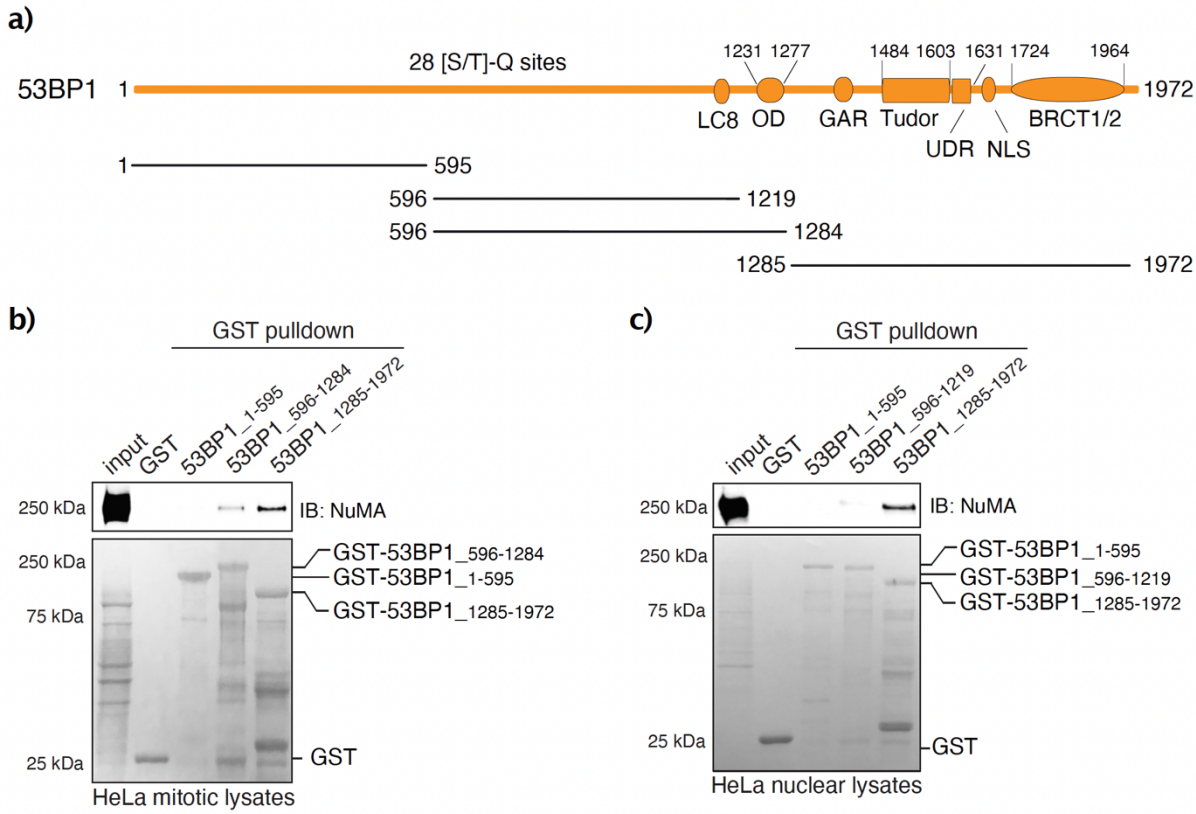

Figure 3.5 – 53BP1$^{1285\text{-}1972}$ is the NuMA binding site both in mitosis and in the nucleus

a) *Schematic representation of human 53BP1-1 domain structure. Bold lines with numbers indicate protein subdomains used in the pulldowns of panels below.* ***b-c)*** *GST pulldown experiments with 2 µM of GST-tagged 53BP1 constructs bound to GSH beads, and 1 mg of HeLa mitotic/nuclear cell lysates. GST was included in the experiments as negative control. Species retained on beads were analysed by immunoblotting for NuMA, and 20 µg/5 µg of lysates were loaded as input. The amount of GST and of each GST-53BP1 construct was assessed by ponceau staining.*

In figure 3.5b is shown the pulldown performed using bacterially purified GST-tagged 53BP1$^{1\text{-}595}$, 53BP1$^{596\text{-}1284}$, and 53BP1$^{1285\text{-}1972}$ as bait, and testing their ability to pulldown endogenous NuMA from HeLa cells blocked in mitosis by nocodazole treatment. 1 mg of mitotic extract was incubated with 2 µM of baits and the 53BP1 C-terminal construct spanning residues 1285-1972 was the fragment interacting with NuMA best. A slight

interaction occurred as well with the fragment of 53BP1 spanning residues 596-1284 that contains the OD, suggesting that the OD could create aspecific binding on beads.

The same experiment was performed with HeLa nuclear extracts and the result was similar (figure 3.5c). In this case, instead of the 53BP1 fragment encompassing residues 596-1284, I used a construct lacking the OD (residues 596-1219). The fact that we didn't score any binding between NuMA and 53BP1$^{596-1219}$ further corroborates the idea that the OD renders the 53BP1 construct aggregate on beads. Of note, the nuclear extract used in this experiment was the nucleoplasmic fraction obtained as for figure 3.1 in 0.3 M NaCl, and diluted to physiological salt concentrations (0.1 M NaCl) before conducting the pulldown.

The 53BP1 domain found to interact with NuMA (residues 1285-1972) comprises the tandem Tudor and UDR motifs, which are required for the recruitment of 53BP1 to damaged chromatin, and the BRCT domains that during mitosis interact with USP28 and p53 (see paragraphs 1.4.2 and 1.4.2.1). Thus, a possible explanation for the negative effect exerted by NuMA on 53BP1 could be that NuMA masks the 53BP1 binding to the DSB-specific histone code in the absence of DNA damage, and during mitosis binds to the BRCT domains, thus having a potential role in the mitotic surveillance pathway.

Further mapping experiments are required to better understand the minimal NuMA binding region on 53BP1, whether the interaction is direct, and thus the functional role of this interaction.

3.2.4 NuMA$^{1821-2115}$ is the 53BP1-binding region

To biochemically dissect the binding interface between NuMA and 53BP1 on the side of NuMA, I conducted a GST-pulldown experiment with HEK293T mitotic cell lysates. I decided to use mitotic lysates as the NuMA NLS is on the C-terminus (residues 1988-2005) and in interphase only some constructs would be nuclear. In this case cells, before being synchronized with nocodazole in prometaphase, were transfected with calcium-phosphate with different GFP-tagged NuMA constructs encompassing the whole domain structure of NuMA (figure 3.6a).

I first determined by western blot analysis the amount of GFP-NuMA Fl, GFP-NuMA$^{1-705}$, GFP-NuMA$^{705-1821}$, and GFP-NuMA$^{1821-2115}$ to be transfected in cells to ensure that the constructs were expressed at comparable levels (10 μg GFP-NuMA Fl, 0.3 μg GFP-NuMA$^{1-705}$, 0.3 μg GFP-NuMA$^{705-1821}$, and 0.5 μg GFP-NuMA$^{1821-2115}$) (figure 3.6b, input). The experiment was performed with the GST-tagged 53BP1 domain found to be the NuMA-binding region (residues 1285-1972, figure 3.5), testing its ability to pulldown the transfected GFP-NuMA constructs. Species retained on beads were analysed by

immunoblotting using anti-GFP antibody. As shown in figure 3.6b, 53BP1$^{1285-1972}$ interacts with the NuMA C-terminal region encompassing residues 1821-2115.

Notably, the identified 53BP1-BD of NuMA encompassing residues 1821-2115 is an unstructured positively charged region that over the years has been extensively studied and characterized: it contains several important domains including the MT-BDs, membrane-BDs, DNA-BD, and is highly regulated by phosphorylation events (figure 1.6c).

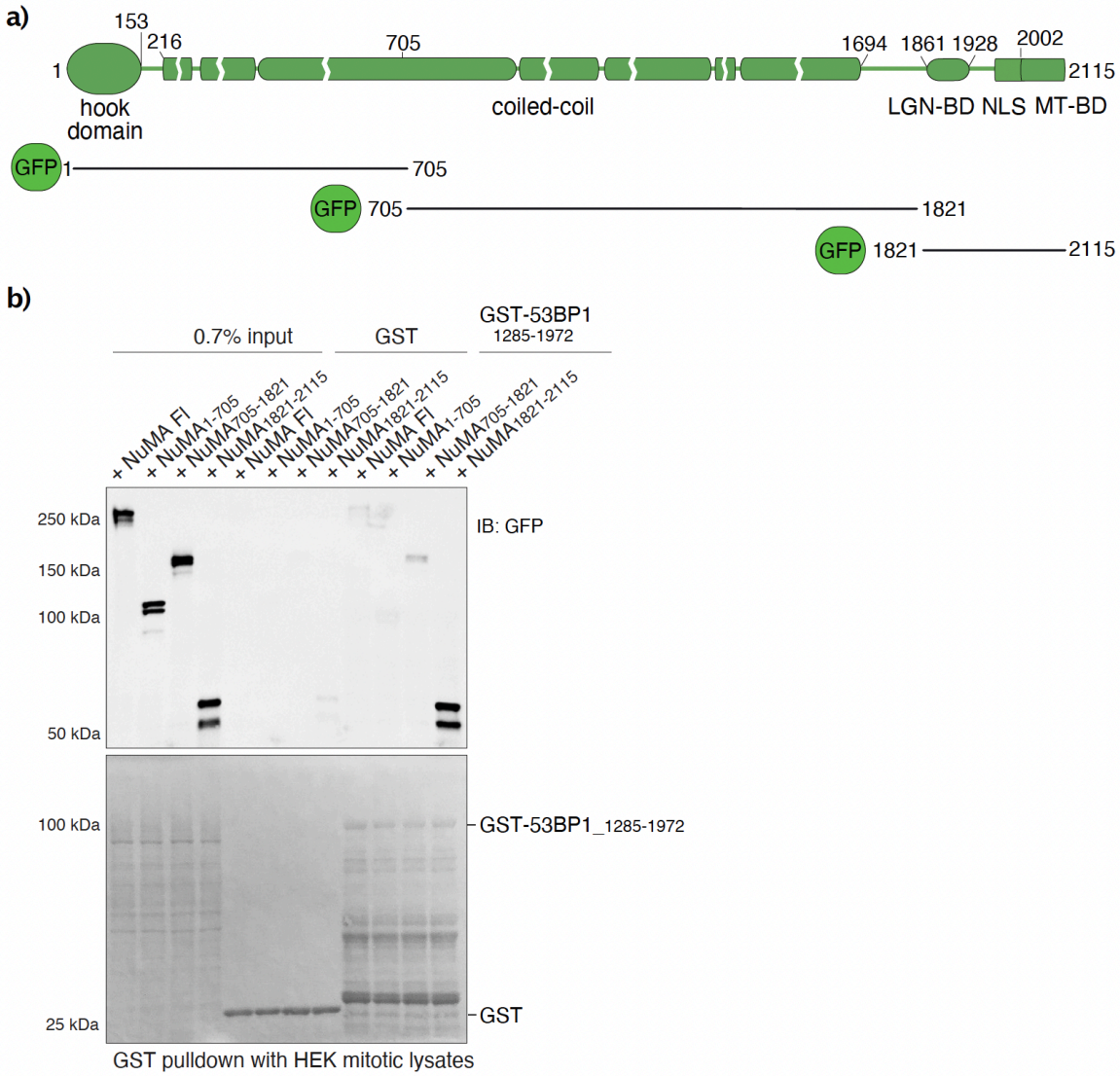

Figure 3.6 – NuMA$^{1821-2115}$ interacts with 53BP1$^{1285-1972}$ in HEK293T cells

a) *Schematic representation of human NuMA domain structure. Bold lines with numbers indicate protein subdomains used in the pulldown of panel b).* ***b)*** *GST pulldown experiment with 1 μM of GST and GST-tagged 53BP1$^{1285-1972}$ bound to GSH beads, and 1 mg of HEK293T mitotic cell lysates transfected with GFP-NuMA constructs (GFP-NuMA Fl, GFP-NuMA$^{1-705}$, GFP-NuMA$^{705-1821}$, and GFP-NuMA$^{1821-2115}$). Species retained on beads were analysed by immunoblotting for the GFP tag, and 7 μg of lysates were loaded as input. The amount of GST and of GST-53BP1 was assessed by ponceau staining.*

3.2.5 53BP1 C-terminus interacts directly with NuMA$^{1821-2115}$

Once established the domains of both 53BP1 and NuMA involved in their interaction in the interphase nucleus and in mitosis (53BP1$^{1285-1972}$ and NuMA$^{1821-2115}$), we decided to understand more in detail whether the two proteins form a direct stable complex in solution. Therefore, I performed a SEC experiment testing the ability of NuMA$^{1821-2115}$ to interact directly with 53BP1$^{1484-1972}$, a shorter and more structured portion starting from the Tudor domain (figure 3.5a). 90 µM of NuMA$^{1821-2115}$ were incubated with 90 µM of 53BP1$^{1484-1972}$ and, as shown in figure 3.7, the SEC profiles and SDS-PAGE analyses of the eluted fractions revealed that 53BP1$^{1484-1972}$ elutes in a stable complex with NuMA$^{1821-2115}$, at higher M_w with respect to the individual proteins.

We conclude that NuMA$^{1821-2115}$ interacts directly with 53BP1$^{1484-1972}$ in solution.

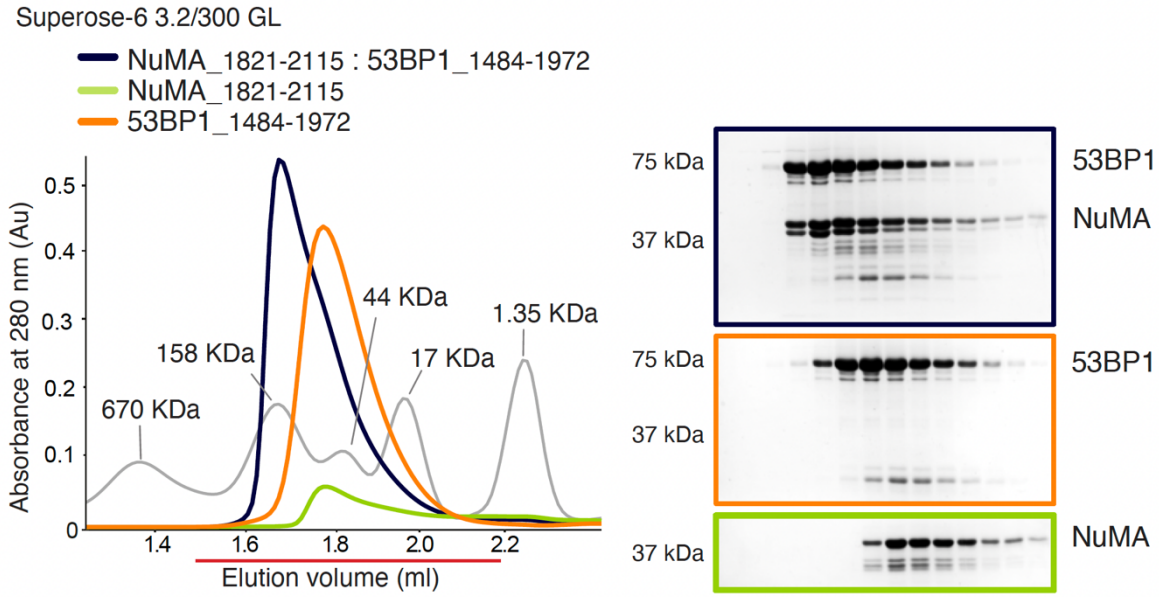

Figure 3.7 – NuMA$^{1821-2115}$ and 53BP1$^{1484-1972}$ bind directly in solution

SEC elution profile of 90 µM NuMA$^{1821-2115}$ and 90 µM 53BP1$^{1484-1972}$ mixed in a 1:1 molar ratio (black line). Eluted proteins were monitored by absorbance at 280 nm and subsequently checked by Coomassie-stained SDS-PAGE of the peak fractions corresponding to the horizontal red bar. The elution profiles of NuMA$^{1821-2115}$ alone and of 53BP1$^{1484-1972}$ are evidenced in light green and orange lines, respectively. The elution profiles of globular molecular-weight markers are evidenced in grey lines.

3.3 GFP-NuMA$^{1821-2115}$ undergoes liquid-liquid phase separation (LLPS) *in vitro*

The interaction between NuMA and 53BP1 could be promoted by weak multivalent interactions that occur in the context of LLPS (see paragraph 1.5). Evidence for this

interpretation come from literature for 53BP1 whose intrinsically disordered C-terminal region encompassing residues 1203-1972 forms LLPS droplets *in vitro* [114]. The intrinsically disordered nature of NuMA C-terminus, a property common to LLPS proteins, prompted us to test whether the NuMA-53BP1 interaction occurs in the context of LLPS.

Disorder prediction on NuMA revealed the presence of an intrinsically disordered region in its C-terminus almost after the end of the coiled-coil region (residues 1700-2115, figure 3.8a). Intrinsic disorder is a feature that is common to known phase separating proteins. For this reason, we decided to test whether the C-terminal region of NuMA interacting with 53BP1 can undergo LLPS. To this aim, I bacterially purified to homogeneity the GFP-tagged NuMA construct encompassing residues 1821-2115 by affinity, ion-exchange and size-exclusion chromatography in a high-salt buffer containing 10 mM Hepes (pH 7.5), 2 mM $MgCl_2$, 0.1 mM $CaCl_2$, 4 mM EGTA, 10% sucrose, and 0.5 M KCl, as already reported for the intrinsically disordered TPX2 N-terminal domain [129]. The SEC elution profile and Coomassie-stained SDS-PAGE analysis of GFP-NuMA$^{1821-2115}$ construct revealed the homogeneity and purity of the construct (figure 3.8b).

Using a phase-separation test (explained in the materials and methods section, paragraph 5.8), GFP-tagged NuMA$^{1821-2115}$ in high-salt buffer (0.5 M KCl) was diluted to physiological salt levels (0.1 M) and this resulted in the formation of spherical condensates not forming at 0.5 M KCl (figure 3.8c). These condensates exhibit salt-concentration-dependent condensation which is one of the criteria of LLPS.

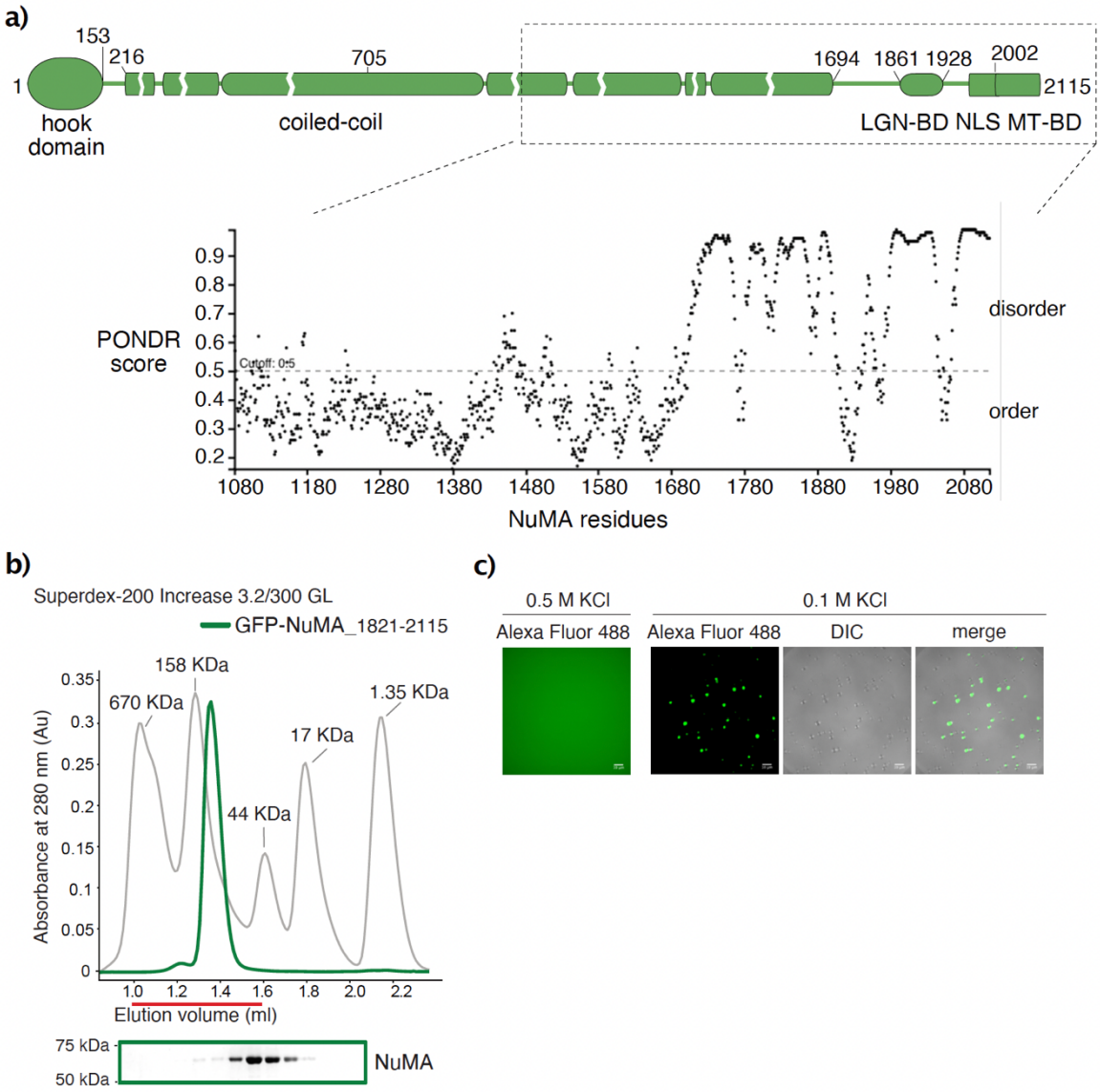

Figure 3.8 – The intrinsically disordered purified GFP-NuMA$^{1821-2115}$ protein forms liquid droplets in vitro

a) *Prediction of NuMA C-terminal intrinsic disorder (http://bioinf.cs.ucl.ac.uk/psipred/).* ***b)*** *SEC elution profile and SDS-PAGE analysis of GFP-NuMA$^{1821-2115}$ purified to homogeneity for in vitro droplet assay.* ***c)*** *Multifluo epifluorescent images at 100X magnification of GFP-NuMA$^{1821-2115}$ condensates formed at 0.1 M KCl and not at 0.5 M KCl and differential interference contrast (DIC) images of protein condensates, at a final concentration of 20 µM, forming in 10 mM Hepes (pH 7.5), 2 mM $MgCl_2$, 0.1 mM $CaCl_2$, 4 mM EGTA, 10% sucrose, 0.1 M KCl. Representative of three experimental replicates. Scale bar, 10 µM.*

Next, I generated a phase diagram testing the formation of NuMA droplets in different salt and protein concentrations (figure 3.9a-b). Phase diagrams are useful to quantitatively describe phase separation. The liquid-liquid demixing process becomes observable when proteins reach a critical concentration and physical factors such as temperature, pH and salt

concentration can affect the condensation or dissolution of LLPS [136]. In the case of NuMA the LLPS was induced by decreasing the ionic strength from 0.5 to 0.1 M KCl or increasing the NuMA concentration above 1 μM.

I then examined the effect of 1,6-hexanediol on NuMA droplets formation since this compound is known to weaken the non-electrostatic hydrophobic interactions that sometime contribute to LLPS behaviour. As shown in figure 3.9b-d, the addition of 10% of 1,6-hexanediol caused an increase of the number and size of NuMA droplets at the same protein concentration of 20 μM and in a buffer containing 0.1 M KCl. The effect was less significant than that observed for other proteins possessing low complexity sequence regions, implying a marginal relevance of non-electrostatic interactions in NuMA droplet formation. This was also seen for p53 liquid-like droplet formation, which is induced by multivalent interactions between two disordered domains [137].

Conversely, the addition to the LLPS assay of 12.5 mM ATP, a known disruptor of electrostatic and polar interactions, was found to dissolve NuMA droplets at 20 μM of concentration (figure 3.9b-d), suggesting that the phase separation behaviour of NuMA is not dependent on hydrophobic interactions but on electrostatic interactions. This is in line with the enrichment in NuMA C-terminus of positively charged residues found to be involved in the binding with DNA.

Future studies are required to understand the *in vivo* function of these NuMA condensates formed *in vitro* and specifically if they are implicated in mitotic and/or nuclear processes.

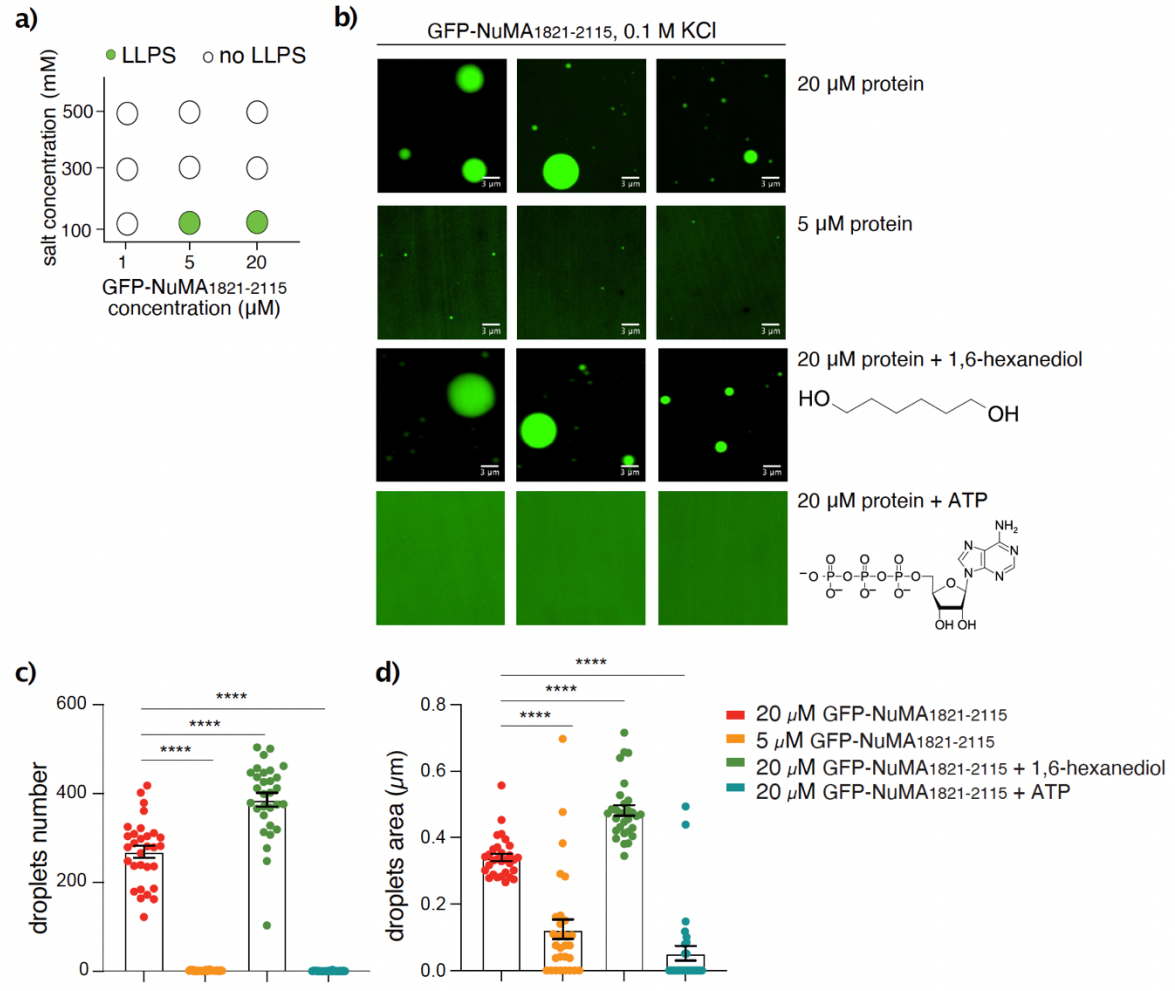

Figure 3.9 – In vitro formation of NuMA droplets with liquid properties

a) *Phase diagram of GFP-NuMA$^{1821-2115}$ at indicated KCl (mM) and protein (μM) concentrations. Green circles indicate presence and empty circles indicate absence of condensates.* ***b)*** *Representative spinning disk confocal images of GFP-NuMA$^{1821-2115}$ condensates formed at 20 μM concentration, at 5 μM of concentration, at 20 μM concentration in the presence of 10% of 1,6-hexanediol and not formed at 20 μM of concentration with the addition of 12.5 mM ATP.* ***c-d)*** *Quantification of droplets number and size of the conditions shown in panel b). Means ± SEM are shown for three independent experiments. **** indicates $p < 0.0001$; by one way ANOVA Tukey's multiple comparisons test.*

4. DISCUSSION

4.1 Biochemical characterization of the NuMA-Dynein interaction interface with implications for mitotic spindle organization

In the first part of my PhD project, in collaboration with other members of the group, I characterized the binding interface between NuMA and the LIC subunit of cytoplasmic dynein and showed that this interaction is essential for the NuMA mitotic functions of spindle assembly and positioning during metaphase.

Specifically, we provided the first structural information on the globular N-terminal head of NuMA (NuMA$^{1-153}$). The crystal structure of NuMA$^{1-153}$ revealed that it folds as a hook domain contacting both LIC1 and LIC2 isoforms with the same interaction surface used by Hook-family proteins. In addition, we identified a second LIC-BD in the N-terminal coiled-coil region of NuMA (NuMA$^{365-376}$) that is homologous to the CC1-box (consensus sequence: (D/E)xxxAAxxGxx(L/V)), a conserved motif common to another family of dynein-dynactin adaptors (figure 4.1a). We showed that these LIC-BDs of NuMA are essential for the NuMA-mediated functions of dynein in mitotic spindle assembly and orientation.

The hook domain is a variant of the CH domain, displaying the canonical 7-helices of the CH fold, featuring an extra helix at the C-terminus termed helix α8. Interestingly, the additional α-helix in the hook domains of NuMA and Hook proteins adopt a slightly different conformation. While in NuMA helices α7 and α8 are connected by an extended linker region, the corresponding residues in Hook3 are helical and the linker between the helices α7 and α8 is shorter (figure 2.5b-c).

Helix α8 in the unbound structure of the hook domain of Hook3 is fully extended, since it interacts in an antiparallel arrangement with the same helix from a symmetry-related molecule in the crystal lattice (figure 1.10f). This interaction is not physiological since Hook3$^{1-160}$ is monomeric [87] and its coiled-coil is parallel, as demonstrated by the cryo-EM structure of the Hook3-dynein-dynactin complex [84]. The helix α8 of Hook3 in the bound structure divides into two short helices (α8a and α8b), organizing a V-shaped hydrophobic cleft for binding to a conserved amphipathic helix in LIC1 C-terminus (helix α1, figure 2.5c).

By superposition of the crystal structure of the hook domains of NuMA and Hook3, we confirmed that helix α8a in NuMA assumes a flexible disordered conformation (α7-α8 loop,

figure 2.5b). The helix α8 of NuMA has the same orientation of helix α8b of Hook3, and bends back with an additional C-terminal helix, termed helix α9. The extended coiled-coil region that NuMA contains after the initial globular domain is compatible with the orientation of helices α8 and α9 observed in the crystal structure. Between the NuMA hook domain and the coiled-coil there are about 60 residues predicted to be extended and unstructured (figure 4.1a). Notably, the last helix α9 plays a fundamental role in conferring increased stability to the CH-like fold via hydrophobic interactions also involving helices α1, α7 and α8 (figure 2.5d).

Despite this diversity in the hook fold, NuMA shares with other Hook proteins the same LIC binding interface consisting of the α7-α8 loop and helix α8, which correspond respectively to helices α8a and α8b of Hook3. Pulldown experiments with purified proteins revealed that residues $Gln124^{NuMA}$ and $Leu131^{NuMA}$ in helix α8, which are conserved in Hook proteins and correspond to $Gln147^{Hook3}$ and $Ile154^{Hook3}$ in helix α8b, are essential for LIC recognition. Moreover, $Arg114^{NuMA}$ in the α7-α8 loop and $Leu135^{NuMA}$ in the helix α8 are also involved in the interaction of purified $NuMA^{1-705}$ to LIC chains (figure 2.6).

Importantly, we found that the NuMA hook domain recognizes both LIC1 and LIC2 isoforms *in vitro*, with a slightly higher affinity for LIC1, implying that in cells NuMA could work with the dynein subpopulations carrying either of the LIC variants. Whether this is the case in mitosis remains unexplored, since dynein LIC isoforms are highly regulated by PTMs [135].

The evidence that the LIC-binding site is partly disorganized in NuMA might explain the lower affinity we observed for the $NuMA^{1-705}$-LIC1 interaction compared to that of $Hook3^{1-552}$-LIC1 by comparative pulldown experiments (figure 2.10d), and to that reported for other dynein-activating adaptors [89]. However, it is also possible that, upon binding to LIC, the α7-α8 loop of NuMA rearranges by induced fit, this way reconstituting the same interface topology observed in the Hook3-LIC1 complex [89]. Unfortunately, we were unable to reconstitute the NuMA-LIC complex in solution for crystal structure determination, even at millimolar concentrations of both the hook domain of NuMA and the C-terminal domain of LIC containing the conserved helix α1 (figure 2.7).

Interestingly, sequence alignment between NuMA and known CC1-box-containing dynein-dynactin adaptors, such as SPDL1 and BICD2, revealed the existence of a second LIC-binding site in the NuMA N-terminal coiled-coil (residues 365-376, figure 2.8a). This region is homologous to the CC1-box, although it does not entirely conform to the CC1-box consensus sequence (D/E)xxxAAxxGxx(L/V), because of the two central alanine residues

having a one-residue frameshift and because of the lack of the highly conserved glycine residue. We thus named this newly identified stretch *CC1-box-like motif*.

Pulldown assays confirmed that this NuMA motif binds LIC, that the two alanine residues Ala368-Ala369^{NuMA} are essential for the interaction, that the binding is conserved throughout species despite the limited preservation, and that the NuMA contact site on LIC chains is the same α1 helix recognized by canonical CC1-boxes and hook domains (figure 2.9). Thus, our studies identified two sites on NuMA N-terminus required for the interaction with the conserved hydrophobic helix α1 in LIC1 C-terminus.

SEC and ITC experiments were performed testing the direct interaction between LIC and NuMA constructs containing both the LIC-binding interfaces, but the complex was not recapitulated in solution and the stoichiometry of the binding was not measurable (figure 2.10a-c). Mitotic PTMs, made for instance by PLK1 and CDK1 [63,70], could be required for the interaction, the binding surface of dynein on NuMA could be more extended than the one beween NuMA and LIC, or NuMA binding to dynactin potentially through the spindly-like motif (residues 417-422, figure 4.1a) could have an important role in the formation of a stable complex. Only additional structural information by single-particle cryo-EM can clarify the organizational principles of the NuMA-dynein LIC interaction.

The finding that NuMA harbours two LIC-BDs of different kind is unprecedented in dynein activating adaptors and suggests the possibility of high-stoichiometry NuMA-dynein-dynactin complexes, in which two dynein motors assemble with one NuMA dimer and one dynactin. We designed a model for the NuMA-dynein-dynactin interaction whereby the coiled-coil dimeric protein NuMA interacts with the dynein complex through two hook domains and two CC1-box-like motifs. As both interfaces seem to contact the LIC1 helix α1 on the dynein complex, we speculate that two dynein molecules could be recruited to dynactin and to the MT tracks (figure 4.1b).

This model is consistent with the ability of some adaptors, like BICDR1 and Hook3, to recruit a double dynein complex to increase the force and speed of the MT motor, with dynactin acting as a scaffold to coordinate two dynein molecules side-by-side [84].

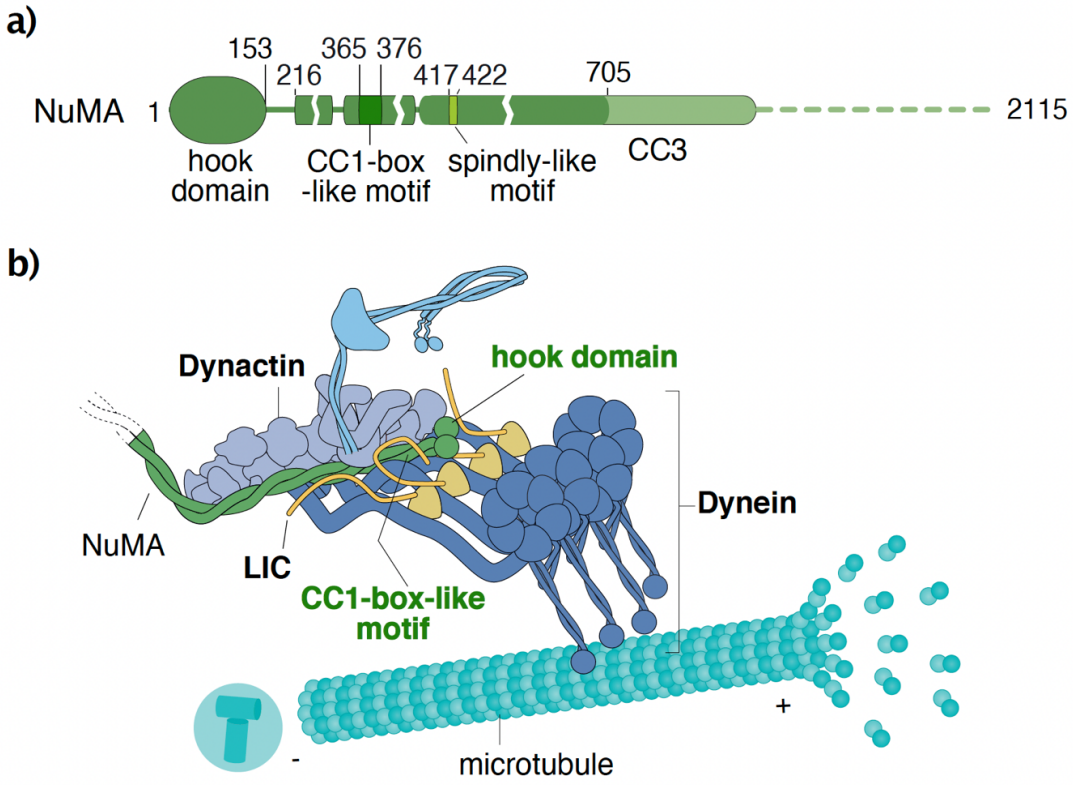

Figure 4.1 – Model for the assembly of NuMA-dynein-dynactin complexes on MT tracks

a) *Schematic representation of the N-terminal region of NuMA with highlighted the domains discovered in this study to interact directly with dynein LIC (the hook domain and the CC1-box-like motif). The spindly-like motif is a potential binding interface for the dynactin pointed-end complex.* ***b)*** *The dimeric coiled-coil NuMA interacts with the LIC subunits of dynein through the hook domains and CC1-box-like motifs. As both interfaces contact the C-terminal helix α1 of LIC, we speculate that NuMA recruits two dynein molecules to the same dynactin complex and to the MT tracks. Green, NuMA; yellow, LIC; blue, dynein; light blue, dynactin; light green, MTs.*

The characterization of the LIC-binding mode of NuMA adds support to NuMA being a *bona fide* dynein activating adaptor for its mitotic functions in spindle assembly and positioning. To start addressing the relevance of the newly identified NuMA-dynein binding interfaces *in vivo*, we conducted rescue experiments in epithelial HeLa cells with NuMA truncation mutants lacking both the hook domain and the CC1-box-like motif ($NuMA^{\Delta 1-705}$) or either one LIC-binding interface ($NuMA^{\Delta 1-153}$ or $NuMA^{\Delta 154-705}$) or mutated only in the alanine couple of the CC1-box-like motif ($NuMA^{A368V/A369V}$). These assays revealed that LIC-interacting motifs are essential for correct mitotic progression, fully supporting the notion that NuMA acts as a mitotic dynein adaptor. Notably, the point mutant $NuMA^{A368V/A369V}$ rescued the phenotype, suggesting that, in this kind of assay, the disruption of the CC1-box like motif is tolerated within the NuMA-dynein complex (figures 2.11-2.12).

These findings are consistent with the requirement of the N-terminal dynein-binding motif of NuMA for spindle pole focusing, as already uncovered [59]. Recently the dynein-dynactin adaptor Hook2 was found to have a role in chromosome congression and spindle positioning in HeLa cells, although the defects of Hook2-depleted cells seem to be ascribed to dynein-independent MT nucleation errors at the spindle poles [17]. This evidence is consistent with the existence in mitotic cells of several pools of dynein-dynactin complexes, assembled on different adaptors, that function in distinct dynein-mediated activities. An interesting observation derived from our rescue assays is that NuMA truncations impairing dynein binding do not affect the localization of NuMA at the spindle poles, implying that a NuMA receptor exists at the spindle poles beside dynein and the MTs. This result is consistent with the evidences that Aurora-A controls NuMA localization at the poles by phosphorylating the C-terminal region of the protein [58] and that NuMA recruits dynein activity to the spindle poles and not vice versa [59]. A screening of NuMA-binding proteins by mass spectrometry in mitotic cells could be useful to identify the spindle-pole receptor for NuMA. Knock-down of the hypothetical spindle-pole receptor for NuMA will reduce significantly the enrichment of NuMA on the poles.

To reconstitute the NuMA-dynein-dynactin complex from recombinant sources, we performed binding assays with MBP-tagged purified NuMA N-terminal constructs and HEK293T mitotic cell extracts (figure 2.1). This experiment revealed that dynein and dynactin interact with NuMA$^{1-705}$, but do not form a complex with shorter constructs. This evidence is consistent with the co-IP performed by Kotak and colleagues in 2012 [32]. We concluded that, to assemble the dynein-dynactin complex, NuMA requires a coiled-coil region of about 500 residues, which is much longer than the one needed by the adaptor Hook3 (Hook3$^{1-239}$) [87]. Indeed, comparative pulldown experiments with purified LIC1 and increasing concentrations of NuMA$^{1-705}$ or Hook3$^{1-552}$ confirmed a lower affinity of NuMA$^{1-705}$ for LIC with respect to that of Hook3$^{1-552}$ (figure 2.10d).

In conclusion, the combination of structural, biochemical, and functional data collected in this study support the hypothesis that NuMA is a mitotic dynein-dynactin activating adaptor assisting spindle organization and positioning.

Recently, using a photo-inducible system, Okumura and colleagues revealed that optogenetic recruitment of dynein and dynactin to the cortex cannot generate enough forces to displace the spindle and that cortical NuMA is required for this process [53]. Molecularly, it is possible that NuMA confers high processivity to dynein movement on astral MTs, or that it induces a conformational change required for effective pulling. Our lab also demonstrated that NuMA-LGN binding at the cortex with the combination of donuts and

coiled-coils generate a protein network at the cortex whose spatial organization might be essential in generating effective pulling forces on astral MTs [36].

Future biochemical studies are needed to investigate the ability of NuMA to activate processive dynein movements on MT tracks. The gold standard for determining if a candidate adaptor is a dynein–dynactin activator is to reconstitute motility from purified components. In this approach, each protein is purified separately, and at least one component is fluorescently tagged. Motility is then monitored using total internal reflection fluorescence (TIRF) microscopy [73]. We tried this approach with bacterially purified NuMA$^{1-705}$, recombinant dynein and purified dynactin in collaboration with the Andrew Carter lab, but unfortunately this N-terminal NuMA fragment purified did not suffice to reconstitute a complex able to promote dynein movement on the MT tracks. For the considerations reported above, we think that trying with a NuMA$^{1-705}$ fragment purified from mitotic HEK293T cells, and hence carrying physiological mitotic PTMs, might help increasing the affinity of NuMA to the MT motors. In addition, future single-particle cryo-EM structural studies are needed to explore the overall topology of the NuMA-dynein-dynactin macromolecular complexes forming during mitosis to sustain spindle functions.

4.2 Biochemical characterization of the NuMA-53BP1 interaction interface with implications for the liquid-liquid phase separation (LLPS) mechanism

In the second part of my PhD project, I focused on the characterization of the protein NuMA in the nucleus of human interphase cells, with emphasis on its contribution to the DDR as negative regulator of the recruitment of 53BP1 to DSBs [2].

Nuclear fractionation experiments revealed that NuMA localizes both in the soluble nucleoplasm and insoluble chromatin and nuclear matrix fractions. By co-IP experiments I further found that endogenous NuMA interacts with histone H3, in this way pointing out the importance of NuMA in chromatin organization. This is consistent with recent reports of the NuMA association with DNA [56,63]. NuMA$^{2058-2115}$ binds DNA *in vitro* and interacts with chromatin in cells for proper regulation of chromatin decompaction during nuclear reformation and for maintaining the proper nuclear architecture [56,63].

By co-IP experiments in HEK293T nuclear extracts, I scored an interaction between endogenous NuMA and 53BP1 that is reduced upon DNA damage induction by doxorubicin treatment. Because NuMA itself is not recruited to DDR foci, the results of my IP support the notion that NuMA prevents 53BP1 recruitment at DNA in the absence of DNA damage, as already reported [2].

I then characterized the biochemical interaction interface between the proteins NuMA and 53BP1, which I showed to occur not only in the nucleus in the absence of DNA damage, but also during mitosis when 53BP1 plays a prominent role in the centrosome surveillance pathway. To map the binding interface between NuMA and 53BP1, I performed pulldown assays with nuclear and mitotic lysates and purified truncated constructs, encompassing the whole domain structure of both NuMA and 53BP1. These experiments revealed that the C-terminus of 53BP1 ($53BP1^{1285-1972}$) interacts directly with the C-terminus of NuMA ($NuMA^{1821-2115}$) (figure 4.2a).

Our data are in line with the experiments performed by Moreno and colleagues, which found using a proteomics approach and FRET experiments that NuMA interacts with the 53BP1 IRIF region, encompassing residues 1220-1711 [2]. Another interesting finding from Moreno lab is that NuMA phosphorylation by ATM in response to DSBs acts a release mechanism, allowing 53BP1 accumulation at damaged chromatin [2]. However, this mechanism deserves further investigation since NuMA is phosphorylated by ATM at the N-terminus (Ser395) and interacts with 53BP1 through its C-terminal domain.

Interestingly, analytical SEC experiments performed to test the direct interaction between NuMA and 53BP1 C-terminal domains (figure 3.7), revealed that the elution profiles of $NuMA^{1821-2115}$ and of $53BP1^{1484-1972}$, when injected on the SEC column together, are shifted toward a higher M_w, demonstrating that the two proteins form a stable complex in solution. In the future it will be interesting to map the minimal binding region involved in the interaction to reconstitute the NuMA-53BP1 complex in solution for crystal structure determination.

As shown in figure 4.2b, the NuMA-BD of 53BP1 comprises the tandem Tudor domain which is involved in the direct interaction with the DSB-specific constitutive histone mark H4K20me2 [138]. This Tudor domain, in the absence of DNA damage, is masked by the factor TIRR, whose interaction with 53BP1 is decreased in response to DNA damage, as it happens for the NuMA-53BP1 interaction. Hence, TIRR and NuMA may act as distinct nuclear negative regulators of 53BP1 DNA repair function in a normal cell nucleus.

Both 53BP1 and NuMA have intrinsically disordered regions based on Disopred3 prediction (http://bioinf.cs.ucl.ac.uk/psipred/). These kinds of domains are commonly found in proteins that undergo LLPS, a mechanism conferring spatial and temporal regulation to biological processes.

In line with these thoughts, 53BP1 has been shown to form DNA damage foci with LLPS condensates properties, that are promoted by its C-terminal disordered region [114]. Because also the C-terminal portion of NuMA interacting with 53BP1 is predicted to be disordered (figure 3.8a), I hypothesized that in the absence of damage, the interaction of NuMA with

53BP1 could occur in LLPS condensates. To test this idea, I first checked whether NuMA could undergo LLPS itself. Interestingly, I found that GFP-tagged purified NuMA$^{1821-2115}$ forms liquid droplets *in vitro* at 5-20 μM and physiological 0.1 M KCl salt concentrations. These droplets were found to be promoted by electrostatic and polar interactions and not by hydrophobic interactions, since they dissolve in the presence of ATP and increase in number and size upon addition of the hydrophobic disruptor aliphatic alcohol 1,6-hexanediol (figure 3.9).

By co-IP experiments in HEK293T nuclear extracts, I also detected an interaction of NuMA with the MT nucleator TPX2. Since TPX2 counteracts the 53BP1 DSB repair function during replication stress [132] and in mitosis undergoes LLPS through its N-terminal intrinsically disordered region [129], I hypothesized that NuMA could work with TPX2 in regulating the 53BP1 DDR function by forming dynamic LLPS condensates.

Unexpectedly, by co-IP experiments, the interaction between NuMA and 53BP1 was also scored during mitosis. It is known that in mitosis 53BP1, together with the proteins USP28 and p53, is part of the mitotic surveillance pathway, another condensate-associated regulatory process forming at mitotic spindle poles to activate p53 for cell cycle arrest upon centrosome loss or prolonged mitosis [121].

Finally, to organize the preliminary information collected by my *in vitro* studies, I designed a model for the potential regulation of 53BP1 DDR function by the proteins NuMA and TPX2. While 53BP1 is accumulated at DNA damage foci upon DSB induction, under physiological conditions it could be sequestered into LLPS condensates formed by NuMA and TPX2 in the nucleus during interphase to avoid undue activation of the DDR and/or at the spindle poles during mitosis (figure 4.2c).

Future studies are required to uncover the molecular basis and the functional role of the NuMA-53BP1 interaction both in the DNA damage and in the mitotic surveillance pathway contexts.

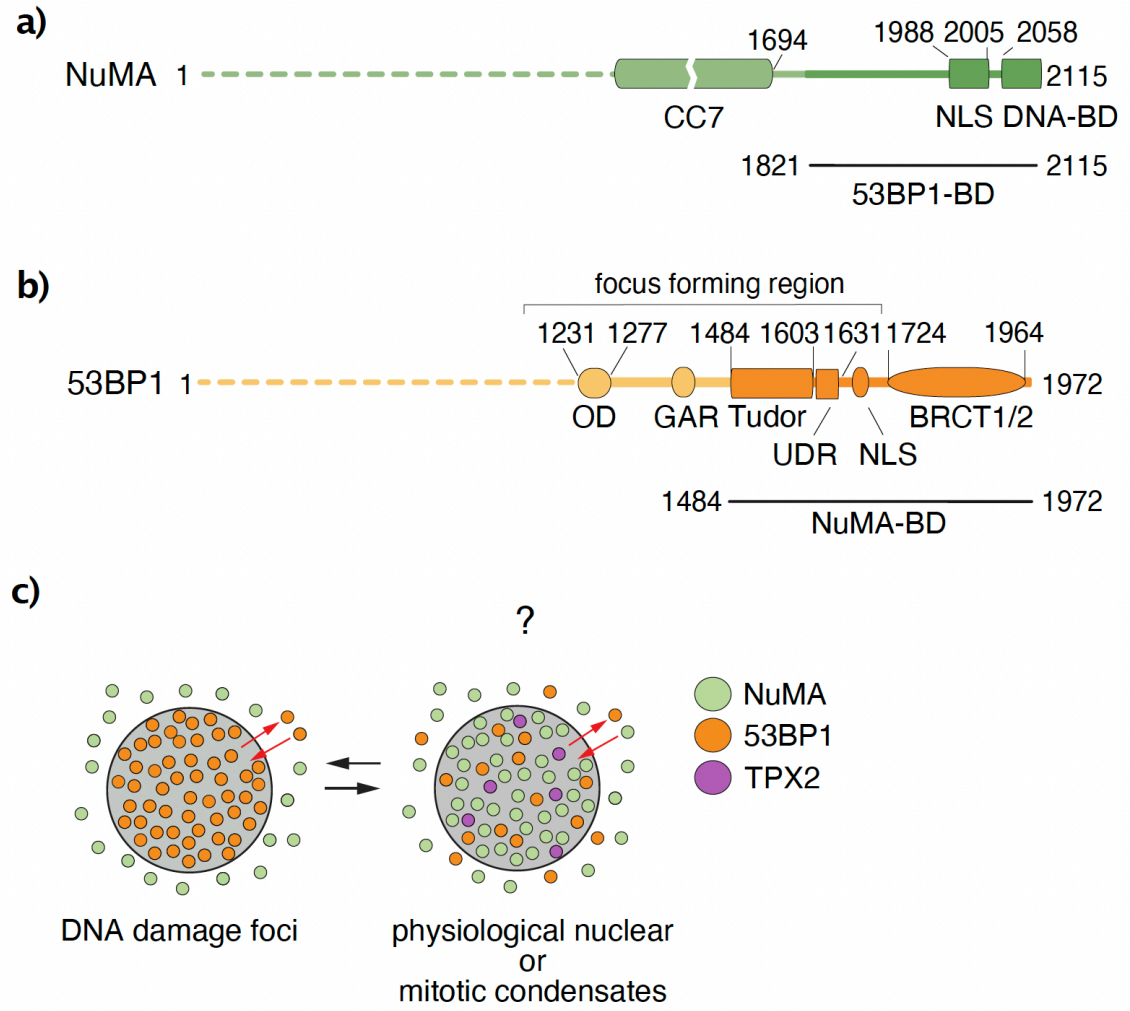

Figure 4.2 – Model for the NuMA-53BP1 assembly

a) *Schematic representation of the C-terminal region of NuMA with highlighted the domain discovered in this study to interact directly with 53BP1.* ***b)*** *Schematic representation of the C-terminal region of 53BP1 with highlighted the domain discovered in this study to interact directly with NuMA.* ***c)*** *Model of the potential regulation of 53BP1 condensates by NuMA and TPX2. Induction of DNA DSBs leads to the formation of DNA damage foci enriched of the DNA damage response protein 53BP1 that repairs the damaged DNA. In the absence of DNA damage, NuMA and TPX2 act to sequester 53BP1 in dynamic biomolecular condensates, to avoid its interaction with chromatin. NuMA-53BP1 condensates formation could also happen during mitosis.*

In this perspective, to test the possibility that NuMA, TPX2 and 53BP1 are part of the same LLPS condensates, I would like to perform *in vitro* droplet assays testing the co-condensation of GFP-tagged NuMA$^{1821\text{-}2115}$ with mCherry-tagged 53BP1$^{1203\text{-}1972}$ and TPX2$^{1\text{-}512}$ (the domains of 53BP1 and TPX2 found in literature [114,129] to undergo LLPS *in vitro*). Of note, this 53BP1 protein construct contains the OD (residues 1231-1277) that stimulates the accumulation of 53BP1 at sites of DNA damage and promotes the self-assembly of 53BP1 into phase-separated condensates. Another idea could be to study the co-condensation of

GFP-NuMA$^{1821-2115}$ with mCherry-53BP1$^{1484-1972}$, the 53BP1 domain that we found to interact directly with NuMA and that does not phase separate alone [114], testing our hypothesis that the NuMA-53BP1 interaction prevents 53BP1 oligomerization required for its DNA repair function and liquid-like behaviour.

Further studies are required to study the physicochemical properties of NuMA LLPS droplets. Fluorescence recovery after photobleaching (FRAP) analysis could be also useful to study the mobility and dynamics within NuMA droplets *in vitro* in the presence and absence of other interactors [139].

A more insightful step will be to perform studies in cells to understand the functional relevance of the NuMA biomolecular condensates and in which biological context they are implicated *in vivo*. Specifically, it would be interesting to check whether foci-like condensates of NuMA are visible in the nucleus [63], and if they dissolve after DNA damage induction in the cell nucleus. This can be done with super resolution microscopy experiments conducted with CRISPR/Cas9-engineered HCT116-GFP-NuMA cell lines expressing NuMA at endogenous levels (generous gift of Dr. Kiyomitsu).

Additionally, to figure out the molecular mechanism regulating condensate formation, phase separation assays and imaging experiments of cells transfected with GFP-NuMA$^{1821-2115}$ constructs carrying point mutations possibly inhibiting phase separation *in vitro* will be performed. Since PTMs are suggested as a mechanism dissolving condensates, being NuMA highly phosphorylated at its C-terminus, some of the numerous positively charged Arg residues could be mutated to study this regulatory mechanism.

5. MATERIALS AND METHODS

5.1 Molecular cloning

Synthetic cDNA coding for human NuMA (NCBI reference sequence NM_006185) was previously subcloned in the lab in a pCDH-Ubc mammalian expression vector with an N-terminal mCherry-tag [58]. The fragments of NuMA spanning residues 1-705, 154-705 and 1821-2115 were generated by PCR amplification and cloned into a pETM14 bacterial expression vector (Novagen) in frame with a cleavable N-terminal hexa-histidine tag.

For the structural and biophysical studies, NuMA$^{1-153}$ and NuMA$^{1-414}$ were obtained by introducing a stop codon in the His-NuMA$^{1-705}$ pETM14 vector by QuikChange site-directed mutagenesis (Agilent), and sequence verified.

For the binding studies, the point mutations R114A, W116A, Y121A, Q124A, L131A, L135A and A368V/A369V were introduced in His-NuMA$^{1-705}$ by QuikChange mutagenesis and sequence verified.

NuMA$^{1-705}$ was also subcloned in a pET43.1a-6xHis-MBP bacterial expression vector in frame with a cleavable N-terminal MBP tag. The shorter MBP-tagged NuMA constructs (NuMA$^{1-400}$, NuMA$^{1-260}$, NuMA$^{1-153}$) were obtained by introducing a stop codon in the His-MBP-NuMA$^{1-705}$ pET43.1a vector by QuikChange mutagenesis.

The mCherry-tagged NuMA$^{\Delta 1-153}$ and NuMA$^{\Delta 1-705}$ rescue constructs were generated by PCR amplification and cloned in a pCDH-Ubc vector. The mCherry-NuMA$^{\Delta 154-705}$ construct was obtained by deletion using 5'-phosphorylated primers (table 5.1). The mCherry-NuMA$^{A368V/A369V}$ construct was generated by QuikChange mutagenesis from the synthetic NuMA gene, sequence verified, and inserted into a pCDH-Ubc vector by restriction cloning.

NuMA Fl, NuMA$^{1-705}$, NuMA$^{705-1821}$ and NuMA$^{1821-2115}$ were cloned in a pCDH-Ubc vector in frame with an N-terminal GFP tag.

For the LLPS studies, GFP-NuMA$^{1821-2115}$ was generated by PCR amplification and cloned into a pET43-His vector in frame with a cleavable N-terminal GFP tag.

Dynein LIC1 Fl (LIC1$^{1-523}$) and C-terminus (LIC1$^{390-523}$), and LIC2 Fl (LIC2$^{1-492}$) and C-terminus (LIC2$^{379-492}$) were generated by PCR amplification using as template human LIC1 cDNA (GE Dharmacon), and human LIC2 cDNA retrotranscribed from HeLa cells. PCR products were cloned into a pGEX-6PI bacterial expression vector in frame with a cleavable N-terminal GST tag. The point mutations F447A/F448A were introduced in GST-LIC1$^{1-523}$ by QuikChange mutagenesis and sequence verified.

For the analytical SEC experiments of figures 2.7 and 2.10b, LIC1$^{390-523}$ and LIC2$^{379-492}$ were cloned into a pET43 vector in frame with an uncleavable N-terminal hexa-histidine tag.

For the SEC experiment of figure 2.10c, MBP-tagged LIC1$^{1-523}$ was cloned in a pET30a bacterial expression vector in frame with a C-terminal hexa-histidine tag.

The mammalian expression vector pcDNA5-FRT/TO-eGFP-53BP1 (Addgene, #60813), gifted by Dr. Stefano Santaguida, was used as template to generate 53BP1 constructs for bacterial expression. The fragments of 53BP1 spanning residues 1-595, 596-1219, 596-1284, 1285-1972, and 1484-1972 were generated by PCR amplification, and cloned into a pGEX-6PI vector in frame with a cleavable N-terminal GST tag.

All gene cloning, manipulation and plasmid propagation steps were carried out in *E. coli* TOP10 cells (for bacterial vectors) and in *E. coli* Stbl3 cells (for mammalian vectors) grown in LB media supplemented with appropriate selection antibiotics. A list of the oligonucleotides used for cloning is provided in table 5.1.

Table 5.1

Recombinant DNA	**DNA oligonucleotides 5' to 3'**
pETM14-His-NuMA-1-705	Restriction cloning forward: GCGCGCCCATGGGTATGACCCTGCACGCTACC reverse: GCGCGCGTCGACTTATTGCAGCTGCTCTTGGAG
pETM14-His-NuMA-1-705-R114A	Site directed mutagenesis forward: ATGTCCTCCAAGTCCCCTGCTGACTGGGAGCAGTTCGAG reverse: CTCGAACTGCTCCCAGTCAGCAGGGGACTTGGAGGACAT
pETM14-His-NuMA-1-705-W116A	Site directed mutagenesis forward: TCCAAGTCCCCTCGTGACGCGGAGCAGTTCGAGTACAAG reverse: CTTGTACTCGAACTGCTCCGCGTCACGAGGGGACTTGGA
pETM14-His-NuMA-1-705-Y121A	Site directed mutagenesis forward: GACTGGGAGCAGTTCGAGGCCAAGATCCAGGCTGAGCTG reverse: CAGCTCAGCCTGGATCTTGGCCTCGAACTGCTCCCAGTC
pETM14-His-NuMA-1-705-Q124A	Site directed mutagenesis forward: CAGTTCGAGTACAAGATCGCGGCTGAGCTGGCTGTGATC reverse: GATCACAGCCAGCTCAGCCGCGATCTTGTACTCGAACTG
pETM14-His-NuMA-1-705-L131A	Site directed mutagenesis forward: GCTGAGCTGGCTGTGATCGCGAAGTTCGTGCTGGACCAC reverse: GTGGTCCAGCACGAACTTCGCGATCACAGCCAGCTCAGC
pETM14-His-NuMA-1-705-L135A	Site directed mutagenesis forward: GTGATCCTGAAGTTCGTGGCGGACCACGAGGACGGCCTG reverse: CAGGCCGTCCTCGTGGTCCGCCACGAACTTCAGGATCAC
pETM14-His-NuMA-1-705-A368V/A369V	Site directed mutagenesis forward: CTGGAAAAGGAACTGAGCGTTGTTCTCCAGGACAAGAAGTGC reverse: GCACTTCTTGTCCTGGAGAACAACGCTCAGTTCCTTTTCCAG
pETM14-His-NuMA-1-414	Site directed mutagenesis forward: GTGCTGGGCGACACTAGTCAGTAAGAAACCCTGAAGCAAGAGGCT reverse: AGCCTCTTGCTTCAGGGTTTCTTACTGACTAGTGTCGCCCAGCAC
pETM14-His-NuMA-1-153	Site directed mutagenesis forward: GAAAACTTCCTGCAAAAGTGACCCGTGCCCTCTACCTGC reverse: GCAGGTAGAGGGCACGGGTCACTTTTGCAGGAAGTTTTC

pETM14-His-NuMA-154-705	Restriction cloning forward: GCGCGCCCATGGGTGCTCCCGTGCCCTCTACC reverse: GCGCGCGTCGACTTATTGCAGCTGCTCTTGGAG
pETM14-His-NuMA-1821-2115	Restriction cloning forward: GCGCGCCCATGGGTAAGAAGCTAGATGTGGAA reverse: GCGCGCGTCGACTTAGTGCTTAGCCTTGCCCTTAGC
pET43.1a-His-MBP-NuMA-1-705	Restriction cloning forward: GCGCGCGGATCCATGACCCTGCACGCTACC reverse: GCGCGCGGTACCTTATTGCAGCTGCTCTTGGAG
pET43.1a-His-MBP-NuMA-1-400	Site directed mutagenesis forward: CTCTCCCAGCTGCAAGACAACTAACCCCAAGAGAAGGGCGAGGTG reverse: CACCTCGCCCTTCTCTTGGGGTTAGTTGTCTTGCAGCTGGGAGAG
pET43.1a-His-MBP-NuMA-1-260	Site directed mutagenesis forward: CAGCAGCGTATCGACCGTTAGGCTCTCCTGAACGAGAAG reverse: CTTCTCGTTCAGGAGAGCCTAACGGTCGATACGCTGCTG
pET43.1a-His-MBP-NuMA-1-153	Site directed mutagenesis forward: GAAAACTTCCTGCAAAAGTGACCCGTGCCCTCTACCTGC reverse: GCAGGTAGAGGGCACGGGTCACTTTTGCAGGAAGTTTTC
pET43-His-GFP-NuMA-1821-2115	Restriction cloning forward: GCGCGCAGATCTATGGTCTCCAAGGGCGAG reverse: GCGCGCGTCGACTTAGTGCTTTGCCTTGCCCTT
pCDH-Ubc-mCherry-NuMA	Restriction cloning forward: GCGCGCGCTAGCATGACCCTGCACGCTACCCGT reverse: GCGCGCGGATCCGAGTGCTTAGCCTTGCCCTT
pCDH-Ubc-mCherry-NuMA-Δ1-153	Restriction cloning forward: GCGCGCGCTAGCATGGCTCCCGTGCCCTCTACC reverse: GCGCGCGGATCCGAGTGCTTAGCCTTGCCCTT
pCDH-Ubc-mCherry-NuMA-Δ154-705	Primers for sequence deletion forward: GCTCTGAAGGAATCCCTGAAGG (5'-phosphorylated) reverse: AGCCTTTTGCAGGAAGTTTTCC (5'-phosphorylated)
pCDH-Ubc-mCherry-NuMA-Δ1-705	Restriction cloning forward: GCGCGCGCTAGCATGGCTCTGAAGGAATCCCTG reverse: GCGCGCGGATCCGAGTGCTTAGCCTTGCCCTT
pCDH-Ubc-GFP-NuMA	Restriction cloning forward: GCGCGCGGATCCATGACCCTGCACGCTACC reverse: GCGCGCCTCGAGGTGCTTAGCCTTGCCCTTAGC
pCDH-Ubc-GFP-NuMA-1-705	Restriction cloning forward: GCGCGCGGATCCATGACCCTGCACGCTACC reverse: GCGCGCCTCGAGTTGCAGCTGCTCTTGGAG
pCDH-Ubc-GFP-NuMA-705-1821	Restriction cloning forward: GCGCGCGGATCCATGCAAGCTCTGAAGGAATCCCTG reverse: GCGCGCCTCGAGCTTGGCCATGGTGATGTTGATGATCTG
pCDH-Ubc-GFP-NuMA-1821-2115	Restriction cloning forward: GCGCGCGGATCCATGAAGAAGTTGGACGTCGAGGAACCC reverse: GCGCGCCTCGAGGTGCTTAGCCTTGCCCTTAGC
pGEX-6PI-GST-LIC1-1-523	Restriction cloning forward: GCGCGCGGATCCATGGCGGCCGTGGGGCGA reverse: GCGCGCGTCGACTTAAGAAGCTTCTCCTTCCGT
pGEX-6PI-GST-LIC1-1-523 F447A/F448A	Site directed mutagenesis forward: AGTGAAGGCGTTCTGGCAAATGCCGCCAACAGTTTGTTGAGTAAAAAG reverse: CTTTTTACTCAACAAACTGTTGGCGGCATTTGCCAGAACGCCTTCACT

pGEX-6PI-GST-LIC1-390-523	Restriction cloning forward: GCGCGCGGATCCATGGCAGCTGGAAGGCCTGTG reverse: GCGCGCGTCGACTTAAGAAGCTTCTCCTTCCGT
pGEX-6PI-GST-LIC2-1-492	Restriction cloning forward: GCGCGCGAATTCGTATGGCGCCGGTGGGGGTGGAG reverse: GCGCGCGTCGACTCAGGCTTCATTTTCTGTTGAAGAG
pGEX-6PI-GST-LIC2-379-492	Restriction cloning forward: GCGCGCGAATTCGTATGAGAGCTTCTGAATCTCCT reverse: GCGCGCGTCGACTCAGGCTTCATTTTCTGTTGAAGAG
pET30a-MBP-LIC1-1-523-His	Restriction cloning forward: GCGCGCCATATGAAAACTGAAGAAGGTAAACTG reverse: GCGCGCCTCGAGAGAAGCTTCTCCTTCCGTAGG
pGEX-6PI-GST-53BP1-1-595	Restriction cloning forward: GCGCGCGGATCCATGGACCCTACTGGAAGTCAG reverse: GCGCGCGTCGACTTAATCCCTGGTGTCTGTATCATC
pGEX-6PI-GST-53BP1-596-1219	Restriction cloning forward: GCGCGCGGATCCATGGACATTAGTATTTTAGCCACTGGTTGC reverse: GCGCGCGTCGACTTAGCTATGGAGCGACTCTGTATC
pGEX-6PI-GST-53BP1-596-1284	Restriction cloning forward: GCGCGCGGATCCATGGACATTAGTATTTTAGCCACTGGTTGC reverse: GCGCGCGTCGACTTATTCACACTCCTGACACTCTAC
pGEX-6PI-GST-53BP1-1285-1972	Restriction cloning forward: GCGCGCGGATCCATGACTGAAGTTTCCCCTTCACAG reverse: GCGCGCGTCGACTTAGTGAGAAACATAATCGTGTTTATATTTTGG
pGEX-6PI-GST-53BP1-1484-1972	Restriction cloning forward: GCGCGCGGATCCATGAATAGCTTTGTAGGGCTCCG reverse: GCGCGCGTCGACTTAGTGAGAAACATAATCGTGTTTATATTTTGG

5.2 Protein expression and purification

The His-NuMA$^{1-153}$ construct was expressed in BL21 Rosetta *E. coli* cells by 16 hours induction with 0.5 mM IPTG at 20 °C. Cells were lysed in His-lysis buffer containing 0.1 M Tris-HCl (pH 8.0), 0.3 M NaCl, 10% glycerol, 5 mM imidazole (pH 8.0), 2 mM β-mercaptoethanol and protease inhibitors (Calbiochem), sonicated and cleared for 1 hour at 100,000 *g*. Clear lysates were injected on a HiTrap chelating column (GE Healthcare) loaded with $NiCl_2$, and washed with 1.0 M NaCl and 15 mM imidazole. His-NuMA$^{1-153}$ was eluted with a 0.02 M – 0.16 M imidazole gradient. Peak fractions were dialysed overnight at 4 °C against a desalting buffer consisting of 30 mM Tris-HCl (pH 8.0), 0.1 M NaCl, 5% glycerol and 1 mM DTT, while incubating with Prescission protease to remove the histidine-tag. The protein was then injected onto a Resource-Q anion exchange column (GE Healthcare) and eluted by a salt gradient from 0.03 M to 0.2 M NaCl over 20 column volumes. NuMA$^{1-153}$ was further polished on a Superdex-200 16/600 column equilibrated in 10 mM Tris-HCl (pH 6.8), 0.1 M NaCl, 5% glycerol and 1 mM DTT (figure 2.2b). Peak fractions were analysed by SDS-PAGE, pooled and concentrated to 33 mg/ml (2 mM) prior freezing at -80 °C.
For SAD experiments, NuMA$^{1-153}$ was expressed in a methionine auxotroph (Met$^-$) bacterial strain grown in a Se-Met minimal medium (Molecular Dimensions #MD12-501).

The His-NuMA$^{1-705}$ construct was expressed in BL21 Rosetta *E. coli* cells by 5 hours induction with 0.5 mM IPTG at 20 °C. Cells were lysed in His-lysis buffer, sonicated and cleared. The over-expressed protein was purified by affinity chromatography on a HiTrap chelating column loaded with $NiCl_2$, washed with 3.0 M NaCl and 15 mM imidazole, eluted by a 0.025 M – 0.2 M imidazole gradient, and then dialysed overnight at 4 °C against desalting buffer, while incubating with Prescission protease. The protein was then injected onto a Resource-Q anion exchange column and eluted by a salt gradient from 0.04 M to 0.3 M NaCl over 12 column volumes. NuMA$^{1-705}$ was further polished on a Superose-6 10/300 column equilibrated in 10 mM Hepes (pH 7.5), 0.1 M NaCl, 5% glycerol and 1 mM DTT (figure 2.2a). Peak fractions were analysed by SDS-PAGE, pooled and concentrated to 40 mg/ml (500 μM) prior freezing at -80 °C. The His-NuMA$^{1-705}$ WT and mutated constructs for pulldown experiments were purified by affinity and anion exchange chromatography without the His-tag removal and the step of gel filtration.

NuMA$^{154-705}$ and NuMA$^{1-414}$ were expressed in BL21 *E. coli* cells by 5 hours induction with 0.5 mM IPTG at 20 °C and purified as described for NuMA$^{1-705}$. The SEC elution profile of NuMA$^{154-705}$ is shown in figure 2.2a.

For the analytical SEC experiments of figure 3.7, His-NuMA$^{1821-2115}$ was expressed in BL21 *E. coli* cells by 5 hours induction with 0.5 mM IPTG at 20 °C. Cells were lysed in His-lysis buffer, sonicated and cleared. The over-expressed protein was purified by affinity chromatography on a HiTrap chelating column loaded with $NiCl_2$, washed with 3.0 M NaCl and 15 mM imidazole, eluted by a 0.025 M – 0.25 M imidazole gradient, and the peak fractions desalted on a HiTrap desalting column in a buffer consisting of 30 mM Tris-HCl (pH 6.8), 0.1 M NaCl, 5% glycerol and 1 mM DTT. The protein was then injected onto a Resource-S cation exchange column (GE Healthcare) and eluted at 0.4 M NaCl. Peak fractions were analysed by SDS-PAGE, pooled, dialysed 3 hours at 4 °C in 10 mM Tris-HCl (pH 8.0), 0.2 M NaCl, 10% glycerol, 1 mM DTT, and concentrated to 6.0 mg/ml (180 μM) prior freezing at -80 °C.

For the LLPS studies, GFP-NuMA$^{1821-2115}$ was expressed in BL21 *E. coli* cells by 5 hours induction with 0.5 mM IPTG at 20 °C. Cells were lysed in His-lysis buffer, sonicated and cleared. The over-expressed protein was affinity purified by incubation with Ni^{2+}-NTA agarose beads (QIAGEN), washed with 3.0 M NaCl and 30 mM imidazole, eluted in a buffer containing 0.2 M imidazole, and dialysed overnight. The protein was then injected onto a Resource-S cation exchange column and eluted at 0.2 M NaCl. GFP-NuMA$^{1821-2115}$ was further polished on a Superdex-200 10/300 Increase column equilibrated in a high salt buffer consisting of 10 mM Hepes (pH 7.5), 2 mM $MgCl_2$, 0.1 mM $CaCl_2$, 4 mM EGTA, 10%

sucrose, 0.5 M KCl salt. Peak fractions were analysed by SDS-PAGE, pooled and concentrated to 6.0 mg/ml (100 μM) prior freezing at -80 °C (figure 3.8b).

MBP-NuMA constructs used for the MBP pulldown assay of figure 2.1b were expressed in BL21 Rosetta *E. coli* cells by 5 hours induction with 0.5 mM IPTG at 20 °C. Cells were lysed in GST/MBP-lysis buffer containing 0.1 M Tris-HCl (pH 8.0), 0.3 M NaCl, 10% glycerol, 0.5 mM EDTA, 1 mM DTT and protease inhibitors, sonicated and cleared. Proteins were affinity purified by incubation with amylose beads (NEB). After washing, proteins immobilized on beads were resuspended in a pulldown buffer containing 10 mM Hepes (pH 7.5), 0.1 M NaCl, 5% glycerol, 0.1% tween-20, 1 mM DTT, and quantified by SDS-PAGE.

Dynein GST-LIC constructs used for the GST pulldown assays were expressed in BL21 Rosetta *E. coli* cells by 16 hours induction with 0.5 mM IPTG at 20 °C. Cells were lysed in GST/MBP-lysis buffer, sonicated and cleared. Proteins were affinity purified by incubation with GSH beads (GE Healthcare). After washing, proteins immobilized on beads were resuspended in a pulldown buffer consisting of 50 mM Tris-HCl (pH 7.4), 0.1 M NaCl, 3 mM DTT, and quantified by SDS-PAGE.

For the SEC experiments of figures 2.7 and 2.10b, His-LIC1$^{390\text{-}523}$ and His-LIC2$^{379\text{-}492}$ were expressed in BL21 Rosetta *E. coli* cells by 16 hours induction with 0.5 mM IPTG at 20 °C. Cells were lysed in His-lysis buffer, sonicated and cleared. Over-expressed proteins were purified by affinity chromatography on HiTrap chelating column loaded with $NiCl_2$, and then dialysed overnight at 4 °C against a buffer containing 30 mM Tris-HCl (pH 6.8), 0.1 M NaCl, 5% glycerol and 1 mM DTT. The proteins were further purified by cation exchange with a Resource-S column by elution with a salt gradient from 0.04 M to 0.7 M NaCl. Peak fractions were pooled and concentrated to 50 mg/ml (3.6 mM, His-LIC1$^{390\text{-}523}$) and 30 mg/ml (2.4 mM, His-LIC2$^{379\text{-}492}$) prior freezing at -80 °C.

For the SEC experiment of figure 2.10c, MBP-LIC1-His was expressed in BL21 Rosetta *E. coli* cells, grown in TB media supplemented with 100 μg/ml kanamycin and 0.2% glucose, by 16 hours induction with 0.25 mM IPTG at 19 °C. Cells were lysed in GST/MBP-lysis buffer, sonicated and cleared. The over-expressed protein was affinity purified by incubation with amylose beads. After washing, the protein was eluted in a buffer containing 10 mM maltose and then further purified by affinity chromatography on HiTrap chelating column loaded with $NiCl_2$, washed, eluted by a 0.025 M – 0.15 M imidazole gradient, and the peak fractions analysed by SDS-PAGE, pooled and concentrated to 40 mg/ml (400 μM) prior freezing at -80 °C.

For the comparative pulldown of figure 2.10d, the pET28a-6xHis-2xStrepTag-GFP-HOOK3$^{1\text{-}552}$ construct (Addgene, #74614) was expressed in BL21 Rosetta *E. coli* cells by 16 hours induction with 0.5 mM IPTG at 20 °C. Cells were lysed in His-lysis buffer and

cleared. The over-expressed protein was purified by affinity chromatography on HiTrap chelating column loaded with $NiCl_2$, washed with 3.0 M NaCl and 15 mM imidazole, eluted at about 0.13 M imidazole, and then dialysed overnight at 4 °C against desalting buffer. The protein was then purified by anion exchange with a Resource-Q column by eluting at 0.27 M NaCl. GFP-Hook3$^{1-552}$ was further polished on a Superose-6 10/300, equilibrated in 50 mM Tris (pH 7.4), 0.1 M NaCl, 3 mM DTT. Peak fractions were analysed by SDS-PAGE, pooled and concentrated prior freezing at -80 °C with the addition of 5% glycerol.

For the binding assays of figures 3.5 and 3.6, GST-53BP1 constructs spanning residues 1-595, 596-1219 and 596-1284 were expressed in BL21 pLysS *E. coli* cells by 5 hours induction with 0.5 mM IPTG at 20 °C, while 53BP1$^{1285-1972}$ and 53BP1$^{1484-1972}$ were expressed in BL21 Rosetta *E. coli* cells with the same protocol of protein induction. Cells were lysed in GST/MBP-lysis buffer, sonicated and cleared. Proteins were affinity purified by incubation with GSH beads. After washing, proteins immobilized on beads were resuspended in a pulldown buffer consisting of 50 mM Hepes (pH 7.5), 0.1 M NaCl, 5 mM $MgCl_2$, 10% glycerol, 1 mM DTT, and quantified by SDS-PAGE.

For the analytical SEC experiment of figure 3.7, 53BP1$^{1484-1972}$ was purified by affinity chromatography on a GST HiTrap column (GE Healthcare), eluted in a buffer containing 20 mM glutathione (pH 8.0) and then dialysed overnight at 4 °C, while incubating with Prescission protease to remove the GST tag. The protein was further purified by ion exchange with a Resource-Q column by elution at 0.17 M NaCl. Peak fractions were pooled and concentrated to 12.5 mg/ml (230 μM) prior freezing at -80 °C.

5.3 Static light scattering (SLS) measurements

SLS analyses of figure 2.2 were performed on a Viscotek GPCmax/TDA instrument equipped with two TSKgel G3000PWxl columns (Tosoh bioscience) in series. The system was calibrated with BSA and equilibrated in a buffer containing 10 mM Tris-HCl (pH 6.8), 0.1 M NaCl, 5% glycerol for NuMA$^{1-153}$, and in a buffer containing 10 mM Hepes (pH 7.5), 0.1 M NaCl, 5% glycerol for NuMA$^{1-705}$ and NuMA$^{154-705}$. 75 μl of purified samples concentrated at about 2 mg/ml were loaded on the columns.

5.4 Crystallization and structure determination

The purified NuMA$^{1-153}$ construct was screened for crystallization using commercially available kits. Crystallization experiments were initially conducted in 200 nl vapor diffusion sitting drops using a mosquito Crystal nano dispenser (TTP Labtech) in MRC-2 well plates (Swissci, Hampton research). Crystals were obtained using the Hampton Research Crystal

Screen 1 and 2 at 4 °C, at 16.5 mg/ml protein concentration, with a reservoir containing 30% PEG-4000, 0.2 M $MgCl_2$, and 0.1 M Tris-HCl (pH 8.5). Diffraction-quality crystals were achieved by optimization using the hanging drop method in 24-well VDX plates. The best crystals grew in crystallization drops consisting of a 1:1 (v/v) mixture of protein solution and well solution of 27% PEG-4000, 0.2 M $MgCl_2$, 0.1 M Bis-Tris Propane (pH 8.5). Crystals were further improved through streak-seeding and by additive screening. For data collection, crystals were transferred to a cryo-buffer (reservoir buffer supplemented with 15% glycerol) and flash-frozen in liquid nitrogen. X-ray diffraction data were collected to 1.54 Å resolution at the PXIII beamline X06DA of the Swiss Light Source (Villigen). All data were initially processed with XDS [140] implemented in xia2 [141] to define the crystallographic space group, unit cell and data collection statistics. The structure of $NuMA^{1-153}$ was determined by SAD method on Se-Met containing crystals, which were grown similarly to the native ones. Initial phases were derived using the *AutoSol* Wizard [142] in *Phenix* [143]. The unit-cell parameters are consistent with four copies of the protein per asymmetric unit. Initial model building was conducted by *AutoBuild* Wizard [144] in *Phenix* and completed using iterative cycles of manual model building in *Coot* [145] and refinement in *Phenix*. The model was refined to an R_{free} of 21.5% and an R_{work} of 17.0%.

PyMOL was used to generate all the illustrations of the structure (http://www.pymol.org). Structure superposition of $NuMA^{1-153}$ to the hook domain of Hook3 (PDB ID: 6B9H) was based on the largest rigid body calculated using the RAPIDO algorithm (http://webapps.embl-hamburg.de/rapido/).

Atomic coordinates and structure factor amplitudes for the crystal structure of $NuMA^{1-153}$ are deposited in the PDB under the accession code 6QJA.

5.5 Cell culture

HEK293T (female), MC38 (female) and HeLa (female) cells were cultured at 37 °C in a 5% CO_2 atmosphere, in Dulbecco's Modified Eagle Medium (DMEM) supplemented with 10% fetal bovine serum (FBS), 1% L-glutamine, and 50 µg/ml penicillin/streptomycin.

For the KD of NuMA, shRNA was used to target gene expression via RNA interference. A lentiviral vector carrying a GFP reporter and puromycin resistance, and expressing the NuMA shRNA CAUUAUGAUGCCAAGAAGCAGCAGA ACCA, was used to generate stably interfered HeLa cell lines [58]. For HeLa cells expressing the shRNA targeting NuMA, the medium was supplemented with 0.5 µg/ml puromycin. Before the immunofluorescence experiments of figures 2.11c and 2.12a, to assess integrin-mediated division orientation,

HeLa cells were plated on coverslips precoated with fibronectin (5 μg/ml, Roche) for 2 hours.

5.5.1 Synchronization, cell treatments and transfection

For pulldown and immunoprecipitation experiments of figures 2.1b, 2.9f, 3.4, 3.5b, and 3.6b, HEK293T and HeLa cells were treated with nocodazole (0.33 μM, Sigma #M1404) for 16 hours, to enrich the population of prometaphase cells, and then collected (figure 5.1a). Nocodazole is an antimitotic agent that arrests the cell cycle at the G2/M phase. It inhibits MT dynamics by binding to β-tubulin and by interfering with MT polymerization.

24h before nocodazole treatment, HEK293T cells of pulldown experiment of figure 3.6b, at 70% of confluence, were transiently transfected with pCDH-Ubc vectors expressing GFP-tagged NuMA full-length, $NuMA^{1-705}$, $NuMA^{705-1821}$, or $NuMA^{1821-2115}$ using calcium phosphate method (figure 5.1b).

NuMA depleted HeLa cells of immunofluorescence experiments of figures 2.11c and 2.12a were transiently transfected with pCDH-Ubc vectors expressing mCherry-tagged NuMA full-length, $NuMA^{\Delta 1-153}$, $NuMA^{\Delta 154-705}$, $NuMA^{\Delta 1-705}$, or $NuMA^{A368V/A369V}$ using Lipofectamine 3000 (Invitrogen) according to manufacturer's instructions. Transfected cells were treated with thymidine (2.5 mM, Sigma #89270) for 24 hours, and then fixed 8 hours after the release (figure 5.1c). Thymidine is a DNA synthesis inhibitor that arrests cells at G1/S boundary. After release into normal medium, cell population at distinct cell cycle phase can be collected at different time points. In this case after 8 hours there is an enrichment of mitotic cells.

To induce the DNA damage, HEK293T cells of figure 3.3b were treated with 0.2 μM of doxorubicin or with the same volume of DMSO as negative control for 12 hours, and then collected (figure 5.1d). Doxorubicin is a drug that damages DNA through intercalation or direct alkylation, causing the formation of DNA DSBs.

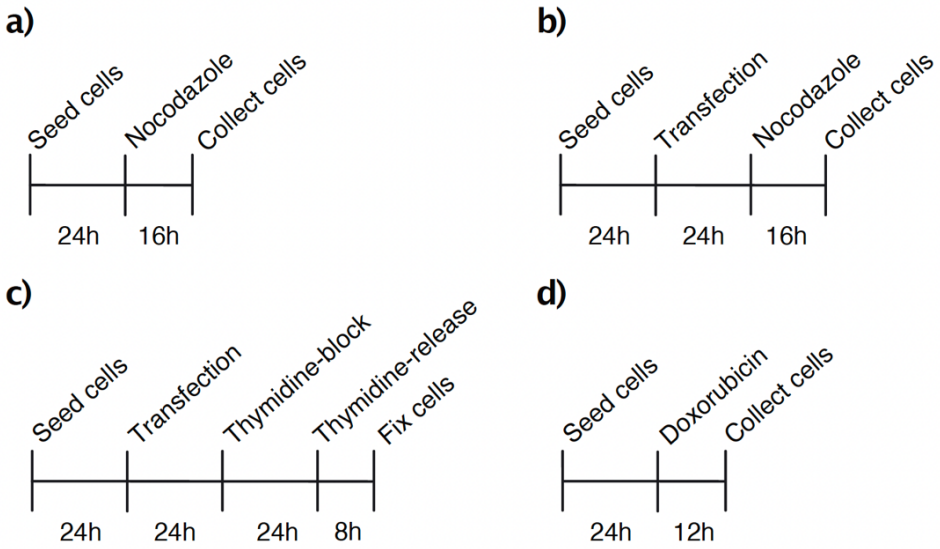

Figure 5.1 – Synchronization, cell treatments and transfection protocols

a) *Synchronization protocol of figures 2.1b, 2.9f, 3.3f and 3.5b.* ***b)*** *Synchronization protocol of figure 3.6b.* ***c)*** *Single thymidine block of figures 2.11c and 2.12a.* ***d)*** *Drug treatment of figure 3.3b.*

5.5.2 Nuclear fractionation

Two types of nuclear fractionation experiments were performed, described in detail in the results section (paragraphs 3.1 and 3.2). In the first fractionation experiment of figure 3.1a, I divided the cytoplasmic and nuclear compartments, extracting the cytosol with a hypotonic buffer containing 0.1 M NaCl. The nucleus was then further divided in the soluble nucleosol and in the chromatin and insoluble nuclear matrix fraction, the first obtained in a buffer at high concentration of salt (0.3 M), and the second extracted in a buffer containing high concentration of urea (8 M). In the second fractionation experiment of figure 3.2a, after extracting the cytosol, the nuclear pellet was resuspended in a buffer containing 0.15 M NaCl, 0.5% NP40 and the Benzonase nuclease (Millipore, #E1014), this latter required for the digestion of DNA and the release of nuclear proteins strongly associated with DNA. Cytosolic and nuclear fractions were quantified by Bradford assay (Bio-Rad) before immunoblotting.

5.6 *In vitro* binding assays

5.6.1 Analytical size-exclusion chromatography (SEC)

For SEC analyses of figure 2.7, NuMA$^{1\text{-}153}$ (1.0 mM) was mixed and incubated for 1 hour on ice with His-LIC1$^{390\text{-}523}$ (1.0 mM) or His-LIC2$^{379\text{-}492}$ (0.5 mM), and loaded on a Superdex-

75 Increase 10/300 column (GE Healthcare) equilibrated in 10 mM Hepes (pH 7.5), 50 mM NaCl, 5% glycerol.

For the SEC analysis of figure 2.10b, 0.27 mM of NuMA$^{1-705}$ were mixed with 1.0 mM of His-LIC1$^{390-523}$, incubated 1 hour on ice, injected on a Superose-6 10/300 column (GE Healthcare) equilibrated in 10 mM Hepes (pH 7.5), 0.1 M NaCl, 5% glycerol, 1 mM DTT, and eluted in 300 µl fractions. In figure 2.10c, NuMA$^{1-705}$ (0.15 mM) was incubated with MBP-LIC1-His (0.2 mM) and loaded on the same equilibrated column.

For the SEC analysis of figure 3.7, 90 µM of 53BP1$^{1484-1972}$ were incubated for 1 hour on ice with 90 µM of His-NuMA$^{1821-2115}$ and loaded on a Superose-6 Increase 3.2/300 column (GE Healthcare) equilibrated in 10 mM Tris (pH 8.0), 0.1 M NaCl, 5% glycerol, 1 mM DTT.

Eluted species were monitored by absorbance at 280 nm and subsequently checked by SDS-PAGE followed by Coomassie staining.

5.6.2 Isothermal titration calorimetry (ITC)

An ITC experiment was performed to measure the thermodynamical parameters of the association between 0.4 mM of purified NuMA$^{1-414}$ construct and 5 mM of LIC1 peptide (residues 433-458). LIC1 peptide (united biosystems) was dissolved in water. Before ITC, NuMA and LIC1 were dialysed in a buffer containing 5 mM Hepes (pH 7.5) and 50 mM NaCl.

5.6.3 MBP pulldown

The pulldown assay with mitotic lysates of figure 2.1b was performed with human HEK293T cells treated with 0.33 mM nocodazole for 16 hours before harvesting. Cells were lysed in a buffer containing 50 mM Hepes (pH 7.5), 0.15 M NaCl, 5 mM EDTA, 1.5 mM $MgCl_2$, 1 mM DTT, 10% glycerol, 1% triton X-100, protease inhibitors, and phosphatase inhibitors (PhosSTOP tablet, Roche), and cleared by centrifugation. About 2 mg of extracts were incubated with 5 µM of MBP-NuMA constructs (MBP-NuMA$^{1-705}$, MBP-NuMA$^{1-400}$, MBP-NuMA$^{1-260}$, and MBP-NuMA$^{1-153}$), immobilized on amylose beads, for two hours at 4 °C, on a rocking wheel, in a final volume of 400 µl. Beads were washed four times with 1 ml of lysis buffer (20 seconds of spin between washes), and species retained on beads were analysed by SDS-PAGE and immunoblotted for the anti-dynactin p150^{Glued} and anti-dynein IC antibodies (see table 5.2).

5.6.4 GST pulldown

To test the binding of NuMA$^{1-705}$ to LIC1 and LIC2 constructs, 0.8 μM of GST-LIC constructs (GST-LIC1$^{1-523}$, GST-LIC1$^{390-523}$, GST-LIC2$^{1-492}$, GST-LIC2$^{379-492}$, GST-LIC1$^{1-523}$-F447A/F448A), immobilized on GSH beads, were incubated for 1 hour on ice with 7 μM of purified His-NuMA$^{1-705}$ WT or carrying the point mutations R114A, W116A, Y121A, Q124A, L131A, L135A, or A368V/A369V (figures 2.3b, 2.6d-f, and 2.9a-c). Pulldown assays were conducted in 100 μl volume of pulldown buffer composed of 50 mM Tris-HCl (pH 7.4), 0.1 M NaCl, 3 mM DTT, 0.1% tween-20, 0.1% triton X-100, and 0.07% Na-deoxycholate. After three washes with 100 μl of pulldown buffer (20 seconds of spin between washes), proteins bound to beads were separated by SDS-PAGE and then transferred onto a nitrocellulose membrane for an hour and a half at 100 V for immunoblotting with anti-His antibody (table 5.2).

To compare NuMA$^{1-705}$ and Hook3$^{1-552}$ capability to bind LIC1, 0.8 μM of GST-LIC1$^{1-523}$, immobilized on GSH beads, were incubated with 1, 3 or 7 μM of His-NuMA$^{1-705}$ or GFP-Hook3$^{1-552}$, and the pulldown was performed similarly to what described above. After washes, species retained on beads were analysed by SDS-PAGE and visualized by Coomassie staining (figure 2.10d).

The pulldown assay with mitotic lysates of figure 2.9f was performed with murine MC38 and human HEK293T cells treated with 0.33 μM nocodazole for 16 hours before harvesting. Cells were lysed by sonication in a buffer containing 50 mM Hepes (pH 7.5), 50 mM NaCl, 1.5 mM EDTA, 1.5 mM $MgCl_2$, 1 mM DTT, 10% glycerol, 0.01% tween-20, protease inhibitors, and phosphatase inhibitors, and cleared by centrifugation. 1 mg of extracts at about 10 mg/ml for MC38 cells and 5 mg/ml for HEK293T cells was incubated with 2 μM GST-LIC1$^{1-523}$ immobilized on GSH beads for 2 hours at 4 °C, with gentle rotation on the wheel. Beads were washed three times with 0.5 ml lysis buffer, and species retained on beads were analysed by SDS-PAGE and immunoblotted with anti-NuMA mouse antibody (table 5.2).

The pulldown assay with mitotic lysates of figure 3.5b was performed using HeLa cells treated with 0.33 μM nocodazole for 16 hours before harvesting. Cells were lysed in a pulldown buffer containing 50 mM Hepes (pH 7.5), 0.1 M NaCl, 5 mM $MgCl_2$, 1 mM DTT, 10% glycerol, 0.1% NP40, 0.1% tween-20, protease inhibitors and phosphatase inhibitors, and cleared by centrifugation. 1 mg of extract at about 5 mg/ml was incubated with 2 μM of GST-53BP1 constructs immobilized on GSH beads for 2 hours at 4 °C on a rotating wheel, in 0.4 mL of pulldown buffer. Beads were washed three times with 0.4 ml pulldown buffer (20 seconds of spin between washes), and species retained on beads were analysed by SDS-

PAGE and immunoblotted with anti-NuMA antibody. Bait proteins were obtained from 0.2 mL of cell culture, incubated with 0.2 mL of GSH beads and washed extensively before being quantified by SDS-PAGE and Coomassie staining.

The GST-pulldown with nuclear lysates of figure 3.5c was essentially performed as for figure 3.5b but with HeLa nucleoplasmic fractions obtained as explained in paragraph 3.1. The experiment was performed in 0.35 ml volume of 20 mM Tris (pH 8.0), 0.15 M NaCl, 10% glycerol, 1 mM DTT, 0.1% NP40, with 1 mg of nuclear lysate at about 5 mg/ml and 2 μM of bait proteins.

The GST-pulldown of figure 3.6b was performed with GST-53BP1$^{1285-1972}$ and HEK293T cells transfected with GFP-NuMA constructs and treated with nocodazole. Cells were transfected with different amounts of GFP-NuMA domains to have the same band intensity on western blot (10 μg GFP-NuMA Fl, 0.3 μg GFP-NuMA$^{1-705}$, 0.3 μg GFP-NuMA$^{705-1821}$, and 0.5 μg GFP-NuMA$^{1821-2115}$). Cells were lysed in 50 mM Hepes (pH 7.5), 1.5 mM EGTA, 1.5 mM $MgCl_2$, 0.1 M NaCl, 0.1% NP40, 10% glycerol, protease inhibitors, and 1 mM DTT, and the pulldown was performed with 1 mg of lysates at about 6 mg/ml and with 1 μM of bait proteins. Species retained on beads were analysed by SDS-PAGE and immunoblotted for the anti-GFP antibody (table 5.2).

5.6.5 Co-immunoprecipitation (co-IP)

The IP experiments of figures 3.2c and 3.3b were performed with 500 μg of nuclear lysates (obtained as for figure 3.2b) at 5 mg/ml, in 100 μl final volume of IP buffer containing 10 mM Tris-HCl (pH 7.6), 0.15 M NaCl, 0.2% NP40, 1 mM DTT. The lysates were incubated for 2 hours on ice with 10 μg of anti-NuMA antibody suitable for IP (table 5.1) or IgG (Sigma, #I8765) as negative control, and then for other 2 hours with 10 μl dry protein-G (Invitrogen). Three washing steps of 20 seconds were performed in 100 μl of IP washing buffer consisting of 10 mM Tris-HCl (pH 7.6), 0.25 M NaCl, 0.2% NP40, 1 mM DTT. Proteins retained on beads were separated by SDS-PAGE and then the resulting blots were probed for the rabbit anti-NuMA, anti-53BP1, anti-TPX2, and anti-H3 antibodies (table 5.2). Before IP, protein-G were washed 3 times with 0.5% BSA, let 2 hours on the wheel to preblock with the same buffer, and then equilibrated in IP buffer. The IP experiment of figure 3.3f was performed as above with 500 μg of mitotic lysates at 5 mg/ml, in a buffer consisting of 50 mM Hepes (pH 7.5), 2 mM EGTA, 1 mM EDTA, 2 mM $MgCl_2$, 0.1 M KCl, 10% glycerol, 0.1% NP40, 1 mM DTT.

5.7 Sequence alignment

For figures 2.6a and 2.8a, *Homo sapiens* sequences of NuMA (Uniprot entry Q14980), Hook1 (Uniprot entry Q9UJC3), Hook2 (Uniprot entry Q96ED9), and Hook3 (Uniprot entry Q86VS8) were aligned with NuMA sequences from *Mus musculus* (Uniprot entry E9Q7G0), *Gallus gallus* (Uniprot entry D8MIU8), *Xenopus laevis* (Uniprot entry P70012), *Danio rerio* (NCBI entry XP_009290241.1), *Drosophila melanogaster* (Uniprot entry Q8IR55), Hook1 sequences from *Mus musculus* (Uniprot entry Q8BIL5), *Gallus gallus* (Uniprot entry Q5ZJ27), *Xenopus tropicalis* (Uniprot entry F7CDF9), *Danio rerio* (Uniprot entry Q5TZ80), Hook2 sequences from *Mus musculus* (Uniprot entry Q7TMK6), *Gallus gallus* (Uniprot entry XP_025001539.1), *Xenopus laevis* (Uniprot entry Q6NRB0), *Danio rerio* (NCBI entry NP_957405.1), Hook3 sequences from *Mus musculus* (Uniprot entry Q8BUK6), *Gallus gallus* (Uniprot entry F1NKH3), *Xenopus laevis* (Uniprot entry Q6GQ73), *Danio rerio* (NCBI entry XP_017211697.1), and with the *Drosophila melanogaster* Hook sequence (Uniprot entry Q24185) using CLUSTAL Ω. The multiple sequence alignment was visualized and coloured with Jalview by percentage of identity for figure 2.6a and by Clustalx for figure 2.8a.

For figure 2.8a, NuMA sequences from *Homo sapiens* (Uniprot entry Q14980), *Mus musculus* (Uniprot entry E9Q7G0), *Gallus gallus* (Uniprot entry D8MIU8), *Xenopus laevis* (Uniprot entry P70012) and *Danio rerio* (NCBI entry XP_009290241.1) were aligned with CLUSTALΩ and coloured by Clustalx in Jalview. To identify the CC1-box-like motif, the first 720 residues of NuMA sequences were aligned with 120 residues around the CC1-boxes of known dynein adaptors using the *Homo sapiens* sequences of BICD2 (Uniprot entry Q8TD16), BICDR1 (Uniprot entry Q6ZP65), SPDL1 (Uniprot entry Q96EA4), BICD1 (Uniprot entry Q96G01), HAP1 (Uniprot entry P54257), and TRAK1 (Uniprot entry Q9UPV9). The alignment was further edited according to the paper by Sacristan *et al.* [146].

5.8 *In vitro* droplet assay, imaging and statistical analysis

For the phase-separation assay of figure 3.8c, GFP-NuMA$^{1821-2115}$ purified in a high salt buffer consisting of 10 mM Hepes (pH 7.5), 2 mM $MgCl_2$, 0.1 mM $CaCl_2$, 4 mM EGTA, 10% sucrose, 0.5 M KCl, at 6 mg/ml (100 μM) was diluted 1:5 in the same buffer containing no salt to reach a final KCl salt concentration of 0.1 M and a protein concentration of 20 μM. The reaction mixture was immediately pipetted into a 20 μl volume coverslip flow chamber. The slide was placed coverslip-side down into a humidity chamber for 20 minutes at room temperature, to allow condensates to settle; reaction was then imaged at Leica DM6 Multifluo Fluorescence Microscope using the filter for GFP and DIC at 100X magnification.

In figure 3.9a a phase diagram was performed testing the ability of purified GFP-NuMA$^{1821-2115}$ to form condensates *in vitro* at different salt and protein concentrations at the Spinning disk confocal microscope Nikon CSU-W1, using laser 488, a 100X oil-immersion objective lens, and a 384-well microplate (Greiner). In the experiment of figure 3.9b 10% of 1,6-hexanediol (Sigma) and 12.5 mM of ATP (Sigma) were added to the reaction mixtures. Crowding agents were never used. All images were processed using the software Fiji [147].
Statistical analysis of the data was performed in Prism with the one-way ANOVA Tukey's multiple comparisons test. In figure 3.9c-d, data are presented as mean ± SEM, with the exact p-values indicated in the figure legend.

5.9 Immunoblotting

Proteins separated by SDS-PAGE were transferred onto a nitrocellulose membrane for 1 hour and a half at 100 V for immunoblotting. Proteins at about 250 kDa, like NuMA and 53BP1, were transferred for 3 hours at 100 V in a buffer containing 6% MetOH and 0.02% SDS. Membranes were blocked with 5% milk solution in TBS and 0.1% tween-20 for 1 hour and incubated with primary antibodies (table 5.2) at room temperature for 2 hours or overnight at 4 °C. After three washes with TBS containing 0.5% tween-20, membranes were incubated with secondary antibodies for 45 minutes and, after three further washes, were acquired using the enhanced chemiluminescence (ECL) and the Chemidoc instrument and Image Lab software (Bio-Rad).
Densitometric analyses of bands in western blots were carried out using Image Lab. For each band equally sized boxes were drawn, the signal intensities were integrated, and background was subtracted. Statistical analysis of the data was performed using GraphPad Prism.

Table 5.2 – Primary antibodies list

Name	Description	Application
α-53BP1, Novus Biologicals, NB100-304	polyclonal, rabbit	1:5000 (IB)
α-dynactin p150^{Glued}, BD Transduction Laboratories, 610473	monoclonal, mouse	1:4000 (IB)
α-dynein IC, Millipore, 2724445	monoclonal, mouse	1:300 (IB)
α-GFP, Roche 11814460001	monoclonal, mouse	1:2000 (IB)
α-α-tubulin, Sigma-Aldrich, T5168	monoclonal, mouse	1:200 (IF), (IB)
α-α-tubulin, Abcam, ab4074	polyclonal, rabbit	1:2000 (IB)
α-γ-tubulin, Abcam, ab11316	monoclonal, mouse	1:100 (IF)
α-H3, CST, 4499	monoclonal, rabbit	1:1000 (IB)
α-His, Santa Cruz Biotechnology, sc8036	monoclonal, mouse	1:200 (IB)
α-lamin B1, Abcam, ab16048	polyclonal, rabbit	1:1000 (IB)
α-NuMA, generated in house, antigen 1861-2001	monoclonal, mouse	1:200 (IB), 1:3000 (IF)
α-NuMA, generated in the lab at GeneCust clone ID: A1A1, antigen 1-705	monoclonal, mouse	5 μg/250 μg lysate (IP)
α-NuMA, Abcam, ab109262	monoclonal, rabbit	1:5000 (IB)

α-phospho-KAP1 (S824), Bethyl Laboratories, A300-767A	polyclonal, rabbit	1:5000, (IB)
α-TPX2, NB500-179	polyclonal, rabbit	1:500 (IB)

5.10 Immunofluorescence, confocal imaging and statistical analysis

For the immunofluorescences of figures 2.11c and 2.12a, HeLa cells were plated on 13 mm coverslips coated with 5 μg/ml fibronectin. To detect α-tubulin or γ-tubulin, cells were fixed with 4% paraformaldehyde for 10 minutes at room temperature, followed by permeabilization with 0.3% triton X-100 in PBS for 5 minutes. Blocking was performed with 3% BSA in PBS for 1 hour at room temperature. Cells were stained with anti-α-tubulin or anti-γ-tubulin in 3% BSA and 0.05% tween-20, followed by incubation with anti-mouse Alexa Fluor 488. DNA was stained with DAPI.

Confocal images were acquired on a Leica SP8 confocal microscope controlled by Leica confocal software. For HeLa cells analysis, a 63X oil-immersion objective lens (HC PL APO 63X/1.40 OIL CS2) was used. All images were processed using the software Fiji [147].

To measure the percentage of multipolar spindle (figure 2.11d), for each condition the number of multipolar spindles was counted for three independent experiments. For statistical analysis, the Fisher's exact test was performed.

Mitotic spindle orientation was monitored on HeLa cells plated on fibronectin-coated coverslips and stained with γ-tubulin to visualize poles and DAPI to visualize the metaphase plate. Cells were imaged in x-z optical sections. To determine the orientation of metaphase spindle, the angle formed by a line passing through the spindle poles and the substratum was measured exploiting the angle tool of the software Fiji. Statistical analysis of the data was performed in Prism with the Kruskal-Wallis test. In figure 2.11d data are presented as mean ± SEM, as indicated in the figure legend.

6. REFERENCES

1. Renna, C., Rizzelli, F., Carminati, M., Gaddoni, C., Pirovano, L., Cecatiello, V., Pasqualato, S., and Mapelli, M. (2020). Organizational Principles of the NuMA-Dynein Interaction Interface and Implications for Mitotic Spindle Functions. Structure *28*, 820–829.e6.
2. Moreno, N.S., Liu, J., Haas, K.M., Parker, L.L., Chakraborty, C., Kron, S.J., Hodges, K., Miller, L.D., Langefeld, C., Robinson, P.J., et al. (2019). The nuclear structural protein NuMA is a negative regulator of 53BP1 in DNA double-strand break repair. Nucleic Acids Res. *47*, 2703–2715.
3. B. Alberts, A. Johnson, J. Lewis, D. Morgan, M. Raff, K. Roberts, P.W. (2015). Molecular Biology of THE CELL Sixth Edition.
4. McGranahan, N., Burrell, R.A., Endesfelder, D., Novelli, M.R., and Swanton, C. (2012). Cancer chromosomal instability: Therapeutic and diagnostic challenges. EMBO Rep. *13*, 528–538.
5. Hoffmann, I. (2021). Centrosomes in mitotic spindle assembly and orientation. Curr. Opin. Struct. Biol. *66*, 193–198.
6. Prosser, S.L., and Pelletier, L. (2017). Mitotic spindle assembly in animal cells: A fine balancing act. Nat. Rev. Mol. Cell Biol. *18*, 187–201.
7. Ong, J.Y., Bradley, M.C., and Torres, J.Z. (2020). Phospho-regulation of mitotic spindle assembly. Cytoskeleton *77*, 558–578.
8. Cavazza, T., and Vernos, I. (2016). The RanGTP pathway: From nucleo-cytoplasmic transport to spindle assembly and beyond. Front. Cell Dev. Biol. *3*.
9. Tsuchiya, K., Hayashi, H., Nishina, M., Okumura, M., Sato, Y., Kanemaki, M.T., Goshima, G., and Kiyomitsu, T. (2021). Ran-GTP Is Non-essential to Activate NuMA for Mitotic Spindle-Pole Focusing but Dynamically Polarizes HURP Near Chromosomes. Curr. Biol. *31*, 115–127.e3.
10. Sawin, K.E., Leguellect, K., Philippet, M., and Mitchison, T.J. (1992). Mitotic spindle organization by a plus-end-directed microtubule motor. Nature *359*, 540–543.
11. Thomas U. Mayer, Tarun M. Kapoor, Stephen J. Haggarty, Randall W. King, Stuart L. Schreiber, T.J.M. (1999). Small molecule inhibitor of mitotic spindle bipolarity identified in a phenotype-based screen. Science (80-.).
12. She, Z., and Yang, W. (2017). Molecular mechanisms of kinesin-14 motors in spindle assembly and chromosome segregation. J. Cell Sci., 2097–2110.
13. Zhong, A., Tan, F.Q., and Yang, W.X. (2016). Chromokinesin: Kinesin superfamily regulating cell division through chromosome and spindle. Gene *589*, 43–48.
14. Merdes, A., Ramyar, K., Vechio, J.D., and Cleveland, D.W. (1996). A complex of NuMA and cytoplasmic dynein is essential for mitotic spindle assembly. Cell *87*, 447–458.
15. Silk, A.D., Holland, A.J., and Cleveland, D.W. (2009). Requirements for NuMA in maintenance and establishment of mammalian spindle poles. J. Cell Biol. *184*, 677–690.
16. Raaijmakers, J.A., and Medema, R.H. (2014). Function and regulation of dynein in

mitotic chromosome segregation. Chromosoma *123*, 407–422.

17. Dwivedi, D., Kumari, A., Rathi, S., Mylavarapu, S.V.S., and Sharma, M. (2019). The dynein adaptor Hook2 plays essential roles in mitotic progression and cytokinesis. J. Cell Biol. *218*, 3526–3527.

18. Hanafusa, H., Kedashiro, S., Tezuka, M., Funatsu, M., Usami, S., Toyoshima, F., and Matsumoto, K. (2015). PLK1-dependent activation of LRRK1 regulates spindle orientation by phosphorylating CDK5RAP2. Nat. Cell Biol. *17*, 1024–1035.

19. Pietro, F., Echard, A., and Morin, X. (2016). Regulation of mitotic spindle orientation: an integrated view. EMBO Rep. *17*, 1106–1130.

20. Lechler, T., and Mapelli, M. (2021). Spindle positioning and its impact on vertebrate tissue architecture and cell fate. Nat. Rev. Mol. Cell Biol. *0123456789*, 1–18.

21. Bergstralh, D.T., Haack, T., and St Johnston, D. (2013). Epithelial polarity and spindle orientation: Intersecting pathways. Philos. Trans. R. Soc. B Biol. Sci. *368*.

22. Morin, X., and Bellaïche, Y. (2011). Mitotic Spindle Orientation in Asymmetric and Symmetric Cell Divisions during Animal Development. Dev. Cell *21*, 102–119.

23. Lechler, T., and Fuchs, E. (2005). Asymmetric cell divisions promote stratification and differentiation of mammalian skin. Nature *437*, 275–280.

24. Caussinus, E., and Gonzalez, C. (2005). Induction of tumor growth by altered stem-cell asymmetric division in Drosophila melanogaster. Nat. Genet. *37*, 1125–1129.

25. Knoblich, J.A. (2010). Asymmetric cell division: Recent developments and their implications for tumour biology. Nat. Rev. Mol. Cell Biol. *11*, 849–860.

26. Lough, K.J., Byrd, K.M., Descovich, C.P., Spitzer, D.C., Bergman, A.J., Beaudoin, G.M., Reichardt, L.F., and Williams, S.E. (2019). Telophase correction refines division orientation in stratified epithelia. Elife *8*, 1–32.

27. Nakajima, Y.I., Meyer, E.J., Kroesen, A., McKinney, S.A., and Gibson, M.C. (2013). Epithelial junctions maintain tissue architecture by directing planar spindle orientation. Nature *500*, 359–362.

28. Bergstralh, D.T., Lovegrove, H.E., and St. Johnston, D. (2015). Lateral adhesion drives reintegration of misplaced cells into epithelial monolayers. Nat. Cell Biol. *17*, 1497–1503.

29. Cammarota, C., Finegan, T.M., Wilson, T.J., Yang, S., and Bergstralh, D.T. (2020). An Axon-Pathfinding Mechanism Preserves Epithelial Tissue Integrity. Curr. Biol. *30*, 5049–5057.e3.

30. Matsumura, S., Kojidani, T., Kamioka, Y., Uchida, S., Haraguchi, T., Kimura, A., and Toyoshima, F. (2016). Interphase adhesion geometry is transmitted to an internal regulator for spindle orientation via caveolin-1. Nat. Commun. *7*.

31. Du, Q., and Macara, I.G. (2004). Mammalian Pins is a conformational switch that links NuMA to heterotrimeric G proteins. Cell *119*, 503–516.

32. Kotak, S., Busso, C., and Gönczy, P. (2012). Cortical dynein is critical for proper spindle positioning in human cells. J. Cell Biol. *199*, 97–110.

33. Singh, D., Schmidt, N., Müller, F., Bange, T., and Bird, A.W. (2021). Destabilization of long astral microtubules via Cdk1-dependent removal of GTSE1 from their plus ends facilitates prometaphase spindle orientation. Curr. Biol. *31*, 766–781.e8.

34. Pan, Z., Zhu, J., Shang, Y., Wei, Z., Jia, M., Xia, C., Wen, W., Wang, W., and Zhang, M. (2013). An autoinhibited conformation of LGN reveals a distinct interaction mode between GoLoco motifs and TPR motifs. Structure *21*, 1007–1017.

35. Zhu, J., Wen, W., Zheng, Z., Shang, Y., Wei, Z., Xiao, Z., Pan, Z., Du, Q., Wang, W., and Zhang, M. (2011). LGN/mInsc and LGN/NuMA Complex Structures Suggest Distinct Functions in Asymmetric Cell Division for the Par3/mInsc/LGN and Gαi/LGN/NuMA Pathways. Mol. Cell *43*, 418–431.

36. Pirovano, L., Culurgioni, S., Carminati, M., Alfieri, A., Monzani, S., Cecatiello, V., Gaddoni, C., Rizzelli, F., Foadi, J., Pasqualato, S., et al. (2019). Hexameric NuMA:LGN structures promote multivalent interactions required for planar epithelial divisions. Nat. Commun. *10*.

37. Seldin, L., Poulson, N.D., Foote, H.P., and Lechler, T. (2013). NuMA localization, stability, and function in spindle orientation involve 4.1 and Cdk1 interactions. Mol. Biol. Cell *24*, 3651–3662.

38. Machicoane, M., de Frutos, C.A., Fink, J., Rocancourt, M., Lombardi, Y., Gare, S., Piel, M., and Echard, A. (2014). SLK-dependent activation of ERMs controls LGN-NuMA localization and spindle orientation. J. Cell Biol. *205*, 791–799.

39. Carminati, M., Gallini, S., Pirovano, L., Alfieri, A., Bisi, S., and Mapelli, M. (2016). Concomitant binding of Afadin to LGN and F-actin directs planar spindle orientation. Nat. Struct. Mol. Biol. *23*, 155–163.

40. Gloerich, M., Bianchini, J.M., Siemers, K.A., Cohen, D.J., and Nelson, W.J. (2017). Cell division orientation is coupled to cell-cell adhesion by the E-cadherin/LGN complex. Nat. Commun. *8*, 1–11.

41. Culurgioni, S., Alfieri, A., Pendolino, V., Laddomada, F., and Mapelli, M. (2011). Inscuteable and NuMA proteins bind competitively to Leu-Gly-Asn repeat-enriched protein (LGN) during asymmetric cell divisions. Proc. Natl. Acad. Sci. U. S. A. *108*, 20998–21003.

42. Culurgioni, S., Mari, S., Bonetti, P., Gallini, S., Bonetto, G., Brennich, M., Round, A., Nicassio, F., and Mapelli, M. (2018). Insc:LGN tetramers promote asymmetric divisions of mammary stem cells. Nat. Commun. *9*.

43. Lydersen, B.K., and Pettijohn, D.E. (1980). Human-specific nuclear protein that associates with the polar region of the mitotic apparatus: Distribution in a human/hamster hybrid cell. Cell *22*, 489–499.

44. Compton, D.A., Szilak, I., and Cleveland, D.W. (1992). Primary structure of NuMA, an intranuclear protein that defines a novel pathway for segregation of proteins at mitosis. J. Cell Biol. *116*, 1395–1408.

45. Seldin, L., Muroyama, A., and Lechler, T. (2016). NuMA-microtubule interactions are critical for spindle orientation and the morphogenesis of diverse epidermal structures. Elife *5*, 1–18.

46. Williams, S.E., Beronja, S., Pasolli, H.A., and Fuchs, E. (2011). Asymmetric cell divisions promote Notch-dependent epidermal differentiation. Nature *470*, 353–358.

47. Chinen, T., Yamamoto, S., Takeda, Y., Watanabe, K., Kuroki, K., Hashimoto, K., Takao, D., and Kitagawa, D. (2020). NuMA assemblies organize microtubule asters to establish spindle bipolarity in acentrosomal human cells. EMBO J. *39*, 1–18.

48. Quintyne, N.J., Reing, J.E., Hoffelder, D.R., Gollin, S.M., and Saunders, W.S. (2005). Spindle multipolarity is prevented by centrosomal clustering. Science (80-.). *307*, 127–129.

49. Brüning-Richardson, A., Bond, J., Alsiary, R., Richardson, J., Cairns, D.A., McCormac, L., Hutson, R., Burns, P.A., Wilkinson, N., Hall, G.D., et al. (2012). NuMA overexpression in epithelial ovarian cancer. PLoS One *7*, 1–11.

50. Novatchkova, M., and Eisenhaber, F. (2002). A CH domain-containing N terminus in NuMA? Protein Sci. *11*, 2281–2284.

51. Yang, C.H., Lambie, E.J., and Snyder, M. (1992). NuMA: An unusually long coiled-coil related protein in the mammalian nucleus. J. Cell Biol. *116*, 1303–1317.

52. Chang, C.C., Huang, T.L., Shimamoto, Y., Tsai, S.Y., and Hsia, K.C. (2017). Regulation of mitotic spindle assembly factor NuMA by Importin-β. J. Cell Biol. *216*, 3453–3462.

53. Okumura, M., Natsume, T., Kanemaki, M.T., and Kiyomitsu, T. (2018). Dynein–dynactin–NuMA clusters generate cortical spindle-pulling forces as a multiarm ensemble. Elife *7*, 1–24.

54. Harborth, J., Weber, K., and Osborn, M. (1995). Epitope mapping and direct visualization of the parallel, in-register arrangement of the double-stranded coiled-coil in the NuMA protein. EMBO J. *14*, 2447–2460.

55. Forth, S., Hsia, K.C., Shimamoto, Y., and Kapoor, T.M. (2014). Asymmetric friction of nonmotor MAPs can lead to their directional motion in active microtubule networks. Cell *157*, 420–432.

56. Serra-Marques, A., Houtekamer, R., Hintzen, D., Canty, J.T., Yildiz, A., and Dumont, S. (2020). The mitotic protein NuMA plays a spindle-independent role in nuclear formation and mechanics. J. Cell Biol. *219*.

57. Du, Q., Taylor, L., Compton, D.A., and Macara, I.G. (2002). LGN blocks the ability of NuMA to bind and stabilize microtubules: A mechanism for mitotic spindle assembly regulation. Curr. Biol. *12*, 1928–1933.

58. Gallini, S., Carminati, M., De Mattia, F., Pirovano, L., Martini, E., Oldani, A., Asteriti, I.A., Guarguaglini, G., and Mapelli, M. (2016). NuMA Phosphorylation by Aurora-A Orchestrates Spindle Orientation. Curr. Biol. *26*, 458–469.

59. Hueschen, C.L., Kenny, S.J., Xu, K., and Dumont, S. (2017). NuMA recruits dynein activity to microtubule minus-ends at mitosis. Elife, 1–26.

60. Kotak, S., Busso, C., and Gönczy, P. (2014). NuMA interacts with phosphoinositides and links the mitotic spindle with the plasma membrane. EMBO J. *33*, 1815–1830.

61. Zheng, Z., Wan, Q., Meixiong, G., and Du, Q. (2014). Cell cycle-regulated membrane binding of NuMA contributes to efficient anaphase chromosome separation. Mol. Biol. Cell *25*, 606–619.

62. Mattagajasingh, S.N., Huang, S.C., and Benz, E.J. (2009). Inhibition of Protein 4.1 R and NuMA interaction by mutagenization of their binding-sites abrogates nuclear localization of 4.1 R. Clin. Transl. Sci. *2*, 102–111.

63. Rajeevan, A., Keshri, R., Kapoor, S., and Kotak, S. (2020). NuMA interaction with chromatin is vital for proper chromosome decondensation at the mitotic exit. Mol. Biol. Cell *31*, 2437–2451.

64. Kotak, S., Busso, C., and Gönczy, P. (2013). NuMA phosphorylation by CDK1 couples mitotic progression with cortical dynein function. EMBO J. *32*, 2517–2529.

65. Keshri, R., Rajeevan, A., and Kotak, S. (2020). PP2A-B55γ counteracts Cdk1 and regulates proper spindle orientation through the cortical dynein adaptor NuMA. J. Cell Sci. *133*.

66. Kiyomitsu, T., and Cheeseman, I.M. (2013). Cortical dynein and asymmetric membrane elongation coordinately position the spindle in anaphase. Cell *154*, 391.

67. Matsumura, S., Hamasaki, M., Yamamoto, T., Ebisuya, M., Sato, M., Nishida, E., and

Toyoshima, F. (2012). ABL1 regulates spindle orientation in adherent cells and mammalian skin. Nat. Commun. *3*.

68. Lee, B.H., Schwager, F., Meraldi, P., and Gotta, M. (2018). p37/UBXN2B regulates spindle orientation by limiting cortical NuMA recruitment via PP1/Repo-Man. J. Cell Biol. *217*, 483–593.

69. Kiyomitsu, T., and Cheeseman, I.M. (2012). Chromosome-and spindle-pole-derived signals generate an intrinsic code for spindle position and orientation. Nat. Cell Biol. *14*, 311–317.

70. Sana, S., Keshri, R., Rajeevan, A., Kapoor, S., and Kotak, S. (2018). Plk1 regulates spindle orientation by phosphorylating NuMA in human cells. Life Sci. Alliance *1*, 1–14.

71. Seo, J.S., Kim, H.N., Kim, S.J., Bang, J., Kim, E.A., Sung, K.S., Yoon, H.J., Yoo, H.Y., and Choi, C.Y. (2014). Cell cycle-dependent SUMO-1 conjugation to nuclear mitotic apparatus protein (NuMA). Biochem. Biophys. Res. Commun. *443*, 259–265.

72. Magescas, J., Sengmanivong, L., Viau, A., Mayeux, A., Dang, T., Burtin, M., Nilsson, U.J., Leffler, H., Poirier, F., Terzi, F., et al. (2017). Spindle pole cohesion requires glycosylation-mediated localization of NuMA. Sci. Rep. *7*, 1–14.

73. Reck-Peterson, S.L., Redwine, W.B., Vale, R.D., and Carter, A.P. (2018). The cytoplasmic dynein transport machinery and its many cargoes. Nat. Rev. Mol. Cell Biol. *19*, 382–398.

74. Lipka, J., Kuijpers, M., Jaworski, J., and Hoogenraad, C.C. (2013). Mutations in cytoplasmic dynein and its regulators cause malformations of cortical development and neurodegenerative diseases. Biochem. Soc. Trans. *41*, 1605–1612.

75. Canty, J.T., and Yildiz, A. (2020). Activation and Regulation of Cytoplasmic Dynein. Trends Biochem. Sci. *45*, 440–453.

76. Canty, J.T., Tan, R., Kusakci, E., Fernandes, J., and Yildiz, A. (2021). Structure and Mechanics of Dynein Motors. Annu. Rev. Biophys. *50*, 549–574.

77. Schroeder, C.M., Ostrem, J.M.L., Hertz, N.T., and Vale, R.D. (2014). A Ras-like domain in the light intermediate chain bridges the dynein motor to a cargo-binding region. Elife *3*, 1–22.

78. Urnavicius, L., Zhang, K., Diamant, A.G., Motz, C., Schlager, M.A., Yu, M., Patel, N.A., Robinson, C. V., and Carter, A.P. (2015). The structure of the dynactin complex and its interaction with dynein. Science (80-.). *347*, 1441–1446.

79. Steinmetz, M.O., and Akhmanova, A. (2008). Capturing protein tails by CAP-Gly domains. Trends Biochem. Sci. *33*, 535–545.

80. McKenney, R.J., Huynh, W., Vale, R.D., and Sirajuddin, M. (2016). Tyrosination of α-tubulin controls the initiation of processive dynein–dynactin motility. EMBO J. *35*, 1175–1185.

81. Zhang, K., Foster, H.E., Rondelet, A., Lacey, S.E., Bahi-Buisson, N., Bird, A.W., and Carter, A.P. (2017). Cryo-EM Reveals How Human Cytoplasmic Dynein Is Auto-inhibited and Activated. Cell *169*, 1303–1314.e18.

82. McKenney, R.J., Huynh, W., Tanenbaum, M.E., Bhabha, G., and Vale, R.D. (2014). Activation of cytoplasmic dynein motility by dynactin-cargo adapter complexes. Science (80-.). *345*, 337–341.

83. Schlager, M.A., Hoang, H.T., Urnavicius, L., Bullock, S.L., and Carter, A.P. (2014). In vitro reconstitution of a highly processive recombinant human dynein complex.

EMBO J. *33*, 1855–1868.

84. Urnavicius, L., Lau, C.K., Elshenawy, M.M., Morales-Rios, E., Motz, C., Yildiz, A., and Carter, A.P. (2018). Cryo-EM shows how dynactin recruits two dyneins for faster movement. Nature *554*, 202–206.

85. Elshenawy, M.M., Kusakci, E., Volz, S., Baumbach, J., Bullock, S.L., and Yildiz, A. (2020). Lis1 activates dynein motility by modulating its pairing with dynactin. Nat. Cell Biol. *22*, 570–578.

86. Kendrick, A.A., Dickey, A.M., Redwine, W.B., Tran, P.T., Vaites, L.P., Dzieciatkowska, M., Harper, J.W., and Reck-Peterson, S.L. (2019). Hook3 is a scaffold for the opposite-polarity microtubule-based motors cytoplasmic dynein-1 and KIF1C. J. Cell Biol. *218*, 2982–3001.

87. Schroeder, C.M., and Vale, R.D. (2016). Assembly and activation of dynein-dynactin by the cargo adaptor protein Hook3. J. Cell Biol. *214*, 309–318.

88. Gama, J.B., Pereira, C., Simões, P.A., Celestino, R., Reis, R.M., Barbosa, D.J., Pires, H.R., Carvalho, C., Amorim, J., Carvalho, A.X., et al. (2017). Molecular mechanism of dynein recruitment to kinetochores by the Rod-Zw10-Zwilch complex and Spindly. J. Cell Biol. *216*, 943–960.

89. Lee, I.G., Olenick, M.A., Boczkowska, M., Franzini-Armstrong, C., Holzbaur, E.L.F., and Dominguez, R. (2018). A conserved interaction of the dynein light intermediate chain with dynein-dynactin effectors necessary for processivity. Nat. Commun. *9*.

90. Olenick, M.A., Tokito, M., Boczkowska, M., Dominguez, R., and Holzbaur, E.L.F. (2016). Hook adaptors induce unidirectional processive motility by enhancing the Dynein-Dynactin interaction. J. Biol. Chem. *291*, 18239–18251.

91. Yin, L.M., Schnoor, M., and Jun, C.D. (2020). Structural Characteristics, Binding Partners and Related Diseases of the Calponin Homology (CH) Domain. Front. Cell Dev. Biol. *8*, 1–7.

92. Lee, I.G., Cason, S.E., Alqassim, S.S., Holzbaur, E.L.F., and Dominguez, R. (2020). A tunable LIC1-adaptor interaction modulates dynein activity in a cargo-specific manner. Nat. Commun. *11*, 1–13.

93. Ohata, H., Miyazaki, M., Otomo, R., Matsushima-Hibiya, Y., Otsubo, C., Nagase, T., Arakawa, H., Yokota, J., Nakagama, H., Taya, Y., et al. (2013). NuMA Is Required for the Selective Induction of p53 Target Genes. Mol. Cell. Biol. *33*, 2447–2457.

94. Harborth, J., Wang, J., Gueth-Hallonet, C., Weber, K., and Osborn, M. (1999). Self assembly of NuMA: Multiarm oligomers as structural units of a nuclear lattice. EMBO J. *18*, 1689–1700.

95. Radulescu, A.E., and Cleveland, D.W. (2010). NuMA after 30 years: The matrix revisited. Trends Cell Biol. *20*, 214–222.

96. Ludérus, M.E., den Blaauwen, J.L., de Smit, O.J., Compton, D.A., and van Driel, R. (1994). Binding of matrix attachment regions to lamin polymers involves single-stranded regions and the minor groove. Mol. Cell. Biol. *14*, 6297–6305.

97. Patricia C. Abad, Jason Lewis, I. Saira Mian, David W. Knowles, Jennifer Sturgis, Sunil Badve, Jun Xie, and S.A.L. (2007). NuMA Influences Higher Order Chromatin Organization in Human Mammary Epithelium. Mol. Biol. Cell *18*, 348–361.

98. Harborth, J., Weber, K., and Osborn, M. (2000). GAS41, a highly conserved protein in eukaryotic nuclei, binds to NuMA. J. Biol. Chem. *275*, 31979–31985.

99. Jayaraman, S., Chittiboyina, S., Bai, Y., Abad, P.C., Vidi, P.A., Stauffacher, C. V., and Lelièvre, S.A. (2017). The nuclear mitotic apparatus protein NuMA controls rDNA transcription and mediates the nucleolar stress response in a p53-independent manner. Nucleic Acids Res. *45*, 11725–11742.

100. Lieber, M.R. (2010). The mechanism of double-strand DNA break repair by the nonhomologous DNA end-joining pathway. Annu. Rev. Biochem. *79*, 181–211.

101. Heyer, W.D., Ehmsen, K.T., and Liu, J. (2010). Regulation of homologous recombination in eukaryotes. Annu. Rev. Genet. *44*, 113–139.

102. Ciccia, A., and Elledge, S.J. (2010). The DNA Damage Response: Making It Safe to Play with Knives. Mol. Cell *40*, 179–204.

103. Matsuoka, S., Ballif, B.A., Smogorzewska, A., McDonald, E.R., Hurov, K.E., Luo, J., Bakalarski, C.E., Zhao, Z., Solimini, N., Lerenthal, Y., et al. (2007). ATM and ATR substrate analysis reveals extensive protein networks responsive to DNA damage. Science (80-.). *316*, 1160–1166.

104. Vidi, P.A., Liu, J., Salles, D., Jayaraman, S., Dorfman, G., Gray, M., Abad, P., Moghe, P. V., Irudayaraj, J.M., Wiesmüller, L., et al. (2014). NuMA promotes homologous recombination repair by regulating the accumulation of the ISWI ATPase SNF2h at DNA breaks. Nucleic Acids Res. *42*, 6365–6379.

105. Chang, W., Dynek, J.N., and Smith, S. (2005). NuMA is a major acceptor of poly(ADP-ribosyl)ation by tankyrase 1 in mitosis. Biochem. J. *391*, 177–184.

106. Boehler, C., Gauthier, L.R., Mortusewicz, O., Biard, D.S., Saliou, J.M., Bresson, A., Sanglier-Cianferani, S., Smith, S., Schreiber, V., Boussin, F., et al. (2011). Poly(ADP-ribose) polymerase 3 (PARP3), a newcomer in cellular response to DNA damage and mitotic progression. PNAS *108*, 2783–2788.

107. Vidi, P.A., Chandramouly, G., Gray, M., Wang, L., Liu, E., Kim, J.J., Roukos, V., Bissell, M.J., Moghe, P. V., and Lelièvre, S.A. (2012). Interconnected contribution of tissue morphogenesis and the nuclear protein NuMA to the DNA damage response. J. Cell Sci. *125*, 350–361.

108. Dimitrova, N., Chen, Y.C.M., Spector, D.L., and De Lange, T. (2008). 53BP1 promotes non-homologous end joining of telomeres by increasing chromatin mobility. Nature *456*, 524–528.

109. Panier, S., and Boulton, S.J. (2014). Double-strand break repair: 53BP1 comes into focus. Nat. Rev. Mol. Cell Biol. *15*, 7–18.

110. Mirman, Z., and de Lange, T. (2020). 53BP1: a DSB escort. Genes Dev. *34*, 7–23.

111. Callen, E., Di Virgilio, M., Kruhlak, M.J., Nieto-Soler, M., Wong, N., Chen, H.T., Faryabi, R.B., Polato, F., Santos, M., Starnes, L.M., et al. (2013). 53BP1 mediates productive and mutagenic DNA repair through distinct phosphoprotein interactions. Cell *153*, 1266–1280.

112. Becker, J.R., Cuella-Martin, R., Barazas, M., Liu, R., Oliveira, C., Oliver, A.W., Bilham, K., Holt, A.B., Blackford, A.N., Heierhorst, J., et al. (2018). The ASCIZ-DYNLL1 axis promotes 53BP1-dependent non-homologous end joining and PARP inhibitor sensitivity. Nat. Commun. *9*, 1–12.

113. Zhang, F., and Gong, Z. (2021). Regulation of DNA double-strand break repair pathway choice: a new focus on 53BP1. J. Zhejiang Univ. Sci. B *22*, 38–46.

114. Kilic, S., Lezaja, A., Gatti, M., Bianco, E., Michelena, J., Imhof, R., and Altmeyer, M. (2019). Phase separation of 53BP1 determines liquid-like behavior of DNA repair compartments. EMBO J. *38*, 1–17.

115. Botuyan, M.V., Lee, J., Ward, I.M., Kim, J.E., Thompson, J.R., Chen, J., and Mer, G. (2006). Structural Basis for the Methylation State-Specific Recognition of Histone H4-K20 by 53BP1 and Crb2 in DNA Repair. Cell *127*, 1361–1373.

116. Fradet-Turcotte, A., Canny, M.D., Escribano-Díaz, C., Orthwein, A., Leung, C.C.Y., Huang, H., Landry, M.C., Kitevski-Leblanc, J., Noordermeer, S.M., Sicheri, F., et al. (2013). 53BP1 is a reader of the DNA-damage-induced H2A Lys 15 ubiquitin mark. Nature *499*, 50–54.

117. Wilson, M.D., Benlekbir, S., Fradet-Turcotte, A., Sherker, A., Julien, J.P., McEwan, A., Noordermeer, S.M., Sicheri, F., Rubinstein, J.L., and Durocher, D. (2016). The structural basis of modified nucleosome recognition by 53BP1. Nature *536*, 100–103.

118. Luessing, J., Sakhteh, M., Sarai, N., Frizzell, L., Tsanov, N., Ramberg, K.O., Maretto, S., Crowley, P.B., and Lowndes, N.F. (2021). The nuclear kinesin KIF18B promotes 53BP1-mediated DNA double-strand break repair. Cell Rep. *35*, 109306.

119. Drané, P., Brault, M.E., Cui, G., Meghani, K., Chaubey, S., Detappe, A., Parnandi, N., He, Y., Zheng, X.F., Botuyan, M.V., et al. (2017). TIRR regulates 53BP1 by masking its histone methyl-lysine binding function. Nature *543*, 211–216.

120. Orthwein, A., Fradet-Turcotte, A., Noordermeer, S.M., Canny, M.D., Brun, C.M., Strecker, J., Escribano-Diaz, C., and Durocher, D. (2014). Mitosis inhibits DNA double-strand break repair to guard against telomere fusions. Science (80-.). *344*, 189–193.

121. Lambrus, B.G., and Holland, A.J. (2017). A New Mode of Mitotic Surveillance. Trends Cell Biol. *27*, 314–321.

122. Lambrus, B.G., Daggubati, V., Uetake, Y., Scott, P.M., Clutario, K.M., Sluder, G., and Holland, A.J. (2016). A USP28-53BP1-p53-p21 signaling axis arrests growth after centrosome loss or prolonged mitosis. J. Cell Biol. *214*, 143–153.

123. Banani, S.F., Lee, H.O., Hyman, A.A., and Rosen, M.K. (2017). Biomolecular condensates: Organizers of cellular biochemistry. Nat. Rev. Mol. Cell Biol. *18*, 285–298.

124. Alberti, S., and Dormann, D. (2019). Liquid-Liquid Phase Separation in Disease. Annu. Rev. Genet. *53*, 171–194.

125. Boija, A., Klein, I.A., and Young, R.A. (2021). Biomolecular Condensates and Cancer. Cancer Cell *39*, 174–192.

126. Shin, Y., and Brangwynne, C.P. (2017). Liquid phase condensation in cell physiology and disease. Science (80-.). *357*.

127. Krainer, G., Welsh, T.J., Joseph, J.A., Espinosa, J.R., Wittmann, S., de Csilléry, E., Sridhar, A., Toprakcioglu, Z., Gudiškytė, G., Czekalska, M.A., et al. (2021). Reentrant liquid condensate phase of proteins is stabilized by hydrophobic and non-ionic interactions. Nat. Commun. *12*, 1–14.

128. Boeynaems, S., Alberti, S., Fawzi, N.L., Mittag, T., Polymenidou, M., Rousseau, F., Schymkowitz, J., Shorter, J., Wolozin, B., Van Den Bosch, L., et al. (2018). Protein Phase Separation: A New Phase in Cell Biology. Trends Cell Biol. *28*, 420–435.

129. King, M.R., and Petry, S. (2020). Phase separation of TPX2 enhances and spatially coordinates microtubule nucleation. Nat. Commun. *11*, 1–13.

130. Pessina, F., Giavazzi, F., Yin, Y., Gioia, U., Vitelli, V., Galbiati, A., Barozzi, S., Garre, M., Oldani, A., Flaus, A., et al. (2019). Functional transcription promoters at DNA double-strand breaks mediate RNA-driven phase separation of damage-response factors. Nat. Cell Biol. *21*, 1286–1299.

131. Ghodke, I., Remisova, M., Furst, A., Kilic, S., Reina-San-Martin, B., Poetsch, A.R., Altmeyer, M., and Soutoglou, E. (2021). AHNAK controls 53BP1-mediated p53 response by restraining 53BP1 oligomerization and phase separation. Mol. Cell *81*, 2596–2610.e7.

132. Byrum, A.K., Carvajal-Maldonado, D., Mudge, M.C., Valle-Garcia, D., Majid, M.C., Patel, R., Sowa, M.E., Gygi, S.P., Wade Harper, J., Shi, Y., et al. (2019). Mitotic regulators TPX2 and Aurora A protect DNA forks during replication stress by counteracting 53BP1 function. J. Cell Biol. *218*, 422–432.

133. Polverino, F., Naso, F.D., Asteriti, I.A., Palmerini, V., Singh, D., Valente, D., Bird, A.W., Rosa, A., Mapelli, M., and Guarguaglini, G. (2021). The Aurora-A/TPX2 Axis Directs Spindle Orientation in Adherent Human Cells by Regulating NuMA and Microtubule Stability. Curr. Biol. *31*, 658–667.e5.

134. Mahale, S., Kumar, M., Sharma, A., Babu, A., Ranjan, S., Sachidanandan, C., and Mylavarapu, S.V.S. (2016). The light intermediate chain 2 subpopulation of dynein regulates mitotic spindle orientation. Sci. Rep. *6*, 1–16.

135. Kumari, A., Kumar, C., Wasnik, N., and Mylavarapu, S.V.S. (2021). Dynein light intermediate chains as pivotal determinants of dynein multifunctionality. J. Cell Sci. *134*.

136. Alberti, S., Gladfelter, A., and Mittag, T. (2019). Considerations and Challenges in Studying Liquid-Liquid Phase Separation and Biomolecular Condensates. Cell *176*, 419–434.

137. Kamagata, K., Kanbayashi, S., Honda, M., Itoh, Y., Takahashi, H., Kameda, T., Nagatsugi, F., and Takahashi, S. (2020). Liquid-like droplet formation by tumor suppressor p53 induced by multivalent electrostatic interactions between two disordered domains. Sci. Rep. *10*, 1–12.

138. Wang, J., Yuan, Z., Cui, Y., Xie, R., Yang, G., Kassab, M.A., Wang, M., Ma, Y., Wu, C., Yu, X., et al. (2018). Molecular basis for the inhibition of the methyl-lysine binding function of 53BP1 by TIRR. Nat. Commun. *9*.

139. Wang, Z., Zhang, G., and Zhang, H. (2019). Protocol for analyzing protein liquid–liquid phase separation. Biophys. Reports *5*, 1–9.

140. Kabsch, W. (2010). Integration, scaling, space-group assignment and post-refinement. Acta Crystallogr. Sect. D Biol. Crystallogr. *66*, 133–144.

141. Winter, G., Lobley, C.M.C., and Prince, S.M. (2013). Decision making in xia2. Acta Crystallogr. Sect. D Biol. Crystallogr. *69*, 1260–1273.

142. Terwilliger, T.C., Adams, P.D., Read, R.J., McCoy, A.J., Moriarty, N.W., Grosse-Kunstleve, R.W., Afonine, P. V., Zwart, P.H., and Hung, L.W. (2009). Decision-making in structure solution using Bayesian estimates of map quality: The PHENIX AutoSol wizard. Acta Crystallogr. Sect. D Biol. Crystallogr. *65*, 582–601.

143. Adams, P.D., Afonine, P. V., Bunkóczi, G., Chen, V.B., Davis, I.W., Echols, N., Headd, J.J., Hung, L.W., Kapral, G.J., Grosse-Kunstleve, R.W., et al. (2010). PHENIX: A comprehensive Python-based system for macromolecular structure solution. Acta Crystallogr. Sect. D Biol. Crystallogr. *66*, 213–221.

144. Terwilliger, T.C., Grosse-Kunstleve, R.W., Afonine, P. V., Moriarty, N.W., Zwart, P.H., Hung, L.W., Read, R.J., and Adams, P.D. (2007). Iterative model building, structure refinement and density modification with the PHENIX AutoBuild wizard. Acta Crystallogr. Sect. D Biol. Crystallogr. *64*, 61–69.

145. Emsley, P., Lohkamp, B., Scott, W.G., and Cowtan, K. (2010). Features and

development of Coot. Acta Crystallogr. Sect. D Biol. Crystallogr. *66*, 486–501.

146. Sacristan, C., Ahmad, M.U.D., Keller, J., Fermie, J., Groenewold, V., Tromer, E., Fish, A., Melero, R., Carazo, J.M., Klumperman, J., et al. (2018). Dynamic kinetochore size regulation promotes microtubule capture and chromosome biorientation in mitosis. Nat. Cell Biol. *20*, 800–810.

147. Schindelin, J., Arganda-Carreras, I., Frise, E., Kaynig, V., Longair, M., Pietzsch, T., Preibisch, S., Rueden, C., Saalfeld, S., Schmid, B., et al. (2012). Fiji: An open-source platform for biological-image analysis. Nat. Methods *9*, 676–682.

ACKNOWLEDGMENTS

I would like to thank my supervisor Dr. Marina Mapelli, for her valuable advice and teachings during my PhD studies and research and for giving me the opportunity to work on these exciting projects.

I am very grateful to the previous and current members of my group Manuel Carminati, Cristina Cecchetti, Federico Donà, Susanna Eli, Danilo Faccenda, Chiara Gaddoni, Sara Gallini, Edoardo Gelardi, Sara Mari, Andrea Moretti, Valentina Palmerini, Ludovico Pellegrino, Laura Pirovano, Federica Polverino, and Francesca Rizzelli, for their friendship and support during the everyday life in the lab.

I thank the previous and current members of the Biochemistry and Structural Biology Unit at IEO, Sebastiano Pasqualato, Margherita Bruni, Valentina Cecatiello, Giuseppe Ciossani, and Silvia Monzani, for their availability and collaboration.

Thanks to Prof. Stefano Santaguida and to all of his lab members for the scientific discussions during the joint meetings.

Thanks to Dr. Andrew Carter and Clinton Lau (MRC Laboratory of Molecular Biology, UK) for precious help in trying to reconstitute motility of the NuMA-dynein-dynactin complex.

I thank Dr. Ylli Doksani (IFOM) for his valuable advice and collaboration on the NuMA-53BP1 project.

Thanks to Dr. Paolo Maiuri and Alessandro Poli (IFOM) for their recent collaboration on an interesting project regarding the regulation of nuclear mechanics by NuMA.

I thank Michele Giannattasio at the IFOM Electron Microscopy Facility, for precious help in trying to image purified NuMA by electron microscopy.

I thank Simona Rodighiero at the IEO Imaging Unit, for teaching me to use the optical microscopes.

I thank Dr. Tomomi Kiyomitsu (Nagoya University, Japan), for providing the HCT116-GFP-NuMA cell line.

I would like to thank my internal advisor Dr. Tiziana Bonaldi and my external advisor Prof. Monica Gotta, for their valuable advice and availability. A special mention goes to Dr. Ylli Doksani (IFOM) and Prof. Sachin Kotak (IISc, Bangalore), for agreeing to serve as my PhD examiners.

Finally, thanks to my love, family and friends for always loving and supporting me.